A Study of Fiber Volume Fraction Effects in Notched Unidirectional SCS-6/Ti-15V-3Cr-3Al-3Sn Composite

Steven J. Covey
University of Cinicinnati
Cincinnati, Ohio

September 1993

NASA

National Aeronautics and
Space Administration

A STUDY OF FIBER VOLUME FRACTION EFFECTS

IN NOTCHED UNIDIRECTIONAL

SCS-6/Ti-15V-3Cr-3Al-3Sn COMPOSITE

A Dissertation submitted to the

Division of Research and Advanced Studies
of the University of Cincinnati

in partial fulfillment of the
requirements for the degree of

DOCTOR OF PHILOSOPHY

in the Department of Materials Science and Engineering
of the College of Engineering

May 1993

by

Steven J. Covey

B.S., University of Wisconsin, 1982

M.S., University of Wisconsin, 1984

Committee Chair: Dr. N. Jayaraman

ABSTRACT

Notched unidirectional SCS-6/Ti-15-3 composite of three different fiber volume fractions (vf=0.15, 0.37, and 0.41) were investigated for various room temperature microstructural and material properties including; fatigue crack initiation, fatigue crack growth, and fracture toughness. While the matrix hardness is similar for all fiber volume fractions, the fiber/matrix interfacial shear strength and matrix residual stress increases with fiber volume fraction. The composite fatigue crack initiation stress is shown to be matrix controlled and occurs when the net maximum matrix stress approaches the endurance limit stress of the matrix. A model is presented which includes residual stresses and presents the composite initiation stress as a function fiber volume fraction. This model predicts a maximum composite initiation stress at vf≈0.15 which agrees with the experimental data. The applied composite stress levels were increased as necessary for continued crack growth. The applied ΔK values at crack arrest increase with fiber volume fraction by an amount better approximated using an energy based formulation rather than when scaled linear with modulus. After crack arrest, the crack growth

rate exponents for vf37 and vf41 were much lower and toughness much higher, when compared to the unreinforced matrix, because of the bridged region which parades with the propagating fatigue crack. However, the vf15 material exhibited a higher crack growth rate exponent and lower toughness than the unreinforced matrix because once the bridged fibers nearest the crack mouth broke, the stress redistribution broke all bridged fibers, leaving an unbridged crack. Degraded, unbridged behavior is modeled using the residual stress state in the matrix ahead of the crack tip. Plastic zone sizes have been directly measured using a metallographic technique and allow prediction of an effective matrix stress intensity which agrees with the fiber pressure model if residual stresses are considered. The sophisticated macro/micro finite element models of the 0.15 and 0.37 fiber volume fractions presented here show good agreement with experimental data and the fiber pressure model when an estimated effective fiber/matrix debond length is used.

ACKNOWLEDGEMENTS

TABLE OF CONTENTS

LIST OF TABLES

LIST OF FIGURES

LIST OF SYMBOLS

a   = total crack length

a_o = unbridged crack length

A   = linearity constant between residual stresses and fiber volume

B   = coefficient of the Paris law

$c(x)$ = crack face closure tractions

COD   = crack opening displacement

da/dN   = crack growth rate

E_i = Young's modulus, i = c, f, m for composite, fiber, and matrix

g   = crack growth rate exponent of the Paris law

G^i = energy release rate, i = c, f, m for composite, fiber, and matrix

$H(a/w, x)$ = weight function

K^i = stress intensity, i = c, f, m for composite, fiber, and matrix

K_t = stress concentration factor

L   = specimen gage length

L_{eff} = effective fiber/matrix debond length

m_1, m_2 = geometric constants for stress intensity calculation

m/c	= meters per cycle
N	= number of cycles
p(x)	= net crack face tractions
R	= fiber radius
r_p	= plastic zone size
R-ratio	= ratio of minimum to maximum applied stress
s	= dummy integration variable
u(a/w,x)	= half crack opening displacement
v_i	= volume fraction, i = f, m for fiber, matrix
vfj	= composite fiber volume percentage, j=15, 37, 41
W	= specimen width
x	= position from free surface (Chapter 2) or crack tip (Appendix 2)
x'	= dummy integration variable
α_i	= coefficient of thermal expansion, i = f, m for fiber, matrix
ß	= dimensionless crack length, a/w
θ	= angle measured counter-clockwise from the crack tip
Δa	= change in crack length
ΔCOD	= change in crack opening displacement
ΔK	= stress intensity range
ΔN	= change in number of cycles

ΔT = change in temperature

σ^{∞} = remote applied stress

σ_i^j = stress,i=c,m composite, matrix, j=A,N,R applied, net, residual

τ = fiber/matrix interfacial friction stress

ν_c = composite poisson's raio, ν_{12}

-Chapter 1-

MATERIAL AND EXPERIMENTAL DETAILS

1.1 INTRODUCTION

For many years titanium alloys have been used in aircraft design because of their high strength and low density. When consolidated with high strength/high modulus fibers, the resulting composite possesses properties approaching those considered as necessary for next generation aerospace vehicles. Consequently, there have been numerous studies aimed at understanding this class of composite material's microstructure and mechanical behavior in various environments. However, most of these studies were performed on approximately the same fiber volume fraction ($\approx$0.35). A systematic study of how fiber volume fraction influences composite microstructure and fatigue crack initiation and growth for this class of materials has not appeared in the literature. To this end, microstructural characterization and fatigue crack initiation and growth tests were performed on composite with

three different fiber volume fractions: 0.15, 0.37, and 0.41.

1.2 MATERIAL

The composite material used for this study was the Ti-15V-3Cr-3Al-3Sn (wt%, Ti-15-3) matrix with the SCS-6 fiber. Ti-15-3 is a cold workable beta (bcc) alloy which ages via alpha (hcp) precipitation[1]. The alloy can be considered as elastic-perfectly plastic for modeling and has been shown to undergo room temperature deformation without strain-induced transformations, twinning, or precipitation[2]. The SCS-6 fiber is a 144 micron diameter silicon carbide fiber with multiple outer carbon layers[3] for protection from damage during processing. Typical fiber and matrix constitutive properties at room temperature are listed in Table 1.1. In particular, note that the coefficient of thermal expansion, α, of the matrix is over twice that of the fiber.

The materials were manufactured by Textron Specialty Metals Division via foil-fiber-foil techniques and use a molybdenum wire weave to help maintain fiber positioning during fabrication. Unidirectional materials were obtained with measured fiber volume fractions of 0.15, 0.37, and 0.41, hereafter referred to as vf15, vf37, and vf41, respectively. The manufacturing date for the vf15 and vf41 plates was June 1991 and the vf37 plate was manufactured about one-and-one-half years earlier. The

composites were well consolidated with no observed voids or microcracks. Photomicrographs of the polished and etched longitudinal cross-sections of the vf15 and vf41 materials are shown in Figure 1.1. Photomicrographs of vf37 are similar to vf41 and have been presented elsewhere[4].

1.3 SPECIMEN GEOMETRY

The vf15 and vf41 specimens were waterjet cut from the plates in the geometry shown in Figure 1.2 with the loading axis parallel to the fibers. The vf37 specimen was essentially rectangular with no reduced gage section. Single edge notch geometry was obtained by notching one side of each sample with a rounded 150 micron diamond wheel. The nominal notch depth-to-width ratio was 0.2. After notching, no attempt was made to relieve or polish the notch surface, although the specimen faces were mechanically polished to facilitate slip and crack observations. The samples were tested in the as-received condition with no heat treatment.

1.4 TEST CONDITIONS

Three single edge notch specimens (vf15#1, vf37, vf41#1) were tested on a servo-hydraulic fatigue stage mounted inside a scanning electron microscope[5] (SEM) at

room temperature in vacuum. This fatigue stage consists of a dual integral piston design for automatic point-of-interest stability and is shown in Figure 1.3. The R-ratio (ratio of minimum load to maximum load) was 0.1. Tests were conducted in load control with typical sinusoidal frequencies ranging from five to twenty Hertz.

The SEM interfaces with an image analysis system which allows real time, high magnification measurements. The laboratory layout is shown in Figure 1.4. Initiation and crack length measurements normally required magnifications of less than 3000X while near tip crack opening displacements (CODs) were measured at magnifications exceeding 20,000X. The top grip rotated freely, allowing a view of both sides of the sample and in the notch simply by returning to zero load and rotating the loading piston which contains the bottom grip. Three additional tests (vf15#2, vf41#2, and vf41#3) were performed at NASA using a similar SEM mounted test system but a different grip design. While the grips used for the first three tests (vf15#1, vf37, and vf41#1) were not rotationally constrained, the grips used for the last three tests (vf15#2, vf41#2, and vf41#3) were rotationally constrained.

1.5 APPLIED STRESS LEVELS

The composite fatigue crack initiation stress, as discussed in Chapter 2, is the

minimum cyclic stress necessary to initiate fatigue cracks in these materials. In order to determine the composite fatigue crack initiation stress, the initial applied stress level was below that necessary to initiate cracks. The applied stress level was then increased in roughly 10% increments after tens-of-thousands of cycles until cracks initiated. Once initiated, these microcracks sometimes required additional stress increases for the cracks to coalesce, and then formed a through-the-thickness crack, growing until the crack was arrested. At crack arrest, the stress levels were again incremented until the crack advanced. These minimum stress levels were selected to help confine the damage evolution to the matrix, thereby leaving undamaged fibers in the crack wake. Gradual incrementing of the applied stresses would also help discern exactly what applied stress level breaks the bridged fibers nearest the crack mouth after crack arrest. The applied stresses used here should be considered the minimum path for continued damage evolution. These stresses should result in improved fatigue crack growth and fracture toughness properties, when compared to results from higher stress levels, because of the additional bridged fibers in the crack wake.

MATERIAL PROPERTIES AND MATRIX CRACK INITIATION

Application of these thin composite sheets to aerospace structures requires many notches and holes. Notches and holes act as stress concentrations and promote initiation of fatigue cracks. Consequently, how fatigue cracks initiate at notches and holes must be well understood for various notch annd hole geometries and as a function of fiber volume fraction. Fiber volume fraction effects on fatigue crack initiation for a single edge notch geometry will be presented next.

2.1 MATERIAL PROPERTIES RESULTS

2.1.1 Microstructure and Properties

From the photomicrographs in Figure 1.1, it is apparent that the vf15 material has fewer touching fibers and larger grain size, were the grain boundaries have been

delineated by etching. The etch also delineated the titanium foil edges and Figure 1.1 shows that vf15 was processed using eighteen titanium foils and vf41 used nine. The approximate grain sizes and plate thicknesses are shown in Table 2.1. The average hardness of the interior matrix grains for vf15 and vf41 were determined with at least ten measurements using a 200g Vickers micro indenter and compares well with earlier work for vf37 [Ref 4]. The similar matrix hardness values (~250) imply similar matrix compositions and consequently little difference in extent of fiber reaction products diffusing into the matrix. Consequently, the in-situ matrix properties are expected to be similar. The composite modulus and strength values given in Table 2.1 are about ten percent below rule-of-mixtures when using the in-situ fiber strength of 2.7 GPa[6,7].

2.1.2 Fiber Pushout Tests

Fiber pushout tests were performed on a recently developed desktop device[8] which employs a 200 N load cell and loads at a rate of 0.815 microns per second. Each specimen was about 384 microns thick and the surfaces were polished for ease of testing. A typical load vs time curve is shown in Figure 2.1. A clear debond point was not always observed in the load-time data but frequently appeared in the acoustic emission signal, which is shown on the bottom of the

graph.

The average of at least thirty-five fiber pushout tests shows increasing fiber/matrix interfacial shear strengths with increasing fiber volume fraction and interfacial shear strengths of 113, 128, and 151 MPa for vf15, vf37, and vf41, respectively. Table 2.1 shows these values with standard deviations which do overlap and may reduce the significance of the variations. The 128 MPa shear strength for vf37 agrees well with the shear strength reported elsewhere for this same material with a 0.39 fiber volume fraction [Ref 6]. This increase in interfacial shear strength with fiber volume fraction implies a stronger fiber/matrix processing induced bond and can be partially explained by the higher residual matrix clamping stresses found in the higher fiber volume fraction material (to be discussed shortly). Once this fiber/matrix bond is broken, the fiber/matrix interface can be considered as two separate surfaces with a friction stress between them. The fiber/matrix interfacial friction stress can be measured by performing pushout tests after the fiber/matrix bond has already been broken. An interfacial friction stress of about 80 MPa has been reported in Reference 6 for a 0.39 fiber volume fraction and was measured by a second fiber pushout test where the specimen is turned over and the fiber pushed back into the composite after the initial bond has been broken. Pushout tests performed on fatigue tested coupons nine millimeters from

the fracture surface showed the same 80 MPa friction stress for all fiber volume fractions. It was originally thought that these tested coupons were far enough removed from the fracture surface that the results could be considered untested. Apparently, some sort of debonding activity occurs over the entire gage length.

2.1.3 Residual Stresses

Residual stresses are induced in these materials upon cooldown from the processing temperature because of the difference in coefficient of thermal expansion between the fiber and the matrix. Even though there are many types of models for predicting residual stresses in metal matrix composites, such as concentric cylinder or hexagonal arrays[9], the quarter fiber finite element model was used here because, for other titanium matrix composites, it has been shown to compare favorably with measurements from x-ray[10] and neutron[11] diffraction techniques.

Generally, quarter fiber models, or unit cells, use assumed dimensions which average out the fiber spacing and have a fiber volume fraction equivalent to that of the overall composite. For this work dimensions of unit cells were determined using the periodic nature of the fiber spacing within rows, as discussed in

Appendix 1, and are shown in Figure 2.2. In Appendix 1, measurements made on the composite are presented which show that fiber spacing is periodic within rows for these foil-fiber-foil composites. The fiber periodicity within rows not only provides dimensions for the unit cells, but also suggests a variation in crack initiation with notch location. These repeated rectangular arrays, or unit cells, represent the interior of the composite away from the matrix rich surface regions and have fiber volume fractions of 0.177, 0.431, and 0.476 for vf15, vf37, and vf41, respectively. It is believed that the higher internal fiber volume fraction is the correct one for understanding fatigue crack initiation and growth in these materials because observed initiation and crack growth behavior were controlled by events occurring away from the matrix rich surface regions.

Three dimensional meshes were generated for each of the fiber volume fractions using the PATRAN[12] (pre, post-processing) and MARC[13] (solver) finite element software and executed on the Cray YMP computer. The models employed about three hundred, eight-noded brick elements with planar displacements enforced at the surfaces and the temperature dependent fiber and matrix properties in Table 2.2. The mesh used for vf37 is shown in Figure 2.3. The fiber and matrix were assumed perfectly bonded with uniform temperature changes of 675C during cooldown. The maximum residual stresses generally increase with

fiber volume fraction and are listed in Table 2.3. These values are in fairly good agreement with values presented elsewhere for similar materials but different unit cell dimensions[14]. Note that Table 2.3 lists only the maximum residual stress values, regardless of location. These maximum values were observed in or between fiber rows, depending upon stress component. Although not evaluated in the current work, Reference 14, and Reference 9 for a different composite system, have shown that the matrix residual radial stress actually decreases in magnitude with increase in fiber volume fraction for a location at about 45 degrees from the fiber row.

Note that even though plastic deformation does not occur during cooldown in the FEM model for vf15 and vf37, the longitudinal matrix residual stresses, σ_m^R, reported here and in Reference 14, are at least 50% larger than those predicted using the expression

$$\sigma_m^R = \frac{(\alpha_f - \alpha_m)}{\frac{1}{E_m} + \frac{(1-V_f)}{E_f V_f}} \Delta T \tag{2.1}$$

where ΔT is negative. A longitudinal matrix residual stress value of 354 MPa has been measured for this same material with a 0.34 fiber volume fraction using x-ray diffraction techniques [Ref 6 of Appendix 3]. This measured value of 354 MPa is identical to that estimated using linear interpolation between the vf15 and vf37

11

FEM predicted values of Table 2.3 and those measured using matrix plasticity as discussed in Appendix 3. The longitudinal matrix residual stress values predicted using Equation 2.1 are lower because fiber-neighbor interactions are not included.

2.2 INITIATION RESULTS

2.2.1 Definition of Fatigue Crack Initiation

Fatigue cracks were considered to be initiated when multiple independent matrix cracks, usually less than 50 microns long, were observed emanating from the regions near the damaged fibers at the notch root. The initial applied stresses were below those necessary to initiate matrix cracks and were increased in roughly 10% increments only if matrix cracks were not observed after an average of 100,000 cycles. If matrix cracks were initiating at the notch root during these lower stresses, they should be readily visible under the high magnifications of the SEM. The applied stress level at the notch which initiates multiple independent matrix cracks is defined here as the composite stress level for fatigue crack initiation. This can be considered as a form of composite stress endurance limit. The accuracy of this composite crack initiation stress probably depends only on the size of the stress increment and the number of cycles applied before crack

initiation occurred. This 10% stress increment can be interpolated using the number of cycles prior to initiation. For example, while vf15#1 experienced almost 200k cycles at a maximum applied notch stress of 684 MPa prior to formation of these small matrix cracks, vf41#1 underwent only 5k cycles at 511 MPa. Consequently, the actual vf15#1 initiation stress is probably somewhat higher while that of vf41#1 is probably somewhat lower. Table 2.4 lists the maximum applied notch stress, associated cycles, and damage status for each test sequence.

When matrix cracks did initiate for the vf15 material, the initiation stress level was maintained without further increases until a through-the-thickness crack was formed and the fiber-bridged crack arrested. However, when matrix cracks initiated in the vf37 and vf41 materials, further crack growth to form a through-the-thickness crack required increased stresses, sometimes even before coalescence of the multiple independent matrix cracks. The applied stress was then incremented as necessary to continue fatigue crack growth. Consequently, for the vf15 material this definition of the crack initiation stress is identical to that used previously[15] where initiation is defined as a 500 micron long crack. This definition of initiation (used in Reference 15) is non-conservative, however, for the vf37 and vf41 materials because they required additional stress increments of

almost fifty percent from initiation of many small matrix cracks to grow a 500 micron long, through-the-thickness, crack.

2.2.2 Initiation Experimental Results

The fibers visible at the notch root were all damaged during machining of the notch and were observed to crack first. Cracks initiated into the matrix only after increasing the stress level and many thousands of cycles. Figure 2.4 shows low magnification micrographs of notches in the vf15 and vf41 samples. The initial matrix crack always occurred adjacent to a cracked fiber but not necessarily near the crack in the fiber. Generally, multiple independent initiation sites in the matrix adjacent to the fibers were observed with subsequent coalescence of these microcracks. The sequence of micrographs in Figure 2.5 convey the typical damage evolution process in these materials. For the test shown, the initiation stress level of 684 MPa was chosen because the ten micron long matrix crack observed at 495 MPa was the only one and did not propagate, even after many thousand cycles at 495 MPa, or even for an increased applied notch stress of 561 MPa. The applied initiation stress levels for each sample tested are given in Table 2.5. Also given in Table 2.5 are the notch geometries, stress concentration factors, and resulting notch stresses at initiation. Note that the average notch initiation

stress levels for vf15, vf37, and vf41 are 700, 561, and 490 MPa, respectively, and decrease with increasing fiber volume fraction. Reasons for this unexpected behavior will be presented later.

2.2.3 Surface Slip Band Observations

Surface slip bands were observed on the specimen surface near the notch during fatigue crack initiation, and occasionally during periods of slow crack growth. Figure 2.6 shows that slip bands appeared on the surface much more readily in the vf37 material than vf15. In both photo micrographs, a crack had just appeared on the surface from the notch. The reasons for this more rapid slip appearance in vf37 are unclear, especially since it will been shown later that the net matrix stresses are similar. Perhaps the closer proximity of the fiber to the surface induces higher local shear stresses in the higher fiber volume fraction materials. Figure 2.6 also shows that slip bands in the notch region occasionally showed multiple slip, an indicator of the notch-induced biaxial stress state.

2.2.4 Orientation of Crack Initiation

Matrix cracks frequently initiated at the fiber/matrix interface near 33 degrees

from the horizontal as can be seen in the photomicrographs of Figure 2.5. This angle corresponds to the location of the maximum shear stress as predicted from an orthotropic finite element model of the notch as shown in Figure 2.7. The magnitude of this predicted maximum shear stress is well below the fiber matrix interfacial shear strength. The orthotropic elements used in this model are homogeneous but blend fiber and matrix properties via the rule-of-mixtures type approach and simulate the overall anisotropic laminate behavior. The location of maximum shear stress has been shown to coincide with crack initiation of a circular hole in vf37 of this same material[16] and in a SCS-6/Ti-24Al-11Nb composite [Ref 50]. This information, combined with the other experimental observations presented earlier, indicate that fatigue crack initiation in these materials must be matrix controlled. Finally, in one case a strand of Mo-weave was exposed at the notch root which did not perturb the nearby cracks and was not exposed on the fracture surface after failure. Apparently, Mo-weave plays no role in these initiation tests and at these stress levels.

2.3 INITIATION ANALYSIS AND DISCUSSION

It was shown earlier that the magnitude of all residual stress components generally increase with fiber volume fraction and consequently should influence

mechanical behavior. For example, it will be presented shortly that the almost linearly increasing, longitudinal residual matrix stress influences initiation behavior of the composite. Variations in residual matrix clamping stresses may also be expected to affect mechanical behavior. Reference 14 showed that while increasing fiber volume fraction increases matrix residual clamping stresses at some interface locations, it decreases them at others; acting almost as a stress redistributor. If the residual matrix clamping stress is integrated/averaged around the fiber circumference, it is nearly independent of fiber volume fraction. Consequently, mechanical behavior dependent on the average residual matrix clamping stress, such as the observed fiber/matrix debonding in transverse coupons, may not change with fiber volume fraction. However, the good correlation between the fiber/matrix interfacial shear strength (prior to debonding) and the maximum matrix residual clamping stress with variation in fiber volume fraction seems to imply that the maximum matrix residual clamping stress is a larger factor in interfacial shear strength than the integrated clamping stress. The interfacial shear strength appears to play no role in the notched composite crack initiation stress because while the interfacial shear strength increases with fiber volume fraction, the composite initiation stress decreases. It will be shown next that the net matrix stress is constant when the different composite crack initiation stress levels are applied for each fiber volume fraction.

2.3.1 Matrix Crack Initiation Analysis

As discussed earlier in this paper, and in Reference 15, the mechanism of fatigue crack initiation in these materials seems to be matrix controlled. And the net matrix stress depends on the applied matrix and residual stresses, which are both functions of fiber volume fraction. As fiber volume fraction increases, the longitudinal matrix residual stresses increase and the applied matrix stresses decrease (for a given applied stress). The net matrix stress is simply the sum of these components. It is of interest to model the composite initiation stress level as a function of fiber volume fraction to determine the best fiber volume fraction for minimizing crack initiation. However, the optimum fiber volume fraction for fatigue crack initiation may not be the best when other factors are considered, such as strength, fatigue crack growth, or toughness. Rule-of-mixtures (ROM) will be used to estimate how the applied composite stress affects the net matrix stress.

ROM, which assumes perfect bonding between the fiber and the matrix, and the strain compatibility condition can be combined to estimate the stress imposed on the matrix for a given applied composite stress

$$\sigma_m^A = \frac{\sigma_c^A}{1+v_f(\frac{E_f}{E_m}-1)} \qquad (2.2)$$

where $\quad \sigma_m^A$ = applied matrix stress

$\qquad \sigma_c^A$ = applied composite stress

and the other values have their usual meaning. For a matrix controlled event the net matrix stress, σ_m^N, is of interest and can be obtained by considering only the longitudinal matrix residual stress [Ref 15], σ_m^R, and adding this to the applied matrix stress

$$\sigma_m^N = \sigma_m^A + \sigma_m^R \qquad (2.3)$$

Using these two equations to eliminate σ_m^A and solving for the applied composite stress provides

$$\sigma_c^A = [1+v_f(\frac{E_f}{E_m}-1)] \, [\sigma_m^N - \sigma_m^R] \qquad (2.4)$$

Because of the notch, a stress concentration factor, K_t, must be used to determine the effect of the applied stress on the composite. The longitudinal stress concentration factor was found by use of orthotropic, notched finite element analysis as shown in Figure 2.7, and must be used to determine the applied notch

stresses. Values of K_t are listed in Table 2.5.

2.3.2 Model Application

In this study the applied composite initiation stress level was experimentally determined for each fiber volume fraction as that applied stress level which initiates multiple independent cracks in the matrix material. The stress concentration factors and longitudinal residual stresses were determined from finite element modeling. The only unknown in the previous equation is the net matrix stress, σ_m^N, which can be solved for. Figure 2.8 shows the various stress components of Equation 2.4 as a function of fiber volume fraction. Also shown is the monolithic Ti-15-3 endurance limit stress of 680 MPa obtained from the literature[17] for $R=0.1$ and $K_t=3$. With increasing fiber volume fraction, the applied matrix stress decreases (even with varying composite applied stresses), and the longitudinal matrix residual stress increases. However, the net matrix stress level at these different applied initiation stress levels remains constant at a magnitude equal to the Ti-15-3 stress endurance limit. Consequently, to predict matrix controlled composite initiation behavior the net matrix stress can be set equal to the endurance limit of the matrix. If we apply the stress concentration factor, K_t, to the expression for composite initiation stress level (Equation 2.4), it becomes

$$\sigma_{composite}^{initiation} = \frac{1}{K_t} [1+v_f(\frac{E_f}{E_m}-1)] [\sigma_{titanium}^{endurance} - \sigma_{titanium}^{residual}] \qquad (2.5)$$

Approximating the longitudinal matrix residual stress as linear in fiber volume fraction using an approximation of Equation 2.1 (with $E_f=4E_m$) increased as required by the FEM calculations

$$\sigma_{titanium}^{residual} \approx 3.5E_m(\alpha_f-\alpha_m)\Delta T*V_f = A*V_f \qquad (2.6)$$

The equation for the composite initiation stress becomes

$$K_t\sigma_{composite}^{initiation} = \sigma_{titanium}^{endurance} + (\sigma_{titanium}^{endurance}(\frac{E_f}{E_m}-1)-A)V_f$$
$$- A(\frac{E_f}{E_m}-1)V_f^2 \qquad (2.7)$$

Using the matrix and fiber properties with A=1150 MPa, Equation 2.7 becomes

$$K_t\sigma_{composite}^{initiation} = 680+1192V_f-3961V_f^2 \qquad (2.7a)$$

The initiation stress is plotted vs fiber volume fraction in Figure 2.9. The curve has a peak at a fiber volume fraction of 0.15 which is the optimum fiber volume fraction for preventing fatigue crack initiation. A similar formulation for the fiber net stress shows a monotonically increasing applied composite stress to break the fibers. This expression is also second order in vf but possess a maximum at the largest fiber volume fraction. The fiber formulation agrees with what would normally be expected and lends some credibility to the net matrix stress version.

21

A residual stress linearized value of A=1150 MPa (Figure 2.8 or Table 2.3) for matrix residual stress underestimates (overestimates) the vf15 (vf41) values. The actual extremum may occur at a higher fiber volume fraction or be less pronounced. Applications intolerant of crack initiation should consider the lower fiber volume fraction material although, other factors, such as strength, fatigue crack growth rate, etc, may be more important. Designers may wish to use lower fiber volume material near notches and holes. It will presented in Chapter 3 that substantial increases in the applied stress level were necessary in the higher fiber volume fraction materials to grow these small initiated cracks into through-the-thickness cracks. Consequently, these initiated cracks may have little structural significance. However, these cracks do extend into the matrix and may degrade any environmental protective coatings even before the composite reaches its steady state operating temperature.

2.3.3 Discussion

The matrix controlled crack initiation stress in these composites is that applied mechanical stress level which places the net matrix stress at the matrix stress endurance limit. The proposed model seems to fit the data reasonably well. However, there are some issues not addressed in the model. It is likely that the

observed behavior was affected by notch machining, biaxial stresses due to the notch, or relaxation of residual stresses due to mechanical cycling. Other factors may also be important. The residual stresses act as mean stresses and effectively change the notch R-ratio from 0.1 for the composite to 0.37 for vf15 matrix and 0.7 for the matrix in vf41. It is not clear that Ti-15-3 fatigue life is dominated more by peak stress than R-ratio. In addition, a sophisticated macro/micro finite element model, developed to study fiber bridging during crack growth, has shown that the notch root stress concentration factor decreases by almost twenty percent with high modulus fibers just behind the notch root (See Figure 2.10). At higher stresses K_t decreases substantially as fiber/matrix debonding occurs [Ref 51]. Finally, the analysis completely disregards the fact that initiation appears to be a shear stress driven mechanism. None-the-less, the simple model presented seems to capture the essential initiation mechanics of the SCS-6/Ti-15-3 composite.

At the elevated temperatures for which these materials are intended the residual stresses are greatly reduced. Similar reductions in residual stresses may someday be obtained by the use of engineered interlayers between the fiber and matrix. Without appreciable processing induced residual stresses the expression for composite initiation stress becomes linear in fiber volume fraction and monotonically increases with vf and the previously predicted maximum at vf=0.15

for room temperature does not occur.

-Chapter 3-

FATIGUE CRACK GROWTH AND FRACTURE TOUGHNESS

Titanium alloy matrix composites offer considerable strength and weight improvements over monolithic materials when consolidated with high strength/high modulus fibers. However, the reactivity of the titanium and brittle fiber require use of protective fiber coatings to prevent degradation of the fiber strength during processing[18], and hence subsequent composite strength. The protective coatings are generally weak and known to greatly alter fatigue crack growth and fracture toughness properties of these materials because the weak interfaces promote·fiber/matrix debonding and allows the fatigue crack to pass by the fibers leaving them undamaged[19]. These bridged fibers can drastically improve fatigue crack growth properties and can even cause crack arrest[20,21]. Modeling of fatigue crack growth in the presence of bridged fibers generally attempts to determine a reduced crack tip stress intensity based on a shear lag[22] or fiber pressure[23] model. This reduced crack tip stress intensity allows the

calculation of an effective matrix stress intensity[24] which governs the fatigue crack growth behavior of the composite. In what follows, the fatigue cracks initiated as discussed in Chapter 2 continued to grow until fracture mechanics concepts became applicable. The results and analysis of fatigue crack growth and fracture toughness are presented next.

3.1 EXPERIMENTAL RESULTS

3.1.1 Crack Growth Prior to Arrest

On the surface, a single predominant crack was generally observed, although at times some secondary cracks developed. Subsequent polishing revealed that secondary cracks frequently occurred inside of the composite even when only a single crack was noted on the surface. Only horizontal crack growth data (ie, the projection of the crack onto a plane perpendicular to the loading axis) from the primary crack is reported with crack arrest defined here as average horizontal crack growth rates ($\Delta a/\Delta N$) of less than 0.5×10^{-9} meters per cycle (m/c) for 40,000 cycles. However, even at crack arrest damage may still be accumulating in the form of degraded fiber strength, additional fiber/matrix debonding, etc. The average crack length from both sides of the composite vs number of cycles is

shown (with associated stresses) for each fiber volume fraction in Figure 3.1.
Apparently, only one crack arrest is possible for this specimen geometry with a
through crack in each fiber volume fraction. The stress increments observed in
Figure 3.1 at 325k cycles for vf37 and vf41 were applied before a through crack
had developed and were necessary to obtain horizontal crack growth beyond the
biaxial stress state influence of the notch. Note that for vf15 and vf37 a stress
increase of more than 25% at crack arrest caused no change in the average crack
length for many thousand cycles. This behavior is believed to reflect a stability
point in the crack growth of these materials and will be shown later to depend on
stress history. Fatigue crack arrest is unique to composite materials and is
discussed next.

3.1.2 Crack Arrest

All three fiber volume fractions experienced a crack arrest at crack lengths which
allowed bridging by an average of about sixteen fibers (two or three fibers per
ply). The crack arrest parameters are given in Table 3.1 and the decreasing crack
growth rate da/dN data are given in Table 3.2. These data are averaged from
observations taken on both sides of the composite. The applied stress intensities
are computed using hand book values[25] (see Appendix 2). The da/dN data of

27

Table 3.2 are plotted vs the applied ΔK in Figure 3.2 and compared to the unreinforced matrix data of Reference 27. It is clear that fiber bridging effectively decreases the crack growth rate from that observed in the monolithic alloy. Crack arrest occurs at an applied ΔK of 11.5, 14, and 16.5 MPa $m^{1/2}$ for vf15, vf37, and vf41, respectively.

The effect of stress level on fatigue crack growth behavior is shown in Figure 3.3, which shows da/dN data just prior to arrest for vf37 with three different stress histories. For every decrease in the applied stress level of 80 MPa, a 10 MPa $m^{1/2}$ decrease in the applied stress intensity at crack arrest is observed and hence scales linearly with applied stress level. The bridged crack lengths in these vf37 specimens were similar and spanned roughly twenty fibers (three fibers per ply).

The change in crack opening displacements were also measured near the crack tip and are shown vs position from the crack tip in Figure 3.4 for each fiber volume fraction. Delta COD, defined as the difference between CODs at maximum and minimum loads, is used because it removes residual stress effects and is related to the crack driving force, ΔK. As can be seen in Figure 3.4, the ΔCODs are similar in magnitude and increase almost linearly with distance from the crack tip for each fiber volume fraction. The similar near tip CODs at crack

arrest for each fiber volume fraction imply similar effective matrix stress intensities. It is apparent from the large CODs that at least some of the original bridged fibers are broken for vf37 and vf41#1.

3.1.3 Breaking Bridged Fibers

After the cracks arrested and ΔCODs were measured, the applied stress level was incremented to promote additional crack growth. Additional crack growth required breaking the bridged fibers nearest the crack mouth as evidenced by a sudden large increase in observed CODs. The applied stress required to break the bridged fibers nearest the crack mouth was 202, 219, and 225 MPa for vf15, vf37, and vf41, respectively. This difference in stress levels necessary to continue damage evolution after crack arrest is within 5% of their average 215 MPa value and less than the scatter of the incremented stress technique used here. In general, once a through-the-thickness crack arrested and then growth continued by incrementing the applied stresses, no further crack arrests were observed. However, one specimen (vf41#3), exhibited only moderate crack growth at elevated stresses and then again arrested. An applied stress of 541 MPa was required prior to apparent break of the fibers nearest the crack mouth as noted via large increase in mouth CODs. Consequently, breaking the bridged fibers

nearest the crack mouth is considered a key event in the life of these materials and will be discussed in more detail later. Table 3.3 summarizes several parameters relating to breaking the bridged fibers nearest the crack mouth. The fiber breakage stress was estimated using the fiber pressure model (to be presented later) and predicts a higher fiber break stress for fully bridged cracks.

The ΔK values applied when these bridged fibers nearest the crack mouth broke were 16, 23, and 20 MPa $m^{1/2}$ for each vf15, vf37, and vf41#1, respectively. The Vf41#3 sample required an applied ΔK of almost 50 MPa $m^{1/2}$ before the bridged fibers broke. A variation of 3 MPa $m^{1/2}$ probably approaches the scatter of the incremented stress technique used and consequently an applied ΔK of 20 MPa $m^{1/2}$ for continued crack growth may be considered representative for all fiber volume fractions, except the fully bridged case of vf41#3.

3.1.4 Post-Arrest Crack Growth

After crack growth recommenced, each fiber volume fraction behaved quite differently. The vf15 material experienced high growth rates until its rapid failure. The vf37 and, especially the vf41, demonstrated stable crack growth rates for very long periods prior to failure. Quantitative information will be presented later

along with the fractography results.

3.1.5 Fiber Breakage, Debonding, and Matrix Plasticity

In addition to a growing fatigue crack, many other damage mechanisms are active

and tend to control the fatigue crack growth behavior of these materials. These

mechanisms are fiber breakage, fiber/matrix debonding, and matrix plasticity.

Prior to and during crack arrest, a fully bridged crack generally exists with

minimal fiber damage ahead or behind the crack tip. However, it is likely that

some bridged fiber damage has occurred as shown by the larger than expected

ΔCOD data of Figure 3.4 for vf37 and vf41#1. After crack arrest, the

incrementally increased stress level breaks the fibers nearest the crack mouth and

the stress is redistributed among the remaining bridged fibers. This stress

redistribution breaks all of the remaining bridged fibers only in the vf15 material

because of the small number of bridged fibers. The vf37 and vf41 materials retain

from eight to sixteen bridged fibers (one or two fibers per ply) which parade

along with the propagating fatigue crack during stable crack growth[26]. To

determine the extent of fiber bridging just after breaking the bridged fibers

nearest the crack mouth, interrupted tests were polished down to the fibers.

Figure 3.5 shows that while the vf15 material had only broken fibers in the crack

wake, the vf41 material had the fibers nearest the crack tip intact. Fiber damage ahead of the crack tip does not occur until just prior to failure because of the low applied stress levels.

Fiber debond lengths were measured by optical metallography in two different fiber plies of the vf15 and vf41 materials. Figure 3.6 shows the fairly constant debond length with position from the notch root as measured on a fractured sample. The values of Figure 3.6 are half of the total debond length. It is seen that the debond lengths are generally independent of crack length. Results were similar for both plies measured. The average total debond length for both the vf15 and vf41 material is about 1950 microns while that of the vf37 is 2680 microns. The large magnitude of the vf37 debond lengths is surprising but consistent with that presented elsewhere[27] for the same material subjected to slightly higher stresses. Interrupted vf15 and vf41 tests have shown similar fiber debond lengths as those presented above for both intact and broken bridged fibers. Apparently, the fiber/matrix debond length is not greatly altered when the bridged fiber breaks and does not seem to be a strong function of applied stress level. However, References 20, 27, and 52 have all shown that the debond length decreases with distance from the crack tip for tests interrrupted at crack arrest. The current work considered debond lengths only after crack arrest. In both vf15

and vf41, a smaller amount of fiber debonding was observed at the fiber/matrix region ahead of the crack tip, as shown in Figure 3.7 for vf15, and is due to matrix plasticity as discussed next. This debonding ahead of the crack tip will increase the matrix stress level there, but should not drastically alter the energy based solutions presented later.

The extent of matrix plasticity was directly measured as a function of crack length using a novel heat treatment[28] which precipitates Ti-alpha phase onto slip bands which then etch preferentially, clearly showing regions of plastic deformation. The optical micrographs in Figure 3.8 show the observable slip bands, which provided the plasticity measurements shown in Figure 3.6 vs position from the notch root. Figure 3.6 shows that the length of slipped region (perpendicular distance from the crack plane) generally increases with increasing crack length. These measured values of matrix plasticity will be used later to estimate the effective matrix stress intensity[29]. Apparently, the variations in the extent of matrix plasticity shown in Figure 3.6 can be considered as variations in effective matrix stress intensity. Since slip bands end at grain boundaries, the resolution of this plasticity measurement is limited to grain size increments. A grain size about an order of magnitude smaller than that of these materials would have been more appropriate for some of the measurements presented.

In the region of crack arrest, the measured plastic zone size was near zero for all

fiber volume fractions and implies a minimal effective matrix stress intensity. It

is not clear why such a small plastic zone size is observed at crack arrest because

the crack was grown past that point by incrementing the applied stresses.

Interrupted tests have shown that matrix plasticity does occur beyond the fibers

at the crack tip for both vf15 and vf41, as shown in Figure 3.7 for vf15. This

matrix plasticity must occur in grains with the highest Schmid factors and is

believed to cause the debonding observed ahead of the crack tip. In vf41#3

ply#2, debonding, with associated matrix plasticity, was observed for the three

fibers ahead of the crack tip. Finally, the extent of plasticity was similar within

plies as between plies and suggests no strong local crack tip stress field

perturbation due to the high modulus fibers. The variation of stress in the vacinity

of a fiber, as predicted in the FEM results of Chapter 4, would require use of a

much smaller grain size.

3.1.6 Fractography

Each fracture surface was analyzed in the scanning electron microscope and is

shown in Figure 3.9. There were no obvious surface features to indicate the

region of crack arrest such as fiber bundles, change in fiber pullout length, or

matrix crack elevation. The average fiber pullout length was about seventy-five microns for the vf15 material and 150 microns for vf37 and vf41. This fiber pullout length is about an order of magnitude less than the measured debond lengths presented earlier. Although this short fiber pullout length may be attributed to fiber abrasion near the crack plane during cycling, there is no difference between the fiber pullout length in the crack growth and overload regions. The transition from stable crack growth to overload is clearly visible in the vf37 and vf41 materials as a change in contrast and indicates the critical crack length prior to catastrophic failure. The vf15 did not show a clear transition and required a consideration of fiber debond lengths, matrix plasticity, and fatigue striations before a critical crack length could be estimated. (The darker appearance opposite the notch for the vf15 fracture surface is due to sloping of the fracture surface and is not a behavior transition.) The critical crack length allows the composite toughness values to be calculated and are shown in Table 3.4.

All toughness values, except vf41#2, were calculated using handbook solutions as discussed in Appendix 2. Appendix 2 demonstrates the effect specimen and gripping geometry can have on choosing the appropriate stress intensity solution. Rational for the solution used here is also presented in Appendix 2. Vf41#2 was

fractured using grips which were rotationally constrained and required use of the

H/W=4.0 shape factor of Appendix 2. The composite toughnesses of 38, 223, and

450 MPa m$^{1/2}$ for vf15#1, vf37, and vf41#1, respectively, are very different from

the 100 MPa m$^{1/2}$ unreinforced matrix value. The 94 MPa m$^{1/2}$ toughness for

vf41#2 was determined using a rotationally constrained derived shape factor and

may be lower than vf41#1 because the higher applied stress value (343 MPa vs

225 MPa) reduces the fiber bridging size, or because the shape factor used to

compute the vf41#1 toughness was too large. The ratio of net section stress at

failure to the composite ultimate tensile strength was 0.31, 0.62, and 1.0 for vf15,

vf37, and vf41, respectively. Finally, the Mo-weave doesn't seem to influence crack

growth behavior at these stresses as it was rarely observed on the fracture

surfaces.

3.2 FATIGUE CRACK GROWTH ANALYSIS AND DISCUSSION

3.2.1 Analytical Fiber Pressure Model

A fiber pressure model will be used here to predict the fatigue crack growth

behavior in the presence of bridged fibers because it has been shown to be

accurate, computationally efficient, and does not require use of the fiber/matrix

interfacial friction shear stress [Ref 23]. The effect of the fibers bridging the crack faces can be modeled by applying a closure pressure in the bridged region as shown, with nomenclature, in Figure 3.10. The necessary equations for computing the composite stress intensity, $K^c(a/w)$, and CODs, $u(a/w,x)$, are given as in [Ref 23]:

$$K^c(\frac{a}{w}) = \sqrt{\frac{2}{\pi}}[\int_0^{a_0}\sigma^\infty H(a,x')dx' + \int_{a_0}^a(\sigma^\infty - c(x'))H(a,x')dx'] \qquad (3.1)$$

and

$$u(\frac{a}{w},x) = \frac{2(1-v_c^2)}{\pi E_c}(\int_x^a H(s,x)[\int_0^s p(x')H(s,x')dx']ds) \qquad (3.2)$$

where

x   =   distance from the free surface

E_c, v_c =   composite modulus and poisson's ratio (v_{12})

P(x')   = σ^∞ for $0<x'<a_0$ and $\sigma^\infty - c(x')$ for $a_0<x'<a$

H(a,x) =   Bueckner weight function (see Appendix 2)

c(x)   =   closure pressure distribution (see Appendix 2)

and

$$H(a,x') = \frac{1}{\sqrt{a-x'}}(1+m_1\frac{a-x'}{a}+m_2(\frac{a-x'}{a})^2)) \qquad (3.3)$$

with

$$m_1(\frac{a}{w}) = 0.6147+17.1844(\frac{a}{w})^2+8.7822(\frac{a}{w})^6 \qquad (3.4)$$

$$m_2(\frac{a}{w}) = 0.2502+3.2889(\frac{a}{w})^2+70.0444(\frac{a}{w})^6 \qquad (3.5)$$

Equation 3.1 gives the composite stress intensity as the difference between the applied stress intensity (σ^∞ terms) and the bridging effect (c(x) terms). This is easier to see if Equation 3.1 is rearranged as follows

$$K^c(\frac{a}{w}) = \sqrt{\frac{2}{\pi}}[\int_0^a \sigma^\infty H(a,x')dx' - \int_{a_0}^a c(x')h(a,x')dx'] \qquad (3.6)$$

Now the first term is simply the applied stress intensity and the second term is what must be subtracted because of fiber bridging. Hence,

$$K^c = K^{applied}-K^{bridging} \qquad (3.7)$$

In the bridged region, the closure pressure, c(x), is given by

$$c(x) = \sigma^\infty(\frac{w}{w-a_0}+\frac{6wa_0[0.5(w-a_0)-(x-a_0)]}{(w-a_0)^3}) \qquad (3.8)$$

and is zero elsewhere. It is clear from these equations that the solution obtained

38

depends heavily on the choice of the weight function and closure pressure distribution, both depending on specimen geometry and grip design. It is shown in Appendix 2 that this weight function predicts stress intensities which agree very well with handbook values [Ref 25] for a/w < 0.5 and that the handbook pinned grip formulation is appropriate here even though friction grips were used. Also presented in Appendix 2 is a justification of this closure pressure distribution and a new weight function which accounts for specimen and grip geometry.

Once the composite stress intensity, K^c, is known, the effective matrix stress intensity, K^m, is determined by [Ref 24]:

$$K^m = K^c \sqrt{\frac{E_m}{E_c(1-v_f)}} \qquad (3.9)$$

Note from Equations 3.2 and 3.9 above that the predicted crack opening displacements, u, and effective matrix stress intensity, K^m, are both dependent on fiber volume fraction.

This formulation predicts effective matrix stress intensities at the crack arrest of about 4 MPa $m^{1/2}$, as shown in Figure 3.2, and agrees well with the Ti-15-3 matrix threshold value of 4 MPa $m^{1/2}$ reported elsewhere[30]. Furthermore, the crack opening displacements predicted by this model agree with those measured for

each fiber volume fraction (see Figure 3.4). Since the crack face closure pressure, c(x), is known, the peak bridged fiber stresses can be computed by dividing c(x) by the fiber volume fraction [Ref 24] and these stresses are given in Table 3.3. The fiber break stresses are predicted to be 3.0, 1.3, and 1.2 GPa for vf15, vf37, and vf41#1, respectively. The fiber break stress of vf41#3 is estimated to be 2.7 GPa. As will be shown later using FEM, the bridged fiber break stress for a fully bridged crack must be near 3 GPa and the low values of vf37 and vf41#1 are likely due to fiber damage in the bridged region.

During post-arrest stable crack growth, where the bridged size was unknown, the CODs and crack growth rates were measured. The fiber pressure model was used to predict CODs and crack growth rates for different bridged lengths. Figure 3.11 shows that excellent COD and crack growth rate correlations are obtained for a bridged region containing sixteen fibers (two fibers per ply).

3.2.2 Fiber Volume Fraction Effects on da/dN vs Applied ΔK

Crack growth rate vs applied stress intensity curves are valid and useful for understanding and comparing fatigue crack growth behavior in monolithic materials with, for example, different grain sizes or alloy content. They will be

used here to understand and compare fiber volume fraction and stress history

effects in the Ti-15-3 composite. These types of curves allow use of the Paris law

$$\frac{da}{dN} = B(\Delta K)^g \qquad\qquad (3.10)$$

over the linear portion of the curve where B is a constant and g is the slope of

the curve on a log-log plot and called the growth rate exponent [Ref 29].

Idealized da/dN vs applied ΔK curves are shown in Figure 3.12 for the three fiber

volume fractions. Also shown is the unreinforced Ti-15-3 data. The much lower

composite crack growth rates, compared to the unreinforced matrix, are a result

of bridging fibers. The similar applied ΔKs of about 20 MPa $m^{1/2}$ break the

bridged fibers nearest the crack mouth for each fiber volume fraction and drasti-

cally increase the crack growth rates. The decrease in post-arrest growth rate

exponents and increase in composite toughness compared to the unreinforced

matrix are easy to explain for the higher fiber volume fraction materials because

of the additional bridged fibers. However, the increase in the growth rate

exponent and decrease in the composite toughness compared to the unreinforced

matrix for the vf15 material is more difficult to understand. Apparently, once the

leading bridged fibers break in vf15, the stress redistribution breaks all remaining

bridged fibers leaving an unbridged crack. It will be shown next that this can

occur in any fiber volume fraction if the applied stress level is high enough.

3.2.3 Stress Level Effects on da/dN vs Applied ΔK

An idealized da/dN vs applied ΔK curve for the vf37 material subjected to

different stress histories is shown in Figure 3.13. Also shown is monolithic Ti-15-3

data. This idealized da/dN vs applied ΔK curve was constructed using the current

data for 118 MPa applied stress range and the data provided in Reference 27 for

the 198 and 280 MPa applied stress ranges. Stress ranges above 280 MPa are

speculation. Three distinct regions can be observed. Region III is that region

where crack arrest occurs and is bounded by the maximum applied stress range

which permits bridging (280 MPa) and its associated da/dN vs applied ΔK profile.

Cracks grown and arrested at stresses less than this upper bound (minimum is 118

MPa) will arrest at a lower ΔK and require stress increases until the critical ΔK

($24 \text{ MPa m}^{1/2}$) is reached. Since these stress increases are not accompanied by an

increase in da/dN until some of the bridged fibers are broken, a horizontal line

on the da/dN vs applied ΔK curve results. For the case of a fully bridged crack

in the higher fiber volume fraction materials, such as vf37 and vf41, this horizontal

line may extend for over $30 \text{ MPa m}^{1/2}$ (vf41#3). Regardless of the applied stress

range prior to crack arrest, behavior at arrest and post arrest will be identical (including toughness) if the same stress range increments are used to break the bridged fibers. The increase in applied stress increases both the applied stress intensity and the reduction due to fiber bridging. Until bridged fibers break, the effective matrix stress intensity remains at or below threshold. An increase in the fiber/matrix interfacial shear stress with applied stress via the shear-lag model is used to explain the stress effect on fiber bridging [Ref 51, 52].

Region II is that region where the applied stress level is too high for arrest but low enough to allow a bridged ligament to parade with the propagating fatigue crack. In this region the growth rate exponent and composite toughness will be improved over the unreinforced matrix but the amount of improvement is stress range dependent. An initial negative growth rate exponent is necessary for Region II behavior to develop and only occurs at initial crack growth rates less than about 50×10^{-9} meters per cycle. If the applied stress range is such that the initial crack growth rates are greater than 50×10^{-9} meters per cycle, Region I behavior is observed which demonstrates severe degradation in crack growth rate exponent and fracture toughness when compared to the unreinforced matrix. This occurs because the stress level is too high for fiber bridging to develop, and the resulting unbridged crack demonstrates severely degraded properties. Apparently, if the

crack growth rate of 50×10^{-9} meters per cycle is exceeded, which probably occurs at an applied stress of about 350 MPa for this material and geometry, catastrophic failure will soon follow if the current applied ΔK is maintained. Furthermore, since composite toughness depends on the extent of fiber bridging, published toughness values have no meaning without knowing the stress history and associated bridging size prior to failure. In Chapter 6 the similarity between these three regions and those identified on a stress or strain vs life curve for understanding low cycle fatigue in composites will be discussed.

3.2.4 Debond Length and Interfacial Shear Strength

The longer debond length of the vf37 material, shown previously in Figure 3.6, implies a weaker fiber/matrix interface than the other fiber volume fractions considering the similar applied stress levels. This contradicts the fiber pushout results presented in Chapter 2 which gave the interfacial shear strength of the vf37 material as between that of the vf15 and vf41. Furthermore, it is not clear why the vf15 and vf41 materials had similar debond lengths but very different interfacial shear strengths. Finally, the very different measured fiber/matrix debond lengths resulted in similar fiber pullout lengths. These findings suggest that there may be very little correlation between the fiber/matrix interfacial shear

strength values obtained from fiber pushout tests and actual composite behavior.

3.2.5 Modeling Fiber Volume Fraction Effects on FCG and Toughness

Just as in monolithic materials, crack growth in composites is governed by having adequate energy available for the creation of additional surface area. For composites subjected to Mode I loading, this elastic strain energy, or energy release rate, G^c, must be the sum of the contributions from the fibers, G^f, and the matrix, G^m. It is assumed that the energy required for fiber matrix debonding is small compared to that required to break the matrix. It is also assumed that the fiber/matrix debonding ahead of the crack tip does not influence the result because this debonding is due to matrix plasticity which, in turn, is part of the matrix fracture process. Since the fiber and matrix must be in force equilibrium, we can multiply both sides of the ROM stress expression by the applied composite strain

$$\sigma_c \varepsilon_c = \sigma_f \varepsilon_c V_f + \sigma_m \varepsilon_c V_m \qquad (3.11a)$$

Now, realizing

$$\varepsilon_c = \frac{\sigma_c}{E_c} = \frac{\sigma_f}{E_f} = \frac{\sigma_m}{E_m} \qquad (3.11b)$$

we can write

$$\frac{\sigma_c^2}{E_c} = \frac{\sigma_f^2}{E_f}V_f + \frac{\sigma_m^2}{E_m}V_m \qquad (3.11c)$$

Multiplying by πa and using

$$G = \frac{\sigma^2 \pi a}{E} \qquad (3.11d)$$

results in the expression

$$G^c = G^f V_f + G^m V_m \qquad (3.11)$$

For plane stress

$$G^i = \frac{(K^i)^2}{E_i}, \quad i = c, f, m \qquad (3.12)$$

and hence,

$$\frac{(K^c)^2}{E_c} = \frac{(K^f)^2}{E_f}V_f + \frac{(K^m)^2}{E_m}V_m \qquad (3.13)$$

For the case of fiber bridging, the strain energy in the fibers is not released and

$$K^c = K^m \sqrt{\frac{E_c(1-V_f)}{E_m}} \qquad (3.14)$$

This expression is identical to that given by McCartney [Ref 24] and allows prediction of the effective matrix stress intensity, K^m, for an applied composite stress intensity, K^c. It is worth pointing out that the expression inside of the

46

radical is quadratic in vf and that the ratio of the composite to matrix stress intensity, K^c/K^m, is maximum for a fiber volume fraction of 0.36 in the SCS-6/Ti-15-3 composite system. Figure 3.14 shows the mild maximum of Equation 3.14, which is valid for both fatigue and monotonic loading conditions. Also shown in Figure 3.14 is K^c/K^m scaled linearly with the ratio of composite to matrix modulus values (ie, $K^c/K^m = E_c/E_m$, Ref 22). Note the large difference in K^c/K^m for these two methods using SCS-6 and Ti-15-3 properties.

This large difference is surprising because both methods appear in the literature, but seldom together. Apparently, the energy based method developed here, and in Reference 24, is the correct one because it successfully correlates the crack growth rate and ΔK data, as discussed previously. Another way to experimentally verify the energy based expression is to compare the ratio of applied stress intensity at crack arrest for vf15 and vf41. The experimental data (Table 3.1) shows that ΔK at crack arrest is 11.5 and 16.5 MPa m$^{1/2}$ for vf15 and vf41, respectively. The ratio of the vf41 to vf15 ΔK at arrest is 1.45. Since the closure pressure, c(x), scales linearly with applied stress (Equation 3.8) this 1.45 ratio becomes 1.10 when multiplied by 126 MPa/165 MPa (stress ranges at crack arrest). This 1.10 ratio compares favorably with the 1.05 vf41 to vf15 ratio predicted by the energetically consistant method but is well below the 1.59 value

47

predicted by scaling linearly with modulus.

As this ratio, K^c/K^m, becomes greater than unity with increasing fiber volume fraction, a higher composite stress intensity must be applied to achieve the same effective matrix stress intensity. Since fatigue crack growth behavior of these materials is matrix controlled, the greater this ratio the better the resulting composite properties. For the SCS-6/Ti-15-3 composite, the maximum value of K^c/K^m is 1.20 for a 0.36 fiber volume fraction composite and predicts a 20% improvement in composite fatigue crack growth properties over that of the unreinforced matrix without considering the effects of fiber bridging. This may explain why the composite stress intensity range, ΔK, required for crack arrest was consistently higher for the higher fiber volume fraction materials. Since fatigue crack growth properties influence low cycle fatigue results, this finding suggests minimal improvement in LCF properties with increasing fiber volume fraction over 0.36 for the SCS-6/Ti-15-3 composite as will be discussed in Chapter 6. The K^c/K^m ratio scaled linearly with modulus increases monotonically with fiber volume fraction up to a suspiciously high 270% improvement in properties. How residual stresses may change this effect for monotonic loading is also shown in Figure 3.14, and discussed next.

The above formulation does not consider how the effective matrix stress intensity may interact with residual stresses in the matrix material. One way to include residual stresses is to return to the definition of the strain energy release rate for brittle materials

$$\sigma_{fracture}^{monolithic} = \sqrt{\frac{E\ G_{critical}^{monolithic}}{\pi a}} \tag{3.15}$$

where this expression is satisfied at fracture. The failure strain of about 1% for these composite materials supports the assumption of brittle type behavior. In addition, the extremely short fiber pullout lengths observed on the fracture surface, as discussed earlier, imply minimal energy dissipation (and hence toughening) by fiber sliding. For the matrix material of a composite with residual stresses, however, the effective stress at fracture has been reduced by an amount equivalent to the residual stress, or

$$\sigma_{fracture}^{monolithic} - \sigma_{residual}^{m} = \sqrt{\frac{EG^{mr}}{\pi a}} \tag{3.16}$$

This expression can be solved for the remaining strain energy which can be stored by the composite matrix prior to fracture, G^{mr}, and used to estimate the ratio of energy release rate in the composite to that in the unreinforced matrix. Hence

$$\frac{G^{mr}}{G^{m}} = (1-\lambda)^2 \tag{3.17}$$

49

where λ is the ratio of the average effective residual stress in the matrix to the unreinforced matrix fracture stress. Using the residual stress reduced G^{mr} of Equation 3.17 as G^m in Equation 3.11 and again neglecting the fiber terms results in

$$G^c = G^m V_m (1-\lambda)^2 \qquad (3.18)$$

where G^c corresponds to the additional elastic energy which can be imposed to the composite prior to exceeding the critical strain energy release rate of the matrix, G^m. Using Equation 3.12 provides

$$\frac{(K^c)^2}{E_c} = \frac{(K^m)^2}{E_m} V_m (1-\lambda)^2 \qquad (3.19)$$

or

$$K^c = K^m (1-\lambda) \sqrt{\frac{E_c (1-v_f)}{E_m}} \qquad (3.20)$$

which is essentially the superposition of the applied and residual stress intensities onto the matrix. From the data of Table 3.5 we can approximate the value of λ as a function of fiber volume fraction, $\lambda = 0.96(V_f)^{1/4}$, and again plot K^c/K^m vs fiber volume fraction in Figure 3.14. Apparently, residual stresses decrease the composite toughness with an increase in fiber volume fraction even after

50

fiber/matrix modulus effects are included. While the average effective residual stress values were used here, this finding does not change using the maximum longitudinal matrix residual stresses. Since the residual stress is monotonic, ΔK should not be affected. Rearranging Equation 3.20,

$$K^c = K^m \sqrt{\frac{E_c(1-V_f)}{E_m}} - K^m \lambda \sqrt{\frac{E_c(1-V_f)}{E_m}} \qquad (3.21)$$

where $K^m \lambda$ is the residual stress intensity in the matrix, $K^m_{residual}$. Or,

$$K^m = K^c \sqrt{\frac{E_m}{E_c(1-V_f)}} + K^m_{residual} \qquad (3.22)$$

Now for fatigue crack growth, ΔK is the important parameter and can be obtained by subtracting Equation 3.22 at the maximum and minimum applied stresses

$$\Delta K^m = \Delta K^c \sqrt{\frac{E_m}{E_c(1-V_f)}} \qquad (3.23)$$

The residual stress term cancels out and apparently does not influence fatigue crack growth other than to change the R-ratio.

Without fiber bridging, Equation 3.20 can be used to estimate how residual stress influences the composite toughness. Because this formulation was energy based,

the effective stress is the most appropriate one and provides $\lambda=0.61$, 0.73, and

0.75 for vf15, vf37, and vf41, respectively. Using the remaining values of Table 3.5,

provides estimated (unbridged) composite toughness values of 44, 32, and 30 MPa

$m^{1/2}$ for vf15, vf37, and vf41, respectively. The estimated composite toughness of

44 MPa $m^{1/2}$ for the vf15 material compares well with the measured 38 MPa $m^{1/2}$.

Even though the vf15 material appears to be the only fiber volume fraction which

fails without active fiber bridging, the possible plane strain conditions in this

thicker composite, as discussed next, may also be partly responsible for the lower

measured toughness value.

3.2.6 Interpretation of Measured Plastic Zone Sizes

As mentioned earlier, a metallographic technique was used for direct

measurement of the extent of matrix plasticity. This matrix plasticity is considered

the plastic zone size, r_p, and can be used to estimate the effective matrix stress

intensity. This same technique has been used previously [Ref 2] for monolithic Ti-

15-3 in thicker samples with excellent correlation between the measured plastic

zone size and that predicted by the equation

$$r_p = \frac{1}{6\pi}\left(\frac{K_{max}}{\sigma_{YS}^m}\right)^2 \tag{3.24}$$

where K_{max} is the maximum applied cyclic stress intensity and σ^m_{YS} is the yield stress of the matrix material. This expression is the standard equation for the monotonic plastic zone size under plane strain conditions directly in front of the crack tip ($\theta=0$) in an infinite body. The plastic zone measured in the current work and that of Reference 2, however, is actually at right angles to the crack plane ($\theta=90$) and has finite dimensions which require use of the shape factor (Appendix 2). Since excellent correlation between predicted and measured data in Reference 2 was obtained without these adjustments, they will not be used here. The smaller fatigue plastic zone experiencing reversed plasticity does not significantly alter this monotonic plastic zone size[31,32]. Consequently, the standard equation for estimating the plastic zone size under plane stress conditions is:

$$r_p = \frac{1}{2\pi}\left(\frac{K_{max}}{\sigma_{YS}^m}\right)^2 \tag{3.25}$$

and will be used to consider the stable crack growth and overload behaviors.

Even though the extent of matrix plasticity varies greatly with position, an average plastic zone size can be approximated during stable crack growth (Figure 3.6) as

200, 1182, and 735 microns for vf15, vf37, and vf41, respectively. Equation 3.25 can be rearranged to solve for K_{max} and predicts a monotonic effective matrix stress intensity of 26, 61, and 48 MPa for vf15, vf37, and vf41, respectively. These high matrix stress intensities would result in crack growth rates far greater than those actually observed. As discussed in the previous section, the residual stresses would only influence the maximum stress intensity and not ΔK, which drives crack growth.

The matrix stress intensity imposed by the residual stress can be subtracted from the values predicted using the measured plastic zone size to provide an estimate of the maximum applied matrix stress intensity

$$K^m_{applied} = K^m_{measured} - K^m_{residual} \qquad (3.26)$$

solving Equation 3.25 for K and using the matrix yield stress for $K^m_{measured}$ and the matrix residual stress for $K^m_{residual}$ results in

$$K^m_{applied} = (\sigma^m_{YS} - \sigma^m_{residual})\sqrt{2\pi r_p} \qquad (3.27)$$

The maximum applied matrix stress intensity can be considered as the stress intensity range with less than 10% error for an R-ratio of 0.1. Using the average effective matrix residual stress values given in Table 3.5 results in the following estimates of $\Delta K^m_{applied}$: 7.8, 11.2, and 7.5 MPa $m^{1/2}$ for vf15, vf37, and vf41, respec-

54

tively. The vf37 and vf41 values are in close accord with those da/dN and ΔK data predicted from the fiber pressure model with about sixteen fibers bridged (two fibers per row) for the ΔCOD vs position from the crack tip in Figure 3.11. Note the good agreement of crack growth rates among the data, the fiber pressure model, and the matrix plasticity estimation. Apparently the matrix residual stresses are not significantly reduced during mechanical cycling at these stress levels.

To estimate the fracture toughness via plastic zone size measurements the residual stresses must again be included. The average plastic zone sizes at fracture (Figure 3.6) are 250, 1800, and 1400 microns for vf15, vf37, and vf41, respectively. These values allow an estimation of the matrix stress intensities at fracture of 28, 76, and 67 MPa $m^{1/2}$ for vf15, vf37, and vf41, respectively. The average 72 MPa $m^{1/2}$ matrix stress intensity at fracture for vf37 and vf41 is near the 100 MPa $m^{1/2}$ toughness value established for the unreinforced Ti-15-3 matrix. However, if the shape factor (Appendix 2) for a rotationally constrained grip with L/W=4 is used along with the 1.46 correction factor for θ=90, the average predicted matrix stress intensity at fracture for vf37 and vf41 becomes 105 MPa $m^{1/2}$. This finding suggests a note of caution when interpreting the high composite toughness values predicted earlier using the handbook (pinned grip) solutions for a/w > 0.5. Finally, the surprisingly low estimated value of the matrix stress intensity at

fracture for vf15 (28 MPa m$^{1/2}$) suggests that this thicker specimen (2.9 mm in vf15 vs 1.5 mm in vf41) experiences plane strain conditions. Using the plane strain formulation (Equation 3.24) boosts the effective matrix stress intensity at fracture for vf15 material to 50 MPa m$^{1/2}$. This is still lower than expected.

A previous study of thickness effects on fatigue crack growth in Ti-15-3 has shown a 50% increase in the fatigue crack growth rate exponent as the thickness increases from 1.27 mm to 2.79 mm with no additional increase for a 7.1 mm thick sample [Ref 2]. This thickness effect was partially attributed to specimen thickness but an increase in grain size with thickness confused the issue. Although not readily apparent on the fracture surfaces in Figure 3.9, at overload the vf15 fracture morphology assumed more of a classical plane strain appearance (ie, slope in the width direction) while the vf37 and vf41 appeared more like plane stress (ie, slope in the thickness direction)[33]. The limited matrix plasticity measured in the vf15 material of the current work is difficult to explain and may be primarily to prevailing plane strain conditions of the thicker plate, which will also reduce the expected toughness of the vf15 material. However, since the fiber/matrix interfaces are weak and easily separate, plane strain conditions would not be expected.

The technique of measuring the extent of matrix plasticity was extended to allow direct measurement of residual stresses as presented in Appendix 3. In Appendix 3, the change in slope of a stress-strain curve for this same material with a 0.34 fiber volume fraction correlates well with the onset of matrix plasticity. The agreement between predicted and measured matrix plasticity in Appendix 3 lends credibility to this approach in using residual stresses to estimate effective stress intensities from the measured matrix plasticity.

3.2.7 Fiber Breakage Stress

As presented earlier the key event in the life of these materials is when the bridged fibers begin to break. Previous attempts to estimate the stress level in the fibers nearest the crack mouth when they break for the vf37 material by using the fiber pressure model predicted a breakage stress of less than 1.7 GPa [Ref 27]. It was thought that fiber strength degraded with cycles since this breakage stress was much lower than the 2.7 GPa in-situ strength of the fiber. The fiber breakage stresses of this study were 3.0, 1.3, and 1.2 GPa for both vf15s, vf37, and vf41#1, respectively. However, vf41#3 had an estimated fiber breakage stress of 2.7 GPa. Since fibers from each fiber volume fraction were subjected to a similar number of cycles, cyclic degradation of fiber strength cannot be the reason that the vf37

and vf41#1 fiber breakage stresses were so low. Instead, an alternate explanation may better address this low fiber pressure model prediction of fiber breakage stresses.

There may be a lower fiber volume fraction of fibers bridged by the crack because those damaged at the notch root must be neglected. Using the fracture surface micrographs, the number of fibers damaged at the notch root were determined and subtracted from the total number of bridged fibers to reduce the bridged fiber volume fraction. This process increased the vf15 fiber breakage stress only slightly but almost doubled the predicted vf37 and vf41#1 values, which then approaches the approximately 2.7 GPa fiber breakage stresses observed for the other tests. Grips effects and periodicity of fiber spacing within rows (Appendix 1) may have also influenced these results as discussed shortly.

The small but persistent increase in fiber breakage stress with a decrease in composite fiber volume fraction is likely due to the retained compressive fiber residual stresses after matrix cracking. It was shown in Chapter 2 that the compressive residual stresses in the vf15 fibers is twice that of the vf37 and vf41 which could result in a higher apparent strength. It will be shown in Chapter 4 that these residual stresses are not completely relieved in the bridged fibers. In

Chapter 4, a sophisticated macro/micro finite element model was generated to study crack growth in the presence of bridged and debonded fibers. Figure 3.15 shows the mesh used in the analysis with bridged fibers. The magnitude of benefit derived from bridged fibers on fatigue crack growth behavior is dependent on the fiber breakage stress, which is higher in the vf15 material because of the larger retained compressive residual fiber stresses.

As mentioned earlier, this fiber breakage stress is estimated from the fiber pressure model by dividing the closure pressure distribution, $c(x)$, by the fiber volume fraction [Ref 24]. For the specimen geometry used here and a 210 MPa applied remote stress

$$c(x) = 559-98x \qquad (3.28)$$

where x is measured in millimeters from the free surface (ie, at the edge of the plate which has the notch mouth) and $c(x)$ is in units of MPa. Dividing Equation 3.28 by 0.1, 0.15, 0.25, 0.35, and 0.45 estimates how the bridged fiber stresses vary with fiber volume fraction for a fully bridged crack. Figure 3.16 shows that the maximum bridged fiber stresses occur at x=1 (ie, at the notch root). Clearly, the bridged fiber stress of 4600 MPa for vf10 is greater than the 2700 MPa in-situ strength of the SCS-6 fiber [Ref 6,7]. Apparently, a fiber volume fraction of 0.15 is the minimum for which fiber bridging, and resulting crack arrest, can be

expected to occur. At fiber volume fractions less than 0.15, the maximum bridged fiber stress exceeds the strength of the SCS-6 fiber before the bridging mechanism is fully activated.

The maximum bridged fiber stresses of 1317 and 1024 MPa from Figure 3.16 for 0.35 and 0.45 fiber volume fractions, respectively, are well below the 2700 MPa in-situ strength of the SCS-6 fiber. It is believed that the applied stress of about 210 MPa which was suspected of breaking these fibers at such low stresses actually induced 2700 MPa fiber stresses in a lower fiber volume fraction of bridged fibers of the vf37 and vf41#1 experiments. It is likely that the fibers in the bridged region were either damaged from the notching process or influenced by the grips used for those experiments, which may have imposed a bending moment when clamped. However, these same grips did not damage the notch region fibers in vf15#1 as it demonstrated full bridging.

The same process used to estimate the bridged fiber stress allows a prediction of the applied stress level required to induce a 3000 MPa maximum bridged fiber stress in the 0.35 and 0.45 fiber volume fractions. The estimated applied stress required to break the bridged fibers of a fully bridged crack are 210, 490, and 630 MPa for 0.15, 0.35, and 0.45 fiber volume fractions, respectively. For vf41 the

estimated applied stress of 560 MPa necessary to break the bridged fibers agrees very well with the 541 MPa measured value (Table 3.3). Because the applied stress levels necessary to induce a 3000 MPa bridged fiber stress in a fully bridged crack increase with fiber volume fraction, the resulting fiber stress distribution as a function of position from the notch is identical for all fiber volume fractions just prior to fiber fracture. This implies that for a fully bridged crack, breaking any bridged fibers may break all bridged fibers and the observed post-arrest fatigue crack growth and toughness behavior may be as poor as the that observed in vf15#1. In fact, the vf41#2 sample behaved much like vf15#1 after breaking the bridged fibers because the specimen broke before the test could be interrupted for metallography. This behavior was anticipated for vf15#2, and the test was interrupted accordingly. But the higher applied stresses of vf41#2 did not allow the slow stable crack growth observed for long crack lengths in vf41#1.

FINITE ELEMENT MODELING OF BRIDGED FIBER STRESSES

In previous chapters experimental and analytical results of the effect of fiber

bridging on fatigue crack growth behavior in fibrous unidirectional composites

were presented. It was shown that the observed reduction in crack growth rates

is matrix controlled with fiber induced perturbations. The bridging fibers impart

a closure pressure to the crack faces, reducing the effective matrix stress intensity

until it approaches the matrix threshold at crack arrest. The fiber pressure model

used to predict this type of behavior agreed well with those experimental results

as a function of the fiber volume fraction. However, there are some remaining

questions about the use of this model. How realistic is the assumed fiber pressure

distribution? Why is the predicted bridged fiber breaking stress below the in-situ

fiber strength? How accurately is the effect of fiber volume fraction modeled?

What is the role of residual stresses on bridged fiber breakage? How do debond

lengths affect fiber stresses and crack opening displacements? Answers to these

questions have proved difficult to obtain experimentally, and reliable analytical models cannot be advanced without a better understanding of the mechanisms involved.

Finite element methods (FEM) are a very powerful tool for these types of problems and have been used to predict residual stresses[34] and tensile behavior of laminates[35]. FEM has also been used to show a decrease in matrix stress intensity due to bridged fibers[36] and that a significant bending stress exists in the bridged fibers of a single edge notch specimen geometry[37]. Finite element methods will be used here to address some of these unanswered questions. The techniques employed in the current work are different and, in some cases, more sophisticated than earlier efforts by other researchers.

4.1 FINITE ELEMENT MODELS

4.1.1 Mesh Definition

Three dimensional finite element models were generated for the vf15 and vf37 geometries with the unit cell dimensions identical to those of Chapter 1 using the PATRAN (pre and post-processing, Ref 12) and MARC (solver, Ref 13) finite

element software and executed on the Cray YMP. Both models had geometries representative of the experiments, with a width of five millimeters and a gage length of twenty millimeters, although longitudinal symmetry requires only half of the length to be modeled. The notch was one millimeter deep. A region of discrete fiber and matrix was placed ahead of the notch and orthotropic material was used elsewhere. The vf15 and vf37 meshes are shown in Figure 4.1 and Figure 4.2, respectively, and were constructed with the eight noded brick element. Note that even though the actual composite has eight plies, only half of a ply needed to be modeled because of symmetry. The vf15 mesh employed 3312 nodes and 2258 elements while the vf37 had 3921 nodes and 2648 elements. Both meshes required two thousand boundary constraints to properly model the material behavior. The larger (vf37) mesh had over ten thousand degrees-of-freedom and required 2700 CPU seconds for execution on the Cray with 19 mega-words memory for in-core solution. All executions were performed with the elastic-plastic option activated for the matrix and used the orthotropic material properties in Table 4.1. The fiber and matrix properties used were identical to those of Table 2.2 except that the SCS-6 CTE at 25C and 300C were increased from 2.0 and 2.5×10^{-6}/C to 3.0 and 3.5×10^{-6}/C. The fiber was considered as elastic until failure.

4.1.2 Boundary Conditions

The front and back faces/sides were tied together such that all nodes on those faces were forced to move together in the y direction (ie, through the thickness). See Figure 4.3. This is frequently referred to as generalized plane strain conditions. The bottom (notch) side of the model was a plane of symmetry restrained from motion in the z direction (parallel with fibers) everywhere except in the notch. One node was completely constrained to prevent rigid body motion of the model. The remaining nodes were free to move in response to a pressure applied at the top surface of the mesh (+z direction), thereby imposing a tensile load on the sample. An applied pressure was used, instead of an applied displacement, because the specimen grips were not rotationally constrained as discussed in Appendix 2.

4.1.3 Mesh Refinement and Matrix Plasticity

These models were specifically generated to study the mechanisms of bridged fiber breakage, because it was shown in Chapter 3 to be the critical event in the life of these materials. The current effort was not an attempt to model fatigue crack growth using nodal release schemes and matrix property evolution ahead,

or behind, the crack tip. However, the near tip mesh refinement used here satisfies a criterion established for that type of work[38] by having a nodal spacing less then a tenth of the expected plastic zone size for the unbridged case. The ratio of largest to smallest element dimension was about 150:1. Because the crack was not 'grown' into the mesh, but rather added, this model is actually more of a tensile simulation than one of fatigue. Including fatigue would require excessive computer resources and would not drastically alter the results, because the Ti-15-3 matrix does not significantly work harden. Matrix plasticity induced crack closure effects were not modeled and are less critical in a tension-tension experiment, as was used in this work. Ahead of the crack tip, the matrix yield condition was modeled using the von Mises yield criteria with isotropic hardening.

4.1.4 Crack Tip Singularity

Originally, twenty-noded brick elements were considered for quarter point singularity[39], but the resulting mesh became too large. However, the inverse square root stress singularity with position from the crack tip imposed by quarter point elements is only valid for brittle materials and may not have been appropriate because of the observed matrix plasticity. Even though quarter point singularity elements were not used here, the mesh is probably adequate for

capturing most of the crack tip stresses, especially since the stress intensity at crack arrest is very small because of the bridged fibers. However, this modeling effort was not an attempt to capture all of the crack tip stress field. Instead, of interest here are the mechanisms of breaking the bridged fibers and the subsequent stress redistribution.

4.1.5 Debonding

The fiber/matrix interface is very weak and debonds as the crack passes the unbroken fibers. The actual process of debonding is a topic of active research and will not be pursued here. Instead, the debond is simulated by constraining the fiber and matrix nodes to the same displacements in the crack (x,y) plane. Relative motion along the fiber (z) is completely unrestrained. Implementing these conditions required extensive use of the multi-point constraint feature in the MARC software. In effect, the crack plane end of the fiber is in a 'can' of matrix material from which it can easily slide in and out. Beyond the debond region, the fiber and matrix are perfectly bonded. Success of this entire model depended on implementing this type of debond scheme because an attempt to use a concrete element at the interface to allow cracking did not provide realistic behavior. The non-linear contact elements, like those used in References 35 and 37 , have been

tried previously at NASA and would require enormous amounts of CPU for a mesh this size. Finally, gap elements are another possibility but have difficulty converging and are very labor intensive to implement. The method of debonding used here worked very well, was computationally efficient, and fairly easy to implement. What isn't clear, however, is how long this debond length should be. The average measured fiber debond lengths in the region of crack arrest were 600, 1250, and 750 microns for vf15, vf37, and vf41, respectively, but fiber motion was at least partially constrained by fiber/matrix friction.

The bridged fiber will be considered as a structural member having an effective debond length, L_{eff}, which is governed by the interfacial friction stress, τ, and the difference between longitudinal fiber stresses at the crack and far removed. This effective debond length arises because a structural member of a given length deflects less (ie, has a higher apparent stiffness) if friction is active. In other words, a longer member with friction will deflect the same amount as a shorter member which has no friction. The value of this effective debond length can be estimated by a force balance in the direction of the fiber

$$\Sigma F = 0 = +2\pi R\tau L_{\textit{eff}} + \pi R^2 \sigma_{remote}^{fiber} - \pi R^2 \sigma_{atcrack}^{fiber} \qquad (4.1)$$

where

L_{eff} = effective debond length

R   = fiber radius (= 72 microns)

τ = fiber/matrix interfacial friction stress (= 80 MPa)

σ_{atcrack} = longitudinal fiber stress at the crack (= 1200 MPa)

σ_{remote} = remote longitudinal fiber stress (= 400 MPa)

The fiber radius and interfacial friction stress were given in Chapter 2 and the longitudinal fiber stress at the crack plane comes from the fiber pressure model or this finite element model (vf37 and a 210 MPa applied stress). The longitudinal fiber stress remote from the crack plane can be estimated using rule-of-mixtures or a finite element model (vf37 and a 210 MPa applied stress).

Equation 4.1 can be solved for the effective debond length and becomes

$$L_{\text{eff}} = \frac{(\sigma_{\text{atcrack}}^{\text{fiber}} - \sigma_{\text{remote}}^{\text{fiber}})R}{2\tau} \qquad (4.2)$$

Using the vf37 values above, an effective debond length of 360 microns is predicted. This estimated effective debond length of 360 microns is about half the measured values for the vf15 and vf41 materials and a third of that measured for the vf37 material. In general, the fiber stress near the crack plane can be given as a function of fiber volume fraction (Equation 3.8) and the remote fiber stress by a ROM expression like that previously used for the matrix (Equation 2.2). The

resulting expression for the effective debond length can be approximated to within

10% for 0.15<vf<0.45 by

$$L_{eff} \sim \frac{0.8R\sigma^\infty}{V_f \tau} \qquad (4.2a)$$

Since the applied stress will be held constant at 210 MPa, the effective debond

length increases with decrease in fiber volume fraction. The effective debond

length for vf15 is 860 microns: similar to the measured values. However, since the

fiber volume fraction effects are of primary interest here, the same effective

debond lengths will be used for both models to aid comparisons.

Instead of these 360 and 860 micron effective debond lengths, a primary debond

length of 582 microns was used here because it was believed to be more represen-

tative of the actual value. There were a few reasons for this. First of all, the

interfacial friction stress was determined using fiber pushout tests whereas the

experiment is a pullout-type test, and hence the fiber experiences Poisson's

contraction rather than Poisson's expansion. Consequently, a lower value of

friction stress, and a higher debond length, should be employed. Secondly, the

friction stress is likely to be relieved near the crack plane due to fatigue loading

and again implies a longer effective debond length. Third, the finite element mesh

only allows debonding at nodal locations, which are at 317, 582, and 1000 microns

from the crack plane for these meshes. The 582 micron debond length also seemed reasonable because it was between the vf15 and vf37 predicted value and closer to the measured values. It will be shown later, however, that this 582 micron debond length over predicts the CODs by a factor of two when compared to both the vf15 and vf41 COD data. A 317 and 1000 micron effective debond length were later used and the 317 micron effective debond length better matches the experimental COD data for vf15 and vf37.

4.1.6 Crack Length

After inducing residual stresses, the appropriate orthotropic and matrix material symmetry plane nodes were released from the notch root to the desired arrested crack length. Since fiber volume fraction effects were of interest, the same 1632 micron crack length was used for both models, which bridged two and three fibers for the vf15 and vf37 material, respectively. This arrested crack length is longer than some of those observed experimentally but was used so a bridged fiber could be and permit studying the stress redistribution on the remaining bridged fibers. In addition, the mesh was generated with the highest nodal density in the matrix between the fibers so allowable crack lengths were in increments of the unit cell dimension. Since the crack lengths, fiber and matrix properties, and applied

stresses are the same for both FEM models, fiber volume fraction and debond length effects can more clearly be discerned.

4.2 RESULTS AND DISCUSSION

Each mesh was subjected to a 675 C temperature change in five increments to induce residual stresses. These five steps are considered adequate because it was shown in Chapter 2, and confirmed again here, that residual stress induced matrix plasticity does not occur in the vf15 and vf37 materials upon cooldown. After cooling, the orthotropic and matrix material nodes from the notch root to the desired 1632 micron crack length were released. Next, a stress of 210 MPa was applied in five increments. Five increments are considered an adequate number because the matrix plasticity is confined to a small region near the crack tip. This 210 MPa applied stress level was shown in Chapter 3 to be the stress level which recommenced crack growth after crack arrest. Finally, the symmetry nodes of the bridged fibers nearest the crack mouth were released to simulate fiber breakage. In what follows, each of these steps will be presented sequentially for the vf15 and vf37 fiber volume fractions using an effective debond length of 582 microns. Associated displacement profiles and longitudinal and von mises stress contours will be given. All displacement profiles have had their displacements magnified

by 25 and all stress contours are given in units of Pascals.

4.2.1 Residual Stresses

The longitudinal residual stresses after cooldown are within 5% of the results

predicted using the quarter fiber model as presented in Chapter 2. Effective

stresses are shown in Figure 4.5. Even though the first two (vf15) or three (vf37)

fibers are already debonded, the residual stress state is not altered until the matrix

is 'cracked'. The coefficient of thermal expansion of the orthotropic material was

chosen so that notch-induced stress magnitudes were minimal after cooldown. The

vf15 and vf41 CTE values used were 7.3 and 5.62×10^{-6}/C, respectively, and about

29% below those estimated using the expression

$$\alpha_c = \frac{V_f \alpha_f E_f + V_m \alpha_m E_m}{V_f E_f + V_m E_m} \qquad (4.3)$$

4.2.2 Cracking the Matrix

After cooldown, matrix nodes were released to introduce a crack of the

appropriate length. Since the fiber nodes were not released, they 'bridged' the

73

crack. The displacement profiles are shown in Figure 4.4 and, as mentioned

earlier, have had their displacements magnified 25 times. The 582 micron debond

region is clearly visible in Figure 4.4 as misaligned fiber/matrix nodes and ends six

nodes above the crack plane. In both vf15 and vf37, the residual stress induced

crack opening displacements (CODs) increase with distance from the crack tip for

only half of the crack length. The remainder of the crack experiences a decrease

in CODs near the crack mouth. This phenomena of the COD not increasing

monotonically with distance from the crack tip at zero applied load is real and has

been observed experimentally in the current work and in Reference 20. The FEM

results of Reference 37 also show this effect, but it is attributed instead to

fiber/matrix sliding. Apparently, the bridged fibers restrain the matrix and do not

allow a monotonically increasing COD with distance from the crack tip. This

restraining force acts as a side load and imposes an additional bending moment

on the bridged fibers.

Consequently, even though the matrix residual stresses are almost completely

relieved, Figure 4.5 shows that the fibers retain a majority of their longitudinal

residual stresses. Force equilibrium is maintained by the symmetry plane of the

fiber. Since the lateral stiffness of a member increases under load, these retained

fiber residual stresses actually help to reduce the CODs even more. It will be

shown shortly that this retained residual fiber stress also increases the apparent

fiber strength of the bridged fibers. Surprisingly, with no applied stress, the

residual fiber stress ahead of the crack tip is somewhat relieved and does not

approach precracked values for the other two fibers in the discrete fiber/matrix

portion of this model. These reduced compressive residual fiber stresses ahead of

the crack tip lower the effective fiber strength found there and consequently

promote fiber breakage ahead of the crack tip. A considerable crack tip stress

intensity is induced by the cracked matrix and residual stresses alone. Matrix

plasticity is observed just behind the crack tip in the vf37 FEM model and is

induced by residual stresses alone. The notion of a residual stress induced stress

intensity and associated plastic zone size is confirmed by this observation. The

effect of residual stresses on measured plastic zone size and fracture toughness

was addressed in Chapter 3.

4.2.3 Applying Stress

After a 210 MPa stress is applied, the COD profile still actually decreases near

the crack mouth, especially for the vf37 material. The bending of the bridged

fibers is readily seen in the displacement profiles of Figure 4.6. The effect of

residual stresses on the COD profile for vf37 after a 210 MPa applied stress can

be clearly seen in Figure 4.7. When residual stresses are not included, the COD at the notch root is 30% less than that obtained with residual stresses included. However, closer to the crack tip the COD with residual stresses is as much as 300% larger than without residual stresses. The longitudinal fiber stress contours in Figure 4.8 are very different for the two fiber volume fractions. The vf15 bridged fibers show a maximum bridged fiber stress of 2700 MPa at the crack plane. This stress implies a maximum 3300 MPa closure pressure when the 600 MPa compressive residual fiber stress is considered. The 2700 MPa fiber stress equals the in-situ fiber strength [Ref 6, 7] and breaks the bridged fibers nearest the crack mouth. This concurs with the experimental observations.

The vf37 FEM model, with a 582 micron effective debond length, shows a maximum bridged fiber stress of 1200 MPa. This stress implies a maximum fiber clossure pressure of 1650 MPa when the 450 MPa compressive residual fiber stress is considered. That the experimental data show the crack arrest ended and some bridged fibers were broken at this low 210 MPa applied stress level suggests the experimental results were not for a fully bridged crack. There must have been substantial damage to the fibers at the notch root and thereby reducing the fiber volume fraction of bridged fibers. This reduction in bridged fiber volume fraction, as estimated in Chapter 3, results in a fiber breakage stress of 2.7 GPa. Further-

more, the ΔCOD data, also presented in Chapter 2, for vf37 and vf41#1 clearly showed bridged fiber damage as indicated by the larger ΔCODs found near the crack mouth. To break the bridged fibers (fiber stress > 2700 MPa) of a fully bridged crack with this geometry should require an approximate applied stress of about 480 MPa since the bridged fiber stresses scale with the applied stress per Equation 3.8. This applied stress of 480 MPa is very close to the 540 MPa value reported to break the fibers in vf41#3 of Chapter 3 for a crack with a fully bridged crack.

Although not clear in Figure 4.8, the bridged fibers nearest the crack tip experience the largest stress gradient across them. This observation is also reported in Reference 37 and is attributed to the bending moment induced by the applied stress. Reference 37 goes on to conclude that the fiber nearest the crack tip may be the most likely to break upon a further increase in stress. The current work, however, shows that this large stress gradient across the fiber nearest to the crack tip is due exclusively to residual stresses retained in the bridged fibers. Consequently, the larger longitudinal compressive fiber stresses found in the fiber nearest the crack tip has a higher effective strength than the other bridged fibers. Figure 4.9 shows the bridged fiber stress profile across the center of the fiber as a function of position from the notch for a 210 MPa applied stress with and

without residual stresses included for the vf37 material. With residual stresses the overall bridged fiber stress level is lower and the stress gradient higher for the fiber nearest the crack tip. The difference between these two curves is very close to the residual stresses predicted after cracking the matrix but before applying the load, which is also shown in Figure 4.9. It is interesting that the bridged fiber nearest the crack mouth (fiber 1) retains a 450 MPa compressive residual stress on its' notch side after cracking. This value of -450 MPa is essentially the same as that existing in the fiber prior to matrix cracking and occurs where the maximum applied tensile fiber stresses are induced from the applied bending moment. A substantial increase in the effective bridged fiber strength should be expected for the bridged fiber nearest the crack mouth and the crack tip. However, as will be shown shortly, the bridged fiber nearest the crack mouth will always break first.

Some plastic deformation occurs in the matrix even with a fully bridged crack. The effective plastic strain contours of Figure 4.10 show the extent of matrix plasticity more clearly. The volume of plastically deformed material at the crack tip after applying a 210 MPa stress is much greater than that induced by residual stresses alone, but the magnitude of effective plastic strain is the same. Without residual stresses, no matrix plasticity is observed at the crack tip after applying a

210 MPa stress. Consequently, the effective plastic strain data shown in Figure 4.10 is all residual stress related.

The plastic zone size predicted is about half of that actually observed and presented in Chapter 3. Slip bands generally do not end within the grain, but rather at grain boundaries, in a single phase material. Consequently, the FEM predicted extent of matrix plasticity prior to crack arrest is on the order of the grain size because these predicted plastic zone sizes are less than the grain size of the material. The experimentally measured plastic zone size was on the order of the grain size. The ratio of the extent of matrix plasticity parallel to the fibers ($\theta=90$) compared to that along the crack plane ($\theta=0$) is 1.44 and identical to that predicted using the plastic zone size prediction of linear elastic fracture mechanics. Apparently, the high modulus fibers ahead of the crack tip do not significantly alter the development of the plastic zone for the FEM spacing used here. The effect of breaking a bridged fiber on the extent of matrix plasticity at the crack tip, also shown in Figure 4.10, will be discussed next.

4.2.4 Breaking the Bridged Fibers

After inducing residual stresses and applying a 210 MPa stress, the bridged fiber

nearest the notch root was 'broken' by releasing its symmetry nodes. The displacement profiles in Figure 4.11 show the resulting increased CODs. It is apparent that the remaining bridged fiber in vf15 has a large bending stress and that the mouth COD in vf37 is still less than the maximum observed near the center of the crack. The longitudinal stress contours in Figure 4.12 show that the single remaining bridged fiber in the vf15 material experiences a 10% increase in the maximum bridged fiber stress and results in a peak stress of 3.03 GPa, which exceeds the 2.7 GPa in-situ strength of the SCS-6 fiber. Apparently, once the vf15 leading fibers break, the stress redistribution breaks all remaining bridged fibers and greatly reduces fatigue crack growth properties when compared to the unreinforced matrix, as was reported in Chapter 3.

The vf37 material's bridged fibers experience a 15% increase in maximum stress after a bridged fiber is broken. However, the maximum bridged fiber stress of 1.5 GPa is still well below the 2.7 GPa in-situ fiber strength. Consequently, the vf37 material maintains a bridged zone near the crack tip which parades with the propagating fatigue crack, as reported in Chapter 3. If the crack were fully bridged, and a 480 MPa applied stress were required to break some of the bridged fibers, the remaining bridged fibers may have been likely to break as well, just as in the vf15 material. The small bridged fiber stress gradient from one

bridged fiber to the next (Figure 4.14) is probably not large enough to permit breaking only those bridged fibers near the crack mouth while retaining others. Instead, the statistical variation of fiber strength may become dominant. A 30% increase in the magnitude of effective plastic strain is predicted in the matrix at the crack tip after the bridged fiber is broken (Figure 4.10) for the vf37 material.

4.2.5 CODs: Prediction vs Data

It is of interest to compare how the predicted CODs change with effective debond length, fiber volume fraction, and with a broken bridged fiber. CODs are also the best means for validating the FEM model. Figure 4.13 shows the half COD profile as a function of position from the crack tip for the three different effective debond lengths (317, 582, and 1000 microns) in the vf37 material. Also shown is the vf15 half COD profile with a 582 micron debond length with and without a broken bridged fiber. It is worth noting that for the vf37 material the decrease in CODs is not linear with decrease in effective debond length. Instead, a decrease of 43% in effective debond length reduces the CODs by only 22%. An expression for maximum COD as a function of effective debond length for an applied stress of 210 MPa can be given by

$$COD^{max} \sim 0.16\sqrt{L_{eff}} \qquad (4.4)$$

This expression fits the data fairly well but contrasts with the results of Reference 20 which showed a fairly constant ratio of COD to effective debond length for a different specimen geometry and composite matrix material. However, in that work the debond length was not a constant for all bridged fibers. Now, the maximum matrix residual COD value can be subtracted from Equation 4.4, and the resulting expression divided by the effective debond length, to estimate the bridged fiber strain. Multiplying this bridged fiber strain by the fiber modulus and using Equation 4.4 provides

$$\sigma^{fiber}_{bridged} \approx \frac{(COD^{max} - COD^{residual})}{L_{eff}} E_f = \frac{\Delta COD\ E_f}{2\sqrt{L_{eff}}} \qquad (4.5)$$

The predicted COD profile for vf15 with a 582 micron debond length is shown in Figure 4.13 and is greater than any of the vf37 profiles. This larger COD for the lower vf material occurs because of the smaller number of bridged fibers and resulting higher bridged fiber stresses, and hence strains, which cause more displacement for a given effective debond length. In addition, the predicted CODs of the vf15 material are greater than those in the vf37 material because of the lower modulus of the remaining material ahead of the crack tip as modeled in the fiber pressure model presented in Chapter 3. Also shown in Figure 4.13 is the

COD data of a fully bridged vf41 crack and a partially bridged vf15 crack.

Excellent agreement is observed between the vf41 1data and vf37 model with a

317 micron effective debond length. The partially bridged vf15 data agrees with

the vf15 FEM model which has a 582 micron effective debond length and one

broken bridged fiber. Not all COD data agreed with the FEM model so well. The

vf15#1 fully bridged COD data was about half of that predicted and can be

explained by either a much shorter effective debond length than used here or a

much higher local fiber volume fraction.

Another method of comparison is the near tip ΔCOD data because it also can be

directly measured experimentally and is a very good indicator of fatigue crack

growth activity. Figure 4.14 shows the excellent agreement in ΔCODs between the

current FEM models for a 317 micron debond length, the fiber pressure model,

and the experimental data. The vf41 data are used here to compare the vf37

model because the fiber volume fractions are not too different and there are

more vf41 data available.

The maximum total COD profiles of the vf37 FEM model with and without

residual stresses are compared to vf41#1 and vf41#3 experimental data in Figure

4.15. The vf41#1 maximum experimental COD data agrees fairly well with the

vf37 FEM model COD using a 582 micron effective debond length with residual stresses. The vf41#3 COD experimental data, however, is about half that predicted with residual stresses for a 582 micron effective debond length and agrees better with those predicted using a 317 micron effective length. These CODs are similar to those observed when residual stresses are not included with the 582 micron debond length. See Figure 4.15. It is believed that the vf41#1 experimental COD data fits the 582 micron effective debond length FEM model with residual stresses well only because some of the bridged fibers were broken as apparent in the COD profile and low stress to break the bridged fibers. CODs from the FEM model which includes residual stresses, a 317 micron effective debond length, and a broken bridged fiber agrees very well with the vf41#1 data.

Figure 4.16 shows the half COD profiles for the 317 and 582 micron effective debond lengths and include residual stresses at applied stresses of near zero and at 210 MPa. Also shown is vf41#3 data for these same two applied stresses. Since the actual data was obtained with an applied stress of 344 MPa, the measured COD values were reduced by a factor of 210/344 for comparison purposes. At maximum load the 317 micron effective debond length COD data agrees much better than the 582 micron effective debond length. However, at the lower stress values, the data seems to agree better with a 582 micron effective debond length.,

which both show a decreasing COD profile near the crack mouth. That the COD data at low applied stresses is larger than that predicted using a 317 micron effective debond length may be due to matrix plasticity behind the crack tip, which is not included in the FEM model

4.2.6 Bridged Fiber Stresses: Prediction vs Data

For the single edge notch specimen geometry used here, the fiber pressure model crack face closure pressure distribution, c(x), of Equation 3.8 becomes

$$c(x) = 559-98.4x \qquad (4.6)$$

for an applied stress of 210 MPa, where x is the distance from the free surface (ie, specimen edge containing the notch mouth) in millimeters. Dividing by the fiber volume fraction [Ref 24] provides an estimate of the bridged fiber pressures and the vf37 equation becomes

$$\sigma_{37}^{fiber} = 1511-266x \qquad (4.5)$$

and for vf15

$$\sigma_{15}^{fiber} = 3728-653x \qquad (4.6)$$

where the fiber stress is given in MPa. Figure 4.17 shows, on average, the excellent agreement between the fiber pressure model estimation of the bridged

fiber stresses and those of the finite element model with a 582 micron debond length for both the vf15 and vf37 materials. Maximum values and slopes differ, however, with the maximum FEM bridged fiber pressure being about 35% higher than the fiber pressure model. It has been shown elsewhere that prior to crack arrest the fiber/matrix debond length decreases with distance from the crack tip [References 20, 27, and 52]. If this is the case, the fiber pressure would decrease for the fiber near the crack mouth and increase for the others. A much closer accord with the fiber pressure model results. The FEM fiber stress (including residual stresses) is much closer to the fiber pressure model prediction (See Figure 4.9). The fiber pressures were obtained by adding the magnitude of the residual stress retained in the bridged fiber to the fiber stress value. As discussed earlier, this is similar to the bridged fiber stress when residual stresses are not included (Figure 4.9). Attempts to modify the fiber pressure model to increase the overall slopes of the fiber pressure model vs position from the free surface for better agreement with the FEM results were unsuccessful.

The finite element model included a notch because it was believed that a stress concentration was acting on the bridged fibers and resulted in the surprisingly low estimation of fiber break stresses. However, this appears not to be the case. Neglecting the notch effects is valid and the low predicted fiber break stresses are

due to an overestimation of the actual bridged fiber volume fraction (ie, notch fiber damage).

Figure 4.17 shows that a 20% decrease in bridged fiber stress results from a 44% increase in debond length. Apparently, materials with significantly different fiber/matrix interface shear strengths than those used here, which result in different debond lengths, will require an alternate crack closure pressure distribution in the fiber pressure model. Assuming the 582 micron debond length to be the best fit to the fiber pressure model data shown in Figure 4.17, an empirical new crack face closure distribution which includes the influence of effective debond length can be given as

$$c(x) = \sigma^{\infty}(\frac{582}{L_{\it eff}})^{0.25}(\frac{w}{w-a_0} + \frac{6wa_0[0.5(w-a_0)-(x-a_0)]}{(w-a_0)^3}) \qquad (4.9)$$

where this expression is identical to that in Equation 3.8 except for the $L_{\rm eff}$ term. For a longer (shorter) effective debond length than 582 microns, Equation 4.9 predicts lower (higher) closure pressures and lower (higher) bridged fiber stresses accordingly.

Figure 4.18 shows how the bridged fiber stress increases with applied stress for the vf37 FEM model with a 317 micron effective debond length. The largest

increases in bridged fiber stress with applied stress occur at the fiber nearest the crack mouth. The rate of change of bridged fiber stress with change in applied stress is constant for a given location regardless of the applied stress level. Figure 4.19 shows the variation in this rate of change with position from the free surface. The bridged fiber nearest the crack mouth will always be the first one to break, neglecting the statistical variation in fiber strengths.

-Chapter 5-

SUMMARY

Notched unidirectional SCS-6/Ti-15-3 composites of three different fiber volume fractions (vf=0.15, 0.37, and 0.41) were investigated at room temperature microstructural, fatigue crack initiation, fatigue crack growth, and fracture toughness behavior. The experimental results were successfully modeled using analytical and finite element methods. These efforts have provided the following conclusions:

MATERIAL PROPERTIES AND MATRIX CRACK INITIATION

1) Maximum residual stress values generally increase with fiber volume fraction. Residual stress induced matrix plasticity only occurs in the vf41 material, because the minimum fiber spacing approaches 25 microns.

2) Composite fatigue crack initiation is matrix controlled with fiber induced perturbations.

3) Matrix fatigue crack initiation occurs when the applied and residual stresses impose a net matrix stress which approaches the matrix endurance limit stress.

4) The composite crack initiation stress can be given by:

$$\sigma_{composite}^{initiation} = \frac{1}{K_t} [1 + v_f(\frac{E_f}{E_m} - 1)] [\sigma_{titanium}^{endurance} - \sigma_{titanium}^{residual}]$$

5) The expression for composite crack initiation stress can be approximated by a second order polynomial in vf if the longitudinal matrix residual stress is assumed linear in vf. The resulting second order polynomial has a maximum at vf=0.15 for this fiber/matrix combination. The current data support this finding.

6) Applications of this material which are crack intolerant should consider the lower fiber volume fraction material. Designers may want to consider using lower fiber volume fraction materials around notches and holes in aerospace structures. However, applications which reduce the residual stress state (ie, engineered interlayers or elevated temperatures) minimize this effect.

FATIGUE CRACK GROWTH AND FRACTURE TOUGHNESS

1) Only one fiber bridged crack arrest is possible in all fiber volume fractions and occurs at an applied ΔK of about 14 MPa m$^{1/2}$. Consequently, the crack face closure pressures must be similar and hence the vf15 fibers experience a higher stress state at crack arrest.

2) Crack growth recommenced when the incrementally increased stress level broke the bridged fibers nearest the crack mouth. The applied stress level neceassary for breaking the bridged fibers of a fully bridged crack in the vf15 material was 215 MPa and 540 MPa in the vf41 material.

3) The large difference in the estimated fiber breakage stresses of 3.0, 1.3, and 1.2 GPa for vf15, vf37, and vf41#1, respectively, is attributed, in part, to an increase in notch damaged fibers for vf37 and vf41#1 and higher retained compressive residual fiber stresses in the cracked vf15 material. A fully bridged vf41 crack (vf41#3) had an estimated bridged fiber break stress of 2.7 GPa.

4) After crack arrest, the vf37 and vf41 material exhibited a much lower growth rate exponent and higher composite toughness than the unreinforced matrix

because of the bridged zone which parades with the propagating crack tip. The vf15 material demonstrated much higher growth rate exponents and lower toughness than the unreinforced matrix because the redistribution of stresses broke all bridged fibers and resulted in an unbridged crack.

5) Unbridged cracks in unidirectional composites exhibit improved fatigue crack growth properties when compared to the unreinforced matrix because the high modulus fibers reduce the stress intensity imposed on the matrix. The magnitude of this improvement is better approximated by an energy based formulation than when scaled linearly with modulus. The toughness behavior is significantly degraded because of the matrix residual stresses.

6) The fiber pressure model accurately predicts both pre and post arrest crack growth behavior for all fiber volume fractions. The predicted effective matrix stress intensity range is consistent with that measured indirectly using plastic zone size measurements and the expression

$$\Delta K^m_{applied} = (\sigma^m_{YS} - \sigma^m_{residual})\sqrt{2\pi r_p}$$

7) A new fiber pressure model was presented which accounts for specimen and grip geometry.

8) The development of matrix plasticity, observable by a special heat treatment, allows direct measurement of matrix residual stresses. Furthermore, all fiber/matrix debonding ahead of the crack tip was associated with and likely caused by matrix plasticity.

9) It is predicted that the vf15 material is the minimum fiber volume fraction which can demonstrate fiber bridging induced crack arrest. Lower fiber volume fractions result in broken fibers before bridging can become fully active.

FINITE ELEMENT MODELING OF BRIDGED FIBER STRESSES

1) An effective debond length can be used with multi-point constraints to accurately simulate behavior in these unidirectional metal matrix composites.

2) Even though residual stresses are essentially relieved in the cracked matrix, the bridged fibers retain half of their longitudinal residual stresses.

3) This retained compressive residual fiber stress provides a higher effective strength in the lower fiber volume fraction material, as observed experimentally.

4) After the first bridged fibers break, the stress redistribution on the remaining bridged fibers break those in the vf15 material but not those of the vf37 material, as observed experimentally.

5) For a constant applied stress, bridged fiber stresses increase with decreasing in fiber volume fraction and debond length. Excellent correlation of the fiber stress distribution was obtained between these FEM models and the fiber pressure model.

6) Predicted CODs increase with decreasing fiber volume fraction and increasing debond length.

7) The predicted CODs agree well with those measured when a 317 micron effective fiber/matrix debond length is used.

-Chapter 6-

CONCLUDING REMARKS

6.1 LIFE PREDICTION

The experimental data and models presented in the preceding chapters are portions of what would be necessary for predicting the life of the SCS-6/Ti-15-3 composite for a given application. Reliable life prediction is a requirement before these materials can obtain widespread use in future aerospace structures. However, before life prediction can be attempted, a complete understanding of the damage mechanisms, and their effect on life, must be available. Dominant fatigue mechanisms in composites have been previously identified using a "fatigue life diagram". Even though this type of diagram was originally developed for polymer matrix composites[40], it has also been used successfully for metal-matrix composites manufactured with SiC fibers and matrices having a failure strain on the order of 15%[41]. The as-received Ti-15-3 matrix material has this type of ductility at room temperature, and some of the more brittle matrices do at

elevated temperatures. A fatigue life diagram, as shown in Figure 6.1, has three distinct regions on a stress or strain vs life plot.

Region I is observed at the highest applied stresses or strain levels and has the shortest life. In this region life is relatively independent of stress or strain and fiber breakage is the dominant failure mechanism. Region II shows increasing life with decreasing applied stress or strain and is generally governed by matrix cracking. Region III behavior is observed at the lowest applied stresses or strains and, like Region I, life is relatively independent of the applied stress or strain level. Here, the endurance limit of the matrix controls the dominant mechanism. Each of these three regions have different damage mechanisms, exhibit different behavior, and require different models. As discussed here, these three regions are almost identical to those presented in Figure 3.13 for the vf37 materials subjected to different stress levels. The only difference is that Region III initiation is governed by matrix endurance properties but life is governed by the strength of the bridged fibers which arrest the crack. Consequently, the experimental data and models presented in previous chapters are all Region III and lower Region II results as defined on the fatigue life diagram.

There are couple of mechanistic based models under development which attempt

life prediction of these materials. An impressive general purpose analysis program, called MMCLIFE[42], can accommodate all three different dominant mechanisms with and without notches. Rather than relying on rigorous solutions and extensive CPU, this package applies very clever approximations to provide reasonably accurate solutions. The general approach is to start with lamination theory and superimpose residual stresses to predict ply effective stresses. These effective stresses are then used in a Miner's rule type (total life sums to 1) method for estimating stiffness reductions to the fiber and matrix of a ply when certain stress levels are exceeded. Once a crack initiates, a weight function approach is used to estimate stress intensity and is then integrated in a Paris law fashion to estimate life.

Another effort at life prediction applies specifically to Region II and Region III behavior in notched composites. This effort defines crack initiation using an effective strain parameter, $\Delta\epsilon_{eff}$, given by[43]:

$$\Delta\epsilon_{eff} = \sqrt{(K_t\epsilon_{max} + \frac{\sigma_m^r}{E_m})\frac{\Delta\epsilon K_t}{2}} \qquad (6.1)$$

where

K_t = notch stress concentration factor

$\Delta\epsilon$ = applied strain range

σ_m^r = matrix longitudinal residual stress

ϵ_{max} = maximum applied strain

Once cracks initiate, micromechanics (via ACK) is combined with a shear lag model to provide a Paris law which can be integrated to estimate life[44].

While these methods seem to correlate the data very well, it is not clear how effective they are at predicting for slightly different loading conditions. Neither model uses the higher residual stress values which result from fiber neighbor interactions as discussed in Chapter 2. Neither model considers surface roughness effects, which have been shown to increase cycles to failure over an order of magnitude for polished SCS-6/Ti-15-3 specimens compared to as-machined[45]. Neither model considers how the number of fibers damaged during machining of the notch or variation in notch fiber linear fraction influences the stress level at which crack arrest ends. The perturbed residual stress state in the bridged fibers is not considered nor are the fiber/matrix debond lengths and their effect on bridged fiber stress. Gripping effects are not included in their stress intensity solutions, which have been shown in Appendix 2.1 to be critical. Both models scale the applied composite stress intensity linearly with the matrix and composite moduli to estimate the effective matrix stress intensity, an approach with very

different results from the energetically consistent method used here. The initiation criteria using the effective stress parameter of Equation 6.1 did not provide a consistent estimate of crack initiation when used with the initiation data of Chapter 2. Neither of the models have been verified for use with different fiber volume fractions, although the data and models presented here should prove very valuable for fine tuning these life prediction methods.

Rather than predicting life, the current results will be used to attempt an explanation of the recently published room temperature low cycle fatigue stress-life curve for the same fiber volume fractions (0.15, 0.37, and 0.41). The stress-life curve for each fiber volume fraction and unreinforced matrix is shown in Figure 6.2[46]. These tests were run using an R-ratio of 0.1 in unnotched specimens. As can be seen, the fatigue life diagram of Figure 6.1, with three regions, applies for the SCS-6/Ti-15-3 composite system. The higher fiber volume fraction materials have almost two orders of magnitude increase in life over the vf15 material, and even more over the unreinforced matrix, for a given applied stress range. The slope decreases uniformly with increasing fiber volume fraction. Although not explicitly part of the data set in Figure 6.2, an approximate 450 MPa endurance limit stress of the vf41 material must be two or three times that of the vf15 material. This vf41 endurance limit stress of 450 MPa agrees very well with the

500 MPa value given in Reference 45 for a 0.39 fiber volume fraction material at the same 0.1 R-ratio. However, an approximate matrix endurance limit stress of 150 MPa is well below the value previously established for Ti-15-3 as discussed in Chapter 2.

6.2 OPTIMUM FIBER VOLUME FRACTION

Recall from Chapter 2 that the composite crack initiation stress was experimentally and analytically shown to be a maximum for the vf15 material and seems to contradict the results of Figure 6.2. However, after crack arrest, breaking the bridged fibers in the vf41 material required a stress increase of almost three times that of the vf15 material for a fully bridged crack (540 MPa vs 200 MPa). As discussed in Chapter 2, the lower composite initiation stress of the vf41 material was due to increased matrix residual stresses, which do not affect fatigue crack growth. Consequently, the higher vf41 endurance limit stress of Figure 6.2 must be entirely due to the additional stress necessary to break the bridged fibers and recommence crack growth, as discussed in Chapter 3.

Because the LCF data for vf37 and vf41 are similar (Figure 6.2), the vf41 plate quality was considered questionable[47]. X-rays of the plates revealed that the vf41

plate had a high percentage of broken Mo-weave and therefore its integrity was questioned. It was assumed that the Mo-weave damaged a considerable number of the fibers, but subsequent metallography and strengths of fibers etched out of all three plates were similar[48]. Because extended periods of fatigue crack growth were noted on the fracture surfaces of the LCF specimens, an alternate explanation may account for why the behavior of the vf41 plate was so similar to the vf37 on the stress-life curve of Figure 6.2: fracture mechanics.

In Chapter 3, an energy based analysis predicted a maximum stress intensity ratio, K^c/K^m, of 1.2 at a 0.36 fiber volume fraction (Equation 3.14) with a reduction for higher fiber volume fractions (Figure 3.14). Even though this decrease in stress intensity ratio is small, it may be a substantial percentage of the tensile property increase expected for additional fiber volume fraction. Consequently, it would seem that the vf37 and vf41 composite provides similar life in the SCS-6/Ti-15-3 system because of a fracture mechanics condition. As Figure 3.14 shows, any further increase in fiber volume fraction beyond 0.36 should actually reduce fatigue crack growth and fracture properties because the matrix experiences an increasing amount of the crack driving force. Additionally, an increase in fiber volume fraction beyond that needed to achieve the desired longitudinal properties may further degrade the transverse properties. In fact, preliminary transverse

tensile results suggest that the vf41 transverse strength is half that of both the vf15 and the vf37[49]. Therefore, when considering room temperature fatigue applications at stresses which allow fatigue crack growth, the optimum fiber volume fraction for this composite system is ≈ 0.35.

6.3 FUTURE WORK

Some possible future projects related to this work have been identified:

1) Recently procured vf37 material manufactured using 32 plies would resolve the question about thickness effects on crack growth and toughness (ie, vf15) when compared to the thinner 8 ply plates used here.

2) It would also allow study of how fully reversed loading affects crack growth in the vf37 material.

3) Obtaining fine grained unreinforced Ti-15-3 would allow a thorough study of an experimental plastic zone size and shape with associated stress intensity and how it compares to fracture mechanics predictions. It is expected that the fatigue plastic zone will have a different appearance than the monotonic plastic zone.

4) Development of life prediction models would be very useful in screening applications for these types of materials. Besides those discussed above, other life prediction models have recently appeared[50,51,52].

5) Discrete fiber/matrix finite element models with longer crack lengths can be used to study fiber bridging effects on toughness. This study should be combined with an experimental program which defines the fiber bridging effect on toughness and the role of stress levels.

6) Effect of elevated temperatures on the current data and models would also be useful.

REFERENCES

1. Collins, E., THE PHYSICAL METALLURGY OF TITANIUM ALLOYS, American Society for Metals, 1984

2. Briggs, R., Taggart, R., Polonis, D., "Crack Growth Study in the Ti-15-3 beta Titanium Alloy", Microstructure, Fracture Toughness, and Fatigue Crack Growth Rates in Titanium Alloys, A. Chakrabarti and S. Chernault, Editors, Proceedings TSM-AIME, February, 1987.

3. Lerch, B., Hull, D., Leonhardt, T., "Microstructure of a SiC/Ti-15-3 Composite", Composites, V21, N3, May 1990, pp.216-224

4. Lerch, B., Gabb, T., and MacKay, R., "Heat Treatment Tensile Study of the Sic/Ti-15-3 Composite System", NASA TP 2970, January 1990

5. Covey, S., Challenger, K., Stouffer, D., and Jayaraman, N., "A New Servohydraulic Fatigue Stage for Use in a Scanning Electron Microscope", Experimental Techniques, November 1992

6. Yang, J., Jeng, S., and Yang, C., "Fracture Mechanisms of Fiber Reinforced Titanium Alloy Composites Part 1: Interfacial Behavior", Materials Science and Engineering, A138/139, 1991

7. Gayda, J., NASA Lewis Research Center, Private Communication, December 1992

8. Eldridge, J., "Desktop Fiber Push-out Apparatus", NASA Technical Memorandum 105341, December 1991

9. Arnold, S. and Wilt, T., "Influence of Engineered Interfaces on Residual Stresses and Mechanical Response in Metal Matrix Composites", NASA Technical Memorandum 105438, March 1992

10. Rangaswamy, P. and Jayaraman, N., "Finite Element Modeling of Residual Stresses in Metal Matrix Composites", Accepted for publication in The Journal of Composites and Technology Research, March 1993

11. Lococo, M., Sensmeier, M., and Wright, K., "Effects of Thermal Stresses on Mechanical Behavior of SCS-6/Ti-24Al-11Nb", HiTemp Review, October 1992, NASA CP 10104, pp.29-1 to 29-12

12.   PATRAN, PDA Engineering, Costa Mesa, CA

13.   MARC, MARC Analysis Research Corporation, Palo Alto, CA

14.   Bigelow, C., "The Effects of Uneven Fiber Spacing on the Thermal Residual Stresses in Unidirectional SCS-6/Ti-15-3 Laminates", NASA Technical Memorandum 104225, March 1992

15.   Bakuckas, J., Johnson, W., and Bigelow, C., "Fatigue Damage in Cross-Ply titanium Metal Matrix Composites Containing Center Holes", NASA Technical Memorandum 104197, January 1992

16.   Newaz, G. and Majumdar, B., "Crack Initiation Around Holes in Unidirectional MMC Under Fatigue Loading", Technical Note, Engineering Fracture Mechanics, V42, N4, 1992, pp.699-711

17.   Rosenberg, H., "Ti-15-3 Property Data", Proceedings of a Symposium Sponsored by The Titanium committee of AIME, TMS Annual Meeting, Atlanta, Georgia, March, 1983

18.   Ritter, A. and Dupree, P., "Effect of Coating Thickness on the Strength of SCS-6 SiC Fibers", Scripta Mettallurgica et Materialia, V27, pp.827-831, 1992

19.   Jeng, S., Alassoeur, P., and Yeng, J., "Fracture Mechanisms of Fiber-Reinforced Titanium Alloy Matrix Composites V: Fatigue Crack Propagation", Materials Science and Engineering, A154, pp.11-19, 1992

20.   Davidson, D., "The Micromechanics of Fatigue Crack Growth at 25 C in Ti-6Al-4V Reinforced with SCS-6 Fibers", Metallurgical Transactions A, Volume 23A, pp.865-879, March 1992

21.   Walls, D. and Zok, F., "The Effects of Notches on the Fatigue Behavior of a Ti/SiC Composite", Advanced Metal Matrix Composites for Elevated Temperatures Conference Proceedings, Cincinnati, OH USA, pp.101-107, October 1991

22.   Marshall, D., Cox, B., and Evans, A., "The Mechanics of Matrix Cracking in Brittle-Matrix Fiber Composites", Acta Metallurgica Volume 33, No 11, pp.2013-2021, 1985

23. Ghosn, L., Kantzos, P., and Telesman, J., "Modeling of Crack Bridging in a Unidirectional Metal Matrix Composite", International Journal of Fracture, Volume 54, pp.345-357, 1992

24. McCartney, L., "Mechanics of Matrix Cracking in Brittle-Matrix Fiber-Reinforced Composites", Proceedings of the Royal Society of London, A409, pp.329-350, 1987

25. Tada,H. and Paris, P., STRESS INTENSITY HANDBOOK, pp.2.10-2.11, October 1985

26. Walls, D., Bao, G., and Zok, F., "Fatigue Crack Growth in a Ti/SiC Composite", Engineering Foundation Conference on Mechanical Fatigue in Advanced Materials, Santa Barbara, CA, June 1991

27. Kantzos, P., "Fatigue Crack Growth and Crack Bridging in Ti-Based Metal Matrix Composites", MS Thesis, Penn State University, December 1991

28. Lerch, B., "Matrix Plasticity in SiC/Ti-15-3 Composite", NASA Technical Memorandum 103760, July 1991

29. Dieter, G., MECHANICAL METALLURGY, McGraw Hill, p.360, 1986

30. Bania, P., Lenning, G., and Hall, J., "Development and Properties of Ti-15V-3Cr-3Sn-3Al (Ti-15-3)", Beta Titanium Alloys in the 80's, Boyer, R. and Rosenberg, H., Editors, Proceedings of AIME Titanium Committee of TMS Annual Meeting, Atlanta, Georgia, March 8, 1983

31. Saxena, A. and Antolovich, S., "Low Cycle Fatigue, Fatigue Crack Propagation, and Substructures in a Series of Polycrystalline Cu-Al Alloys", Metallurgical Transactions A, Volume 6A, September 1975, pp. 1975-1809

32. Lankford, J. and Hudak, S., "Relevance of the Small Crack Problem to Lifetime Prediction in Gas Turbines", International Journal of Fatigue, pp. 87-92, April 1987

33. Broek, D., ELEMENTARY ENGINEERING FRACTURE MECHANICS, Martinus Nijhoff Press, New York, NY, 1982, Chapter 4.

34. Saigal, A., Kupperman, D., and Majumdar, S, "Residual Strains in Titanium Matrix High-Temperature Composites", Materials Science and Engineering, A150, pp.59-66, 1992

35. Lerch, B., Melis, M., and Tong, M., "Experimental and Analytical Analysis of Stress-Strain Behavior in a $[90/0]_{2s}$ SiC/Ti-15-3 Laminate", NASA Technical Memorandum 104470, August 1991

36. Kennedy, T. and Wang, M., "Micromechanical Analysis of Short Cracks in Fiber-Reinforced Ceramics", Journal of the American Ceramic Society, 71 (12), pp.c-490-c-491, 1988

37. Morris, W., Dudlhah, M., James, M., Mitchell, M, and Schroeder, S., "Micromechanics of Fatigue Crack Growth in Ti-Aluminide Composites", WL-TR-91-4020, P. Smith, S. Balsome, and T. Nicholas, Eds, pp.511-521, February 1991

38. McClung, R. and Sehitoglu, H., "On the Finite Element Analysis of Fatigue Crack Closure - I: Basic Modeling Issues", Engineering Fracture Mechanics, Volume 33, Number 2, pp.237-252, 1989

39. Henshall, R. and Shaw, K., "Crack Tip Elements are Unnecessary", International Journal of Numerical Methods in Engineering, Volume 9, pp.495-507, 1975

40. Talreja, R., FATIGUE OF COMPOSITES MATERIALS, Technomic Publishing Co., Lancaster, Pa, 1987

41. Bartolotta, P., "Fatigue Behavior and Life Prediction of a Sic/Ti-24Al-11Nb Composite Under Isothermal Conditions", NASA Technical Memorandum 105168, August 1991

42. Harmon, D. and Finefield, M., "Thermomechanical Load History Effects in Metal Matrix Composites: Third Interim Report", McDonnell Douglas Aerospace Report MDC 93B0030, February, 1993

43. Hillberry, B. and Johnson, W. S., "Prediction of Matrix Fatigue Crack Initiation in Notched SCS-6/Ti-15-3 Metal Matrix Composites", Journal of Composites Technology & Research, JCTRER, Vol.14, No.4, Winter 1992, pp.221-224

44.   Bakuckas, J. and Johnson, W. S., "Damage Initiation and Life Prediction Methodologies for Titanium Matrix Composites", Presented at the GWP 85B: Material Characterization of Titanium Matrix Composites section of the NIC Steering Committee Meeting, Pratt & Whitney, West Palm Beach, FL, January, 1993

45.   Jeng, S., Alassoeur, P., Yang, J., and Aksoy, S., "Fracture Mechanisms of Fiber-Reinforced Titanium Alloy Matrix Composites Part IV: Low Cycle Fatigue", Materials Science and Engineering, A148, pp.67-77, 1991

46.   Majumdar, B., "Isothermal Fatigue Mechanisms in Ti-Based Metal Matrix Composites", Final Report of NASA Contract NAS3-26494 to Battelle, March 1993

47.   Gayda, J. and Gabb, T., "The Effect of Fiber Content on the Fatigue Life of SCS-6/Ti-15-3 Composite", Presented at the Seventh NASA Hi-Temp Conference, Cleveland, OH, October, 1992

48.   Gayda, J., Private Communication, NASA Lewis, November, 1992

49.   Lerch, B., Private Communication, NASA Lewis, April 1993

50.   Jira, J. and Larsen, J., "Fatigue of Unidirectional SCS-6/Ti-24Al-11Nb Composite Containing a Circular Hole (Part I)", Submitted to Metallurgical Transactions, February 1993

51.   Bakuckas, J. and Johnson, W.S., "Application of Fiber Bridging Models to Fatigue Crack Growth in Unidirectional Titanium Matrix Composites", NASA Technical Memorandum 107588, July 1992

52.   John, R., Jira, J., Larsen, J., and Ashbough, N., "Fatigue Crack Growth in Unidirectional SCS-6/Ti-24Al-11Nb Composite Containing a Circular Hole (Part II)", Submitted to Metallurgical Transactions, February 1993

TABLES

Table 1.1: Typical Room Temperature Constitutive Properties

	Ti-15-3 Matrix	SCS-6 Fiber
Modulus (GPa)	90	400
Strength (MPa)	800	3500
K_c (MPa m$^{1/2}$)	100	4
CTE (x10^{-6}/C)	8	3

Table 2.1: Material System Data For SCS-6/Ti-15-3

Fiber Volume Fraction	15	37	41
Grain Size (Microns)	350x300x200	200x110x150	200x100x150
Hardness[1] (Hv)	248	260[a]	247
Interfacial Strength[2] (MPa)	113 (24)	128 (37)	151 (35)
Plate Thickness (mm)	2.90	1.68	1.52
Modulus (GPa)	124[b]	186[a]	200[b]
Tensile Strength (GPa)	1.14[b]	1.38[a]	1.45[b]

109

[a]   Ref [4]

[b]   Lerch, B., Private Communication, March 1992

[1]   Average of at least ten, 200g Vickers measurements

[2]   Average of at least thirty-five fiber pushout tests (values in parenthesis are one

standard deviation)

Table 2.2: Constitutive Properties used for FEM Modeling

Matrix (elastic perfectly-plastic)

Temperature	E	CTE	Yield Stress	Poisson's Ratio
(C)	(GPa)	$(10^{-6}/C)$	(MPa)	
25	88.3	8.1	710	0.34
300	80.7	9.3	582	0.34
550	74.5	10.0	450	0.34
700	68.3	10.5	207	0.34

Fiber (elastic only)

Temperature (C)	E (GPa)	CTE (10^{-6}/C)	Poisson's Ratio
25	393	2.0	0.22
300	380	2.5	0.22
550	373	4.5	0.22
700	368	5.0	0.22

Table 2.3: Finite Element Prediction of Maximum Residual Stresses

(location may vary)

Matrix Stress (MPa)	Vf15	Vf37	Vf41
Radial	-250	-290	-390
Tangential	320	445	425
Longitudinal	210	380	430
Effective	600	645	710
Plasticity?	No	No	Yes
Fiber Stress (MPa)			
Fiber Longitudinal	-990	-490	-444

Table 2.4: Maximum Notch Stress, Associated Cycles, and Damage Status

(clearly shows stress history)

Notch Stress (MPa)	Cycle Number (kcycles)	Damage Status
	VF15#1	
280	0 to 30	fiber cracks
330	30 to 68	fiber cracks
422	68 to 116	fiber cracks
495	116 to 171	small matrix crack
561	171 to 238	small matrix crack
684	238 to 410	many matrix cracks
	VF15#2	
647	0 to 194	small matrix crack
712	194 to 234	many matrix cracks

VF37

| 561 | 0 to 0.37 | small matrix crack |
| 561 | 0.37 to 200 | many matrix cracks |

VF41#1

| 351 | 0 to 45 | fiber cracks |
| 511 | 45 to 50 | many matrix cracks |

VF41#3

| 407 | 0 to 92 | small matrix crack |
| 463 | 92 to 163 | many matrix cracks |

Table 2.5: Composite Crack Initiation Stresses and Stress Concentration Factors

Specimen	Notch Depth (microns)	Width (microns)	K_t	Initiation Stress* (MPa)	Notch Stress (MPa)
vf15#1	825	5120	5.1	134	684
vf15#2	760	5120	4.9	144	712
vf37	1350	6800	6.4	87.7	561
vf41#1	925	5120	5.3	96.4	511
vf41#3	980	5120	5.4	85.7	463

* The composite crack initiation stress is defined as that applied stress which first initiates multiple independent matrix cracks in the notch of the composite. These cracks are on the order of 50 microns long.

Table 3.1: Values at Crack Arrest

Fiber Volume Fraction	Vf15		Vf37	Vf41	
	#1	#2		#1	#3
Average Crack Length (microns)	1210	1220	1832	1325	1355
Specimen Width (microns)	5120	5120	6800	5120	5120
Applied Stress Range (MPa)	121	130	118	174	155
Applied ΔK (MPa m$^{1/2}$)	11	12	14	17	16
Cumulative Cycles (thousands)	633	744	638	560	900

Table 3.2: Measured da/dN vs Applied ΔK Prior to Crack Arrest

(m/c=meters per cycle)

Vf15#1		Vf37		Vf41#1	
da/dN	ΔK	da/dN	ΔK	da/dN	ΔK
$(10^{-9}$ m/c)	(MPa m$^{1/2}$)	$(10^{-9}$ m/c)	(MPa m$^{1/2}$)	$(10^{-9}$ m/c)	(MPa m$^{1/2}$)
3.4	10.2	3.6	12.5	2.5	12.1
1.2	10.5	1.51	13.5	0.89	14.9
0.64	10.8	1.05	13.7	1.0	15.6
0.2	10.9	0.61	14.0	0.57	17.3
0.1	10.9	0.1	14.0	0.1	17.3

Table 3.3: Values Which Broke the Bridged Fibers

Composite Vf	a (microns)	a/w	Applied σ (MPa)	ΔK (MPa m$^{1/2}$)	Fiber Break Stress[a], GPa
15#1	1210	0.24	201	16	3.0
15#2	1220	0.24	203	16	3.0
37	1832	0.27	219	23	1.3
41#1	1325	0.26	225	20	1.2
41#3	1355	0.27	230	21[b]	2.7

[a]Fully bridged cracks have the higher predicted fiber break stresses which are roughly equal to the in-situ fiber strength. The lower predicted fiber break stresses for partially bridged cracks implies damaged fibers at the notch root.

[b]Applied ΔK of 21 MPa m$^{1/2}$ induced additional crack growth but obtaining a large increase in CODs required a 541 MPa stress (ΔK=50 MPa m$^{1/2}$), which was used to predict the 2.7 GPa fiber break stress.

Table 3.4: Values at Fracture

Composite Vf	a (microns)	a/w	Applied σ (MPa)	$K_c^@$ (MPa m$^{1/2}$)	Net σ/σ_{UTS}
15#1	2200	0.43	201	38 (27)	0.31
37	5050	0.74	219	223 (76)	0.62
41#1	4310	0.84	225	450 (80)	1.0
41#2	3794	0.74	343	94	0.91

$^@$All toughness values, except vf41#2, were computed using the Tada pinned solution. Vf41#2, and values in parenthesis, were computed using the rotationally constrained solution for L/W=4.0. See Appendix 2.

Table 3.5: Values Used to Estimate Unbridged Composite Toughness

	Vf15	Vf37	Vf41
Composite Modulus (ROM, GPa)	136.5	204.7	217.1
Average Effective Residual Stress (FEM, MPa)	490	580	600
λ (Ratio of Residual to Fracture Stress)	0.61	0.73	0.75
Predicted Unbridged Toughness (MPa m$^{1/2}$)	44	32	30
Measured Unbridged Toughness (MPa m$^{1/2}$)	38	*	*

* Bridging was active at specimen failure for the vf37 and vf41 materials.

Other unreinforced matrix properties used for modeling include: fracture stress = 800 MPa[1], modulus = 90 MPa[1], and toughness = 100 MPa m$^{1/2}$ [2].

[1]Reference 4 in Appendix 3

[2]Reference 17

Table 4.1: Othotropic Material Properties

Orthotropic, Vf37

Direction	Elastic Modulus		Shear Modulus		CTE[a]	Poisson's
i,j =	E_{ij}	(GPa)	G_{ij}	(GPa)	(10^{-6}/C)	Ratio
11	222		55		5.62	0.30
12	122		45		5.62	0.20
23	122		45		5.62	0.20

Orthotropic, Vf15

Direction	Elastic Modulus		Shear Modulus		CTE[a]	Poisson's
i,j =	E_{ij}	(GPa)	G_{ij}	(GPa)	(10^{-6}/C)	Ratio
11	122		50		7.3	0.33
12	100		40		7.3	0.25
23	100		40		7.3	0.25

[a]Orthotropic CTE chosen so that notch stress after cooldown is minimal.

Table A1: Statistics of Fiber Linear Fraction Within Rows

	Vf15	Vf41
Mean	0.152	0.427
Std Dev	0.0416	0.0818
Std Err	0.0044	0.0087
Number	88	89
Maximum	0.243	0.589
Minimum	0.051	0.216

APPENDIX 1

PERIODICITY OF NOTCH FIBER LINEAR FRACTION

Applications of these materials to aerospace structures require use of many notches and bolt holes. However, the local behavior in the high stress region of each notch is controlled by the local fiber volume fraction and may be quite different than the average fiber volume fraction. In what follows, an attempt was made to address this issue by statistically analyzing the variation in notch fiber fraction with position. In the process, the periodic nature of the fiber spacing within rows becomes apparent.

For composites, in general, the determination of reinforcement volume fraction is a three dimensional problem which requires use of certain position and shape assumptions for calculation from a (two dimensional) photograph. Continuous fiber composites allow absolute determination of fiber volume fraction from a photograph measured area fraction because there is no change in the third

122

dimension and hence is a two dimensional problem. Similarly, the notch fiber

linear fraction is a one dimensional look at a two dimensional problem and

depends on fiber spacing between rows and distribution within rows. Since the

fiber spacing between rows is easy to determine and fairly constant, the

distribution within rows is what needs to be addressed.

To determine the distribution profile of the fiber linear fraction at the notch root

in foil-fiber-foil composites, a study was defined which included measuring

intercepted fiber length by lines running through the thickness (ie, perpendicular

to the ply direction) on a collage of low magnification photographs looking similar

to that shown in Figure 1.1 of the text. The eighty-eight lines had a spacing of 48

and 23 microns for the vf15 and vf41, respectively (~7.5 lines per average unit

cell). The vf37 material was not analyzed. The notch fiber linear fraction was

defined as the total intersected fiber length divided by the plate thickness.

Periodicity is apparent in the notch fiber linear fraction vs position graphs shown

in Figure A1.1 with the statistics given in Table A1. Note that in both cases the

variational amplitude (ie, peak-to-peak or maximum minus minimum) is on the

same order as the mean. This implies that the uncertainty, or variation, in fiber

linear fraction increases with the fiber volume fraction. A transverse tension test

will almost certainly fail in the region of largest fiber linear fraction. For example,

if the fibers are considered as holes in a transverse tension test, the maximum net section stress will be almost three times the minimum (ie, 0.589/0.216 from Table A1).

Periodicity can best be ascertained using a Fourier transform which represents the total distribution as a sum of periodic functions. These periodic functions can then be analyzed for frequency content by computing the energy at each frequency, or power spectrum. For a random distribution the Fourier transform will have a flat power spectrum while a single frequency distribution will have an extremely large power spectrum at that frequency. Of the eighty-eight data points, the first sixty-four were used to compute the fast Fourier transform (FFT) for vf15 and vf41. The power spectrum was then plotted against the period, rather than frequency, because of its physical significance. The results are shown in Figure A1.2.

For both the vf15 and the vf41 fiber volume fractions the repeated rectangular arrays (ie, unit cell) dimensions were computed using the period of the power spectrum and resulted in the geometry shown in Figure 2.2 of the text. While vf41 has one sharp peak, vf15 shows a maximum peak at twice the average spacing. This implies that whatever randomness occurs from fiber-to-fiber, it is repeated with good certainty over two fibers. As mentioned earlier, the notch fiber linear

fractions of the samples tested for this work were all very close to the overall composite fiber volume fraction. The largest deviation of notch fiber linear fraction from the compoiste fiber voulme fraction was in vf37 which had a notch fiber linear fraction of 0.42 and did not seem to influence the crack initiation results. However, it is likely that if tests were performed on samples with notch fiber linear fractions of extreme values initiation properties would be different. Finally, the periodicity of fiber spacing within rows implies that the quarter fiber (or unit cell) finite element models may be more representative of the actual material than the hexagonal array.

APPENDIX 2

WEIGHT FUNCTIONS, STRESS INTENSITY SOLUTIONS,

AND CRACK CLOSURE PRESSURES

In his original paper[1], Bueckner presents a weight function approach for computing the stress intensity, K. For a finite crack geometry the formulation proposed an integral equation which involves the remote applied stress, $P(x)$, where x is the distance from the crack tip,

$$K(\frac{a}{w}) = \sqrt{\frac{2}{\pi}} \int_0^a H(a,x) P(x) dx \qquad \text{(A2.1)}$$

where

$$H(a,x) = \frac{1}{\sqrt{x}} (1 + m_1 \frac{x}{a} + m_2 (\frac{x}{a})^2) \qquad \text{(A2.2)}$$

and

---

[1]Bueckner, H., "Weight Functions for the Notched Bar", Zeitschift fur angewandte Mathmatik und Mechanik 51, pp.97-109, 1971

$$m_1(\frac{a}{w}) = 0.6147+17.1844(\frac{a}{w})^2+8.7822(\frac{a}{w})^6 \qquad \text{(A2.3)}$$

$$m_2(\frac{a}{w}) = 0.2502+3.2889(\frac{a}{w})^2+70.0444(\frac{a}{w})^6 \qquad \text{(A2.4)}$$

For a uniform remote stress without bridging, we can use $P(x)=\sigma^\infty$, and arrive at

a closed form solution for the stress intensity

$$K(\frac{a}{w}) = 2\sigma^\infty\sqrt{\frac{2a}{\pi}} \;[1+\frac{m_1(\frac{a}{w})}{3}+\frac{m_2(\frac{a}{w})}{5}] \qquad \text{(A2.5)}$$

Bueckner goes on to show that this formulation agrees to better than 1% with the

type of solution presented by Tada [Ref 25] for a/w<0.5. The advantage of the

weight function method over that of Tada is that for bridged cracks, P(x) can be

modified to include crack face tractions from bridged fibers, and also that the

entire COD profile be can easily computed because of the unique relationship

between these weight functions and the crack opening displacements. However,

for a/w>0.5, or for other than pinned loading, errors in computed stress

intensities and CODs can exceed an order of magnitude.

Consequently, an alternate weight function for predicting K, originally proposed

by Bueckner for an infinite crack in a half space, was modified as part of this

127

work to account for a finite specimen geometry. For an unbridged crack this relationship becomes

$$K(\frac{a}{w}) = \sigma^\infty \sqrt{\frac{2}{\pi(w-a)}} \int_0^a [(\frac{x}{x+(w-a)})^{-1/2} + 0.6147(\frac{x}{x+(w-a)})^{1/2}$$
$$+ 0.2502(\frac{x}{x+(w-a)})^{3/2}]dx \quad \text{(A2.6)}$$

This expression cannot be integrated in closed form, is not listed in tables of integrals, and must be integrated numerically. The dimensionless stress intensity, F, frequently referred to as the shape factor, can be defined as

$$F = \frac{K}{\sigma^\infty\sqrt{\pi a}} \quad \text{(A2.7)}$$

The shape factor vs a/w is shown in Figure A2.1 for the Bueckner finite, Bueckner infinite, and Tada solutions. Also shown are results of Dao to be discussed shortly. The differences in these formulations are readily apparent, especially for a/w>0.5. These Bueckner and Tada solutions were derived using a pin loading approach and may not be appropriate for unidirectional composites using friction grips.

In fact, a recent paper[2] using finite element methods has shown that finite

---

[2]Dao, T. and Mettu, S., "Analysis of an Edge-Cracked Specimen Subjected to Rotationally-Constrained End Displacements", NASA Johnson Space Center Report 32171 (LESC 29683), August 1991

specimen lengths with rotationally constrained end displacements (ie, friction

grips) greatly alters the shape factor. Figure A2.1 shows the shape factor, F, for

two different specimen gage length, L, to width, W, ratios: L/W=1 and L/W=4.

The rotationally constrained shape factor for L/W=4 has been experimentally

verified[3]. The L/W=1 shape factor is remarkably similar to the infinite crack

Bueckner weight function. Since L/W=4 for these experiments, the infinite crack

weight function was further modified via curve fitting to Dao's data while

retaining the essential singularities. The resulting equation is

$$K(\frac{a}{w})=\sigma^{\infty}\sqrt{\frac{2}{\pi(w-a)}}\int_0^a [(\frac{x}{x+(w-a)})^{-1/2} + 0.6147x^{-0.25}(\frac{x}{x+(w-a)})^{1/2} \qquad \text{A2.8}$$
$$- 0.2502x^{-0.36}(\frac{x}{x+(w-a)})^{3/2}]dx$$

This new formulation, which includes position dependent coefficients on the

second and third terms, is far more efficient than the many finite element

solutions generated by Dao. Furthermore, fiber bridging can easily be included

and CODs determined via a second integration, neither of which can be done

without complicated finite element models. It should be noted that while the

---

[3]Blatt, D., "An Investigation of the Fatigue Crack Growth Behavior of a Titanium Matrix Composite Under Thermomechanical Loading", Proceedings of the Seventh Thermomechanical Fatigue Workshop, NASA Lewis Research Center, Cleveland, Ohio, December 1992

shape factor of both the Bueckner finite and infinite weight functions is independent of the specimen width, the weight function modified for L/W=4 is a weak function in W. As the specimen width is increased from five to twenty-five millimeters, for example, the shape factor decreases about ten percent for all a/w.

Stress Intensity Solutions

The grips used for the vf15#1, vf37, and vf41#1 tests were friction grips with serrated wedges. The wedges were clamped via two opposing spherical seated bolts which passed through the cylindrical grip body. When tightly clamped into one grip, the specimen could easily be rotated via a small impact with a screw driver. The angle of easy rotation was at least ten degrees from the specimen centerline. This free rotation of the grips used here implies that a pinned solution, with its higher shape factor, should be used when computing the stress intensity. The measured ΔCODs agree very well with those predicted using the shape factor for pinned grips (ie, Bueckner finite crack or Tada solutions) at a/w=0.5. However, the shape factor for rotationally constrained grips (ie, Bueckner infinite crack, modified for L/W=4.0) predicted unbridged ΔCODs less than those actually measured with bridging for vf37 and vf41 with a/w=0.5. In addition, the Tada

solution is appropriate even at large a/w because the maximum possible specimen rotation predicted for the unreinforced matrix (which does not experience fiber bridging) is less than the ten degrees of easy rotation demonstrated for these grips. The extent of matrix plasticity measured at fracture, as discussed in the text, suggests, however, that the grip used for the vf15#1, vf37, and vf41#1 may have actually been at least partially constrained and hence the appropriate shape factor may be between these two extremes. The grips used for the vf15#2, vf41#2, and vf41#3 tests were rotationally constrained. Unfortunately, COD and fracture data are not available at large a/w for both grips.

The formulation given by Tada for a pinned grip and an unbridged crack is

$$K = F\sigma\sqrt{\pi a} \qquad\qquad \text{(A2.9)}$$

where σ is the applied stress, a is the total crack length, and F is the shape factor dependent upon the ratio, ß, of crack length to specimen width (ß=a/w). For ß<0.6,

$$F = 1.122 - 0.231\beta + 10.55\beta^2 - 21.71\beta^3 + 30.382\beta^4 \qquad \text{(A2.10)}$$

and for ß>0.6

$$F = 0.265(1-\beta)^4 + \frac{(0.857+0.265\beta)}{(1-\beta)^{3/2}} \qquad (A2.11)$$

Crack Closure Pressures

In the derivation of the closure pressure, $c(x)$, for the single edge notch geometry

mechanics of materials requires that if the bridged fibers act as a continuum with

the remaining undamaged composite, and if the notch stress concentration has

been relieved, and if the stress state is not producing plastic deformation in the

fibers, then

$$c(x) = \sigma^\infty(\frac{w}{w-a_0} + \frac{6wa_0[0.5(w-a_0)-(x-a_0)]}{(w-a_0)^3}) \qquad (A2.12)$$

The first term is the net section stress and the second term is the bending

moment induced stress. The assumption that plastic deformation does not occur

in the fibers is reasonable because they are ceramic and hence allows

superposition of the net section and bending induced stress fields. However, that

the fibers act as a continuum and that the notch effects have been relieved is a

little more difficult to justify. To validate these assumptions a three dimensional

macro/micro finite element model was generated and is presented Chapter 4. It

is shown that indeed the notch effects have been relieved and that the stress

distribution in the bridged fibers is remarkably similar to that given by the above equation. Apparently, this crack pressure formulation includes all the necessary mechanics, is reliable, and was used in the analysis.

APPENDIX 3

MEASUREMENT OF MATRIX RESIDUAL STRESSES

Earlier in this work matrix plasticity was directly measured and used to estimate the effective matrix stress intensity. Similar measurements can also be used to predict the longitudinal residual stress state in the matrix. Consider a stress-strain curve for a [0] SCS-6/Ti-15-3 composite [Vf=34, Ref 4] with its appreciable decrease in slope at an applied stress level of approximately 800 MPa. This decrease in the instantaneous composite modulus is generally attributed to the onset of matrix plasticity. Chapter 2 presented the following method for estimating the matrix stress using rule-of-mixtures and fiber/matrix strain compatibility conditions

$$\sigma_m^A = \frac{\sigma_c^A}{[1 + V_f (\frac{E_f}{E_m} - 1)]} \tag{A3.1}$$

where the superscript A denotes the applied stress and subscripts m, f, and c denote the matrix, fiber, and composite, respectively. The 800 MPa applied

composite stress results in an estimated 354 MPa matrix stress. The longitudinal matrix residual stress is estimated to be 356 MPa. Since the prediction is for the onset of plasticity, superposition is valid and the two stresses can be added to predict a net matrix stress of 710 MPa: the yield stress of Ti-15-3[4].

Room temperature tensile tests were interrupted just below and just above the 800 MPa applied stress level, heat treated, and etched to reveal the extent of matrix plasticity[5]. As expected, below the 800 MPa composite stress, microplasticity was observed at grain boundaries and some fiber/matrix interfaces. Above the 800 MPa composite stress extensive plasticity was observed. Apparently, this experimentally verifies the 356 MPa longitudinal matrix residual stress predicted by finite elements. The longitudinal matrix residual stress in this same material with a fiber volume fraction of 0.34 was measured using the x-ray diffraction technique[6] and is identical to the 356 MPa value estimated here.

---

[4]Lerch, B. and Saltsman, J., "Tensile Deformation Damage in SiC Reinforced Ti-15V-3Cr-3Al-3Sn", NASA Technical Memorandum 103620, April 1991

[5]Private Communication with Dr. B. Lerch at NASA Lewis, January 1993

[6]Brown, K., Hendricks, R., and Brewer, W., "X-Ray Diffraction Measurements of Residual Stresses in SiC/Ti Composites", Fundamental Relationships Between Microstructure and Mechanical Properties of Metal Matrix Composites, Edited by P. K. Liaw and M. N. Gungor, The Minerals, Metals, and Materials Society, pp.269-286, 1990
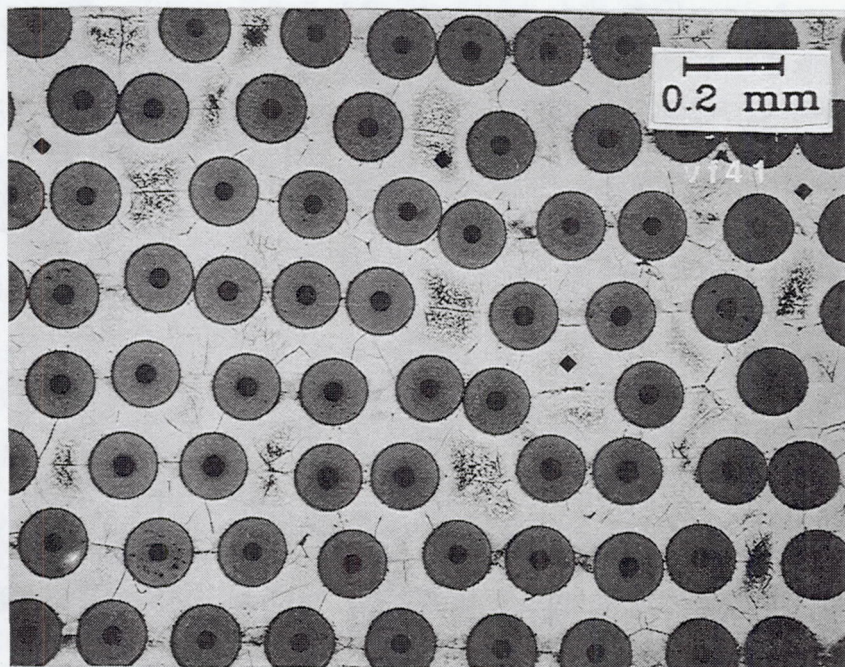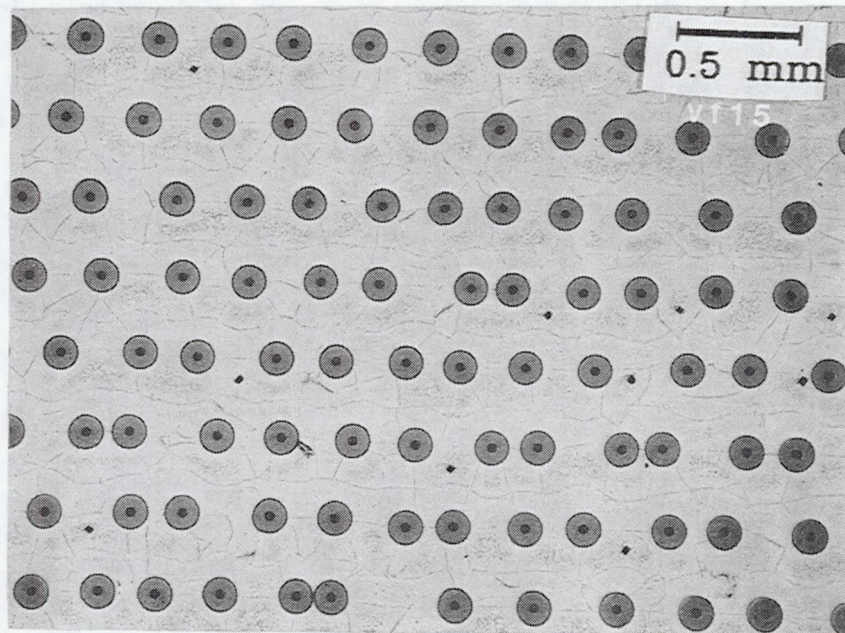
Figure 1.1: Optical photos of the polished and etched vf15 and vf41 cross-sections.
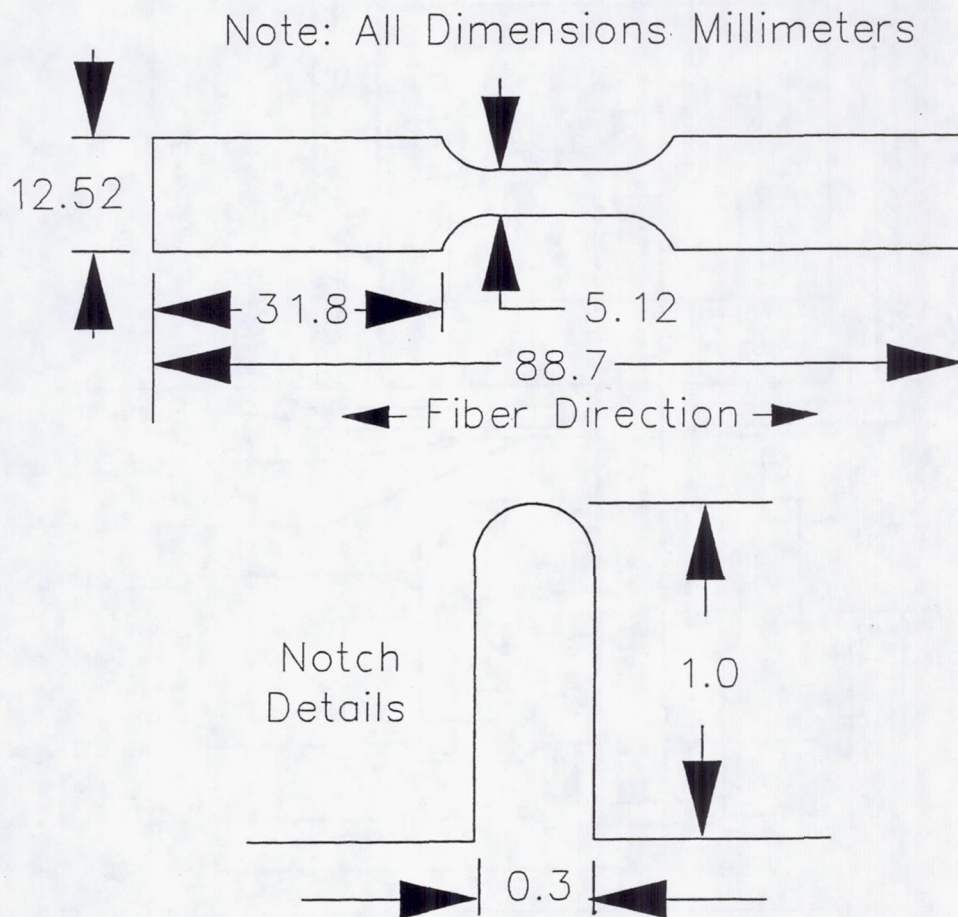
Figure 1.2: Single edge notch specimen geometry.
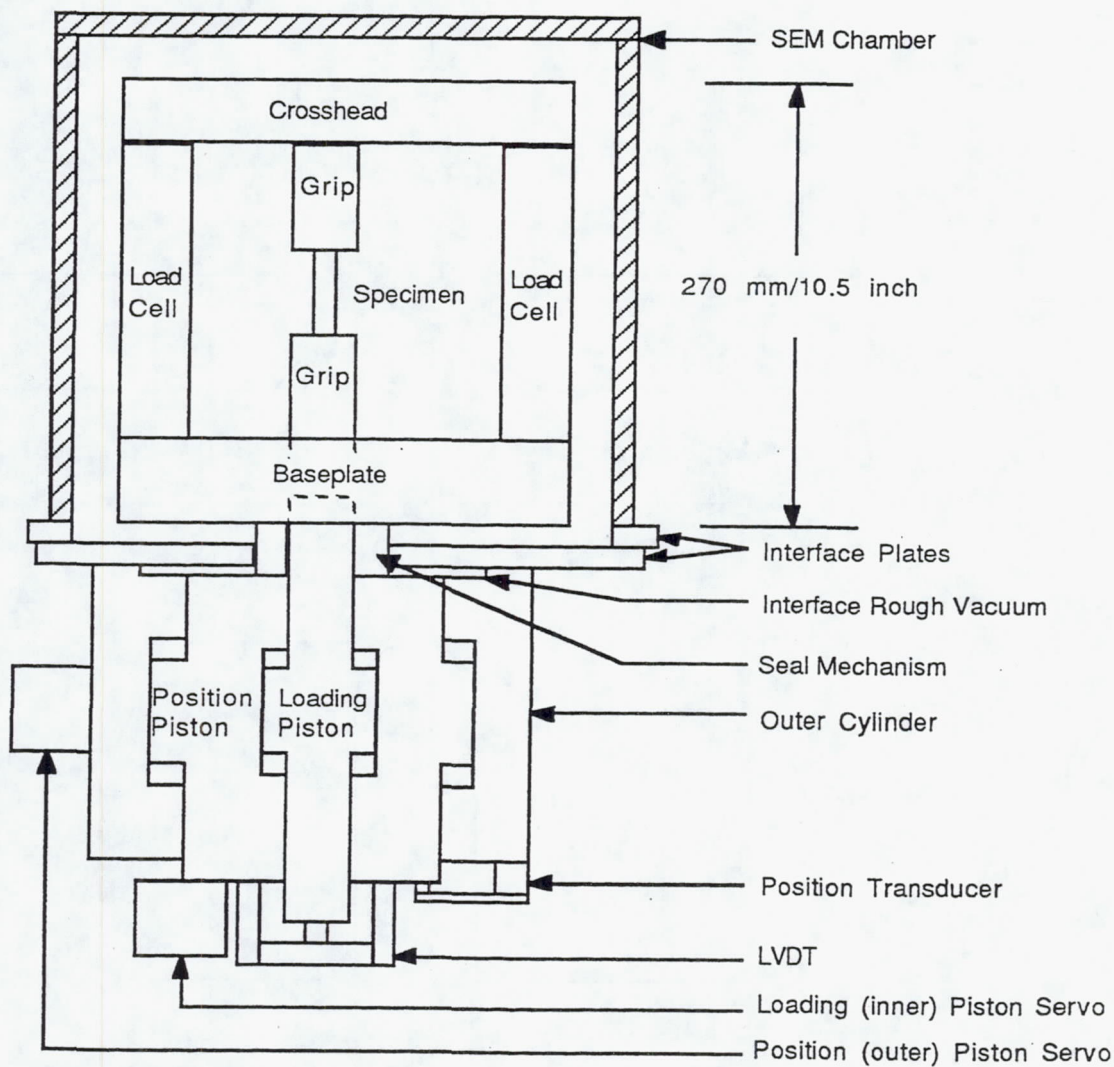
Figure 1.3: Scanning electron microscope fatigue stage schematic.
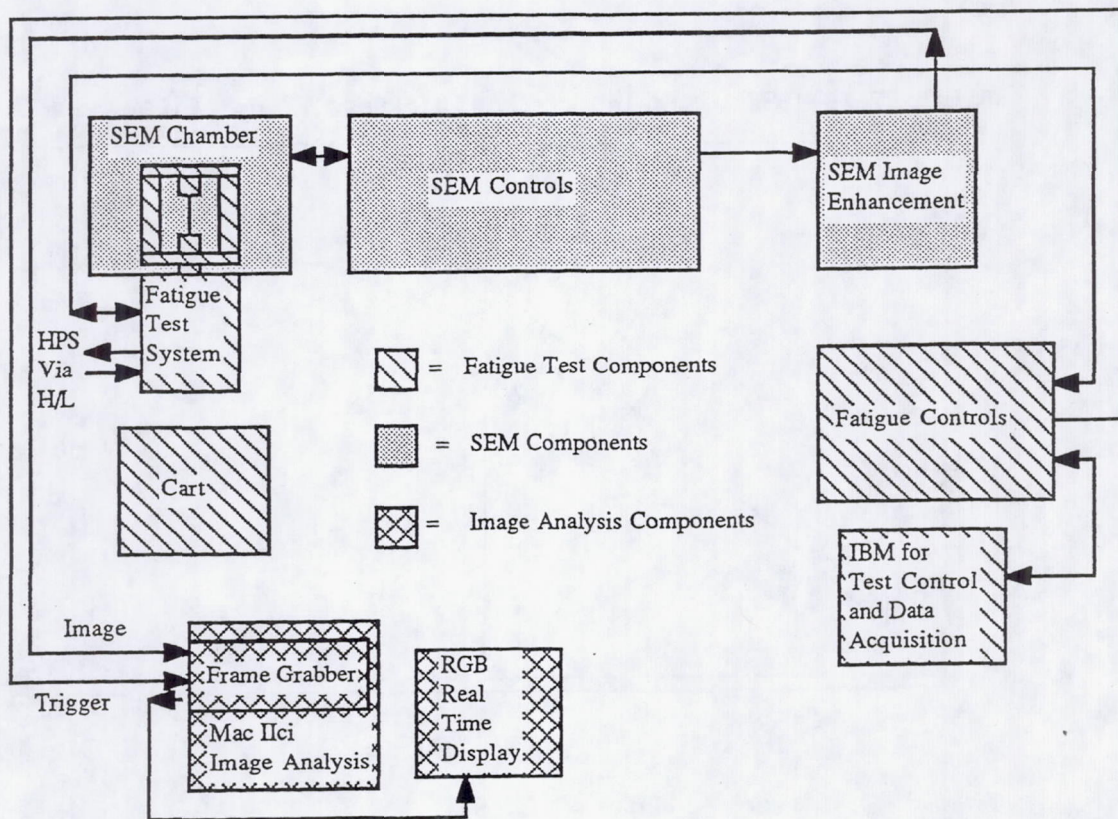
Figure 1.4: Micromechanics laboratory with image analysis.

139
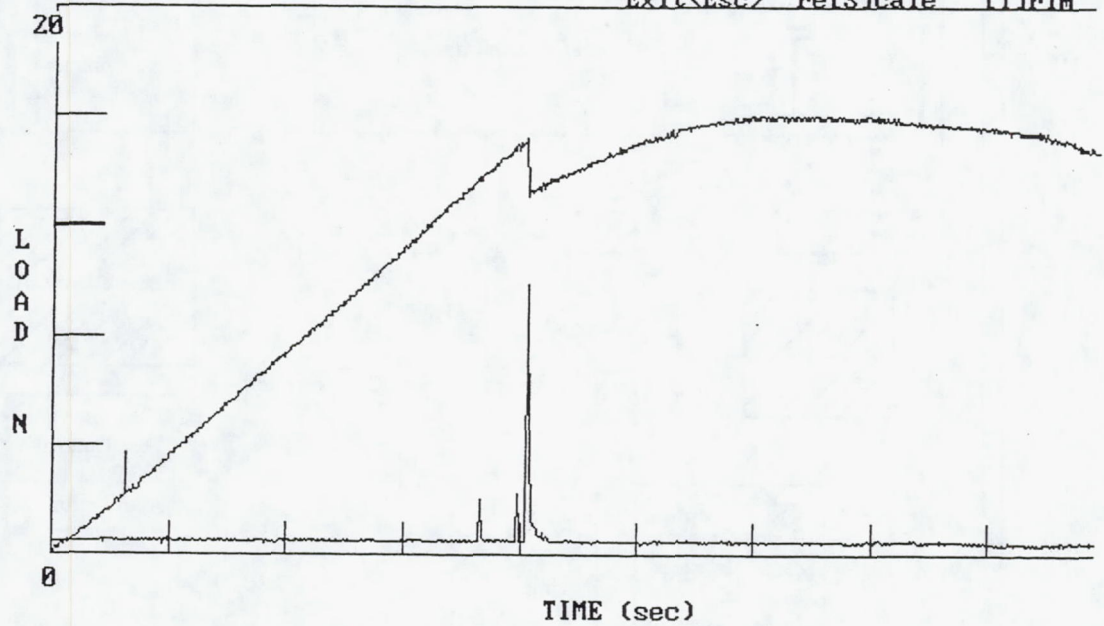
Figure 2.1: Fiber pushout load vs time plot with acoustic emission signal.

All Dimensions Microns
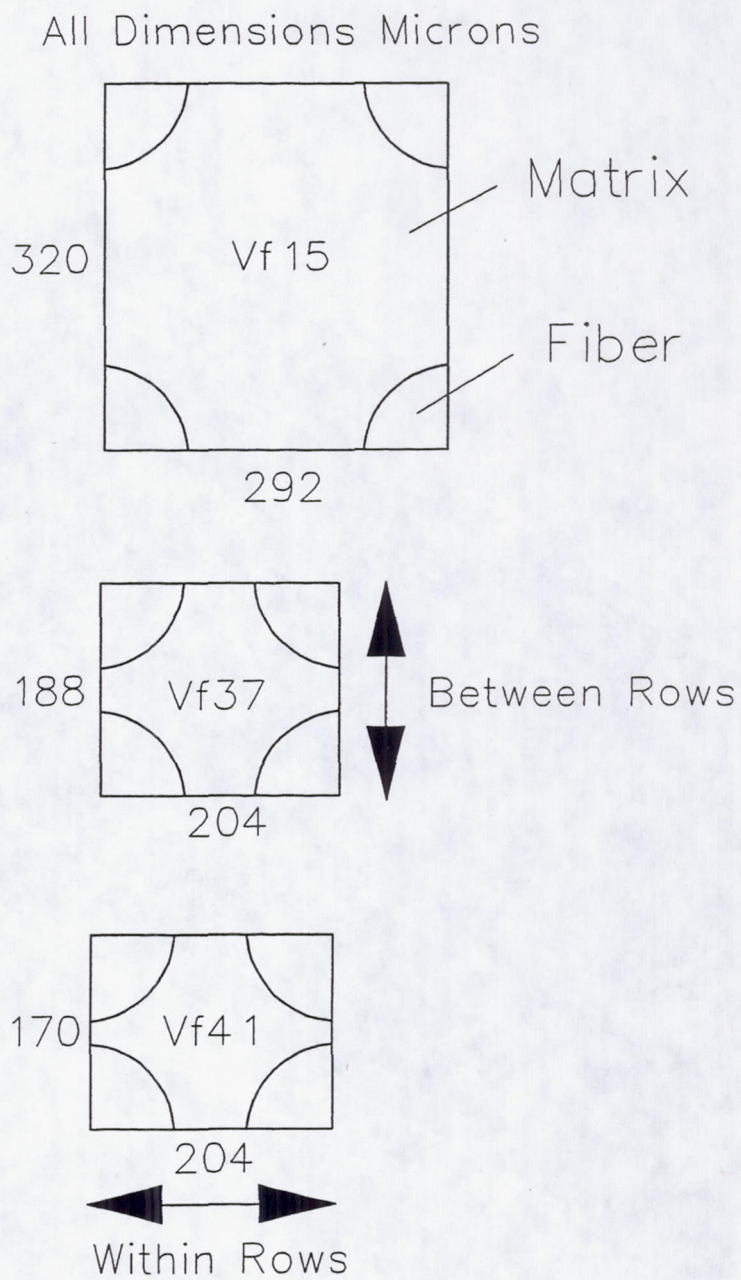
Figure 2.2: Repeated rectangular arrays used to define FEM unit cells.
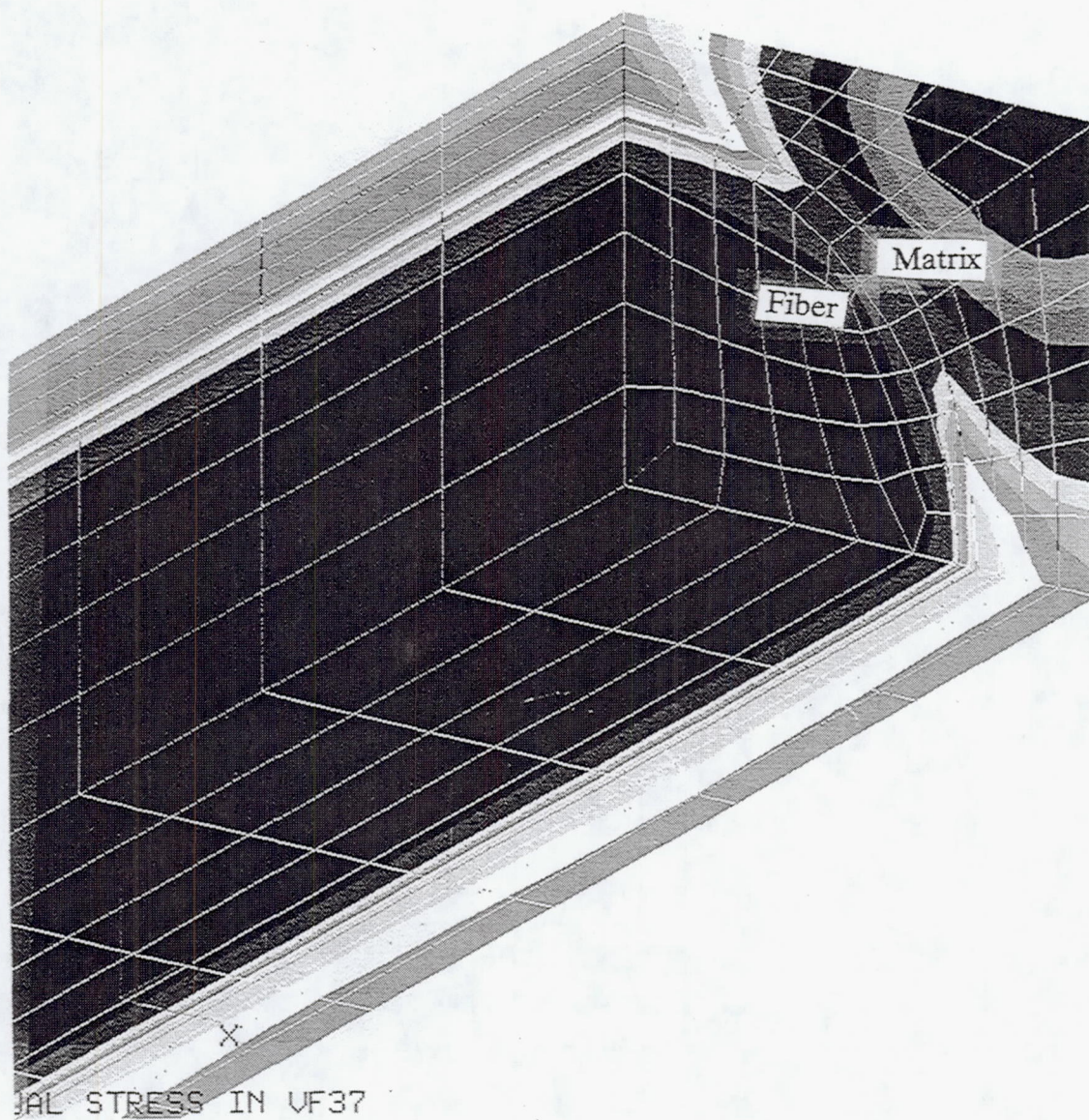
Figure 2.3: FEM mesh used for predicting residual stresses in vf37.

142
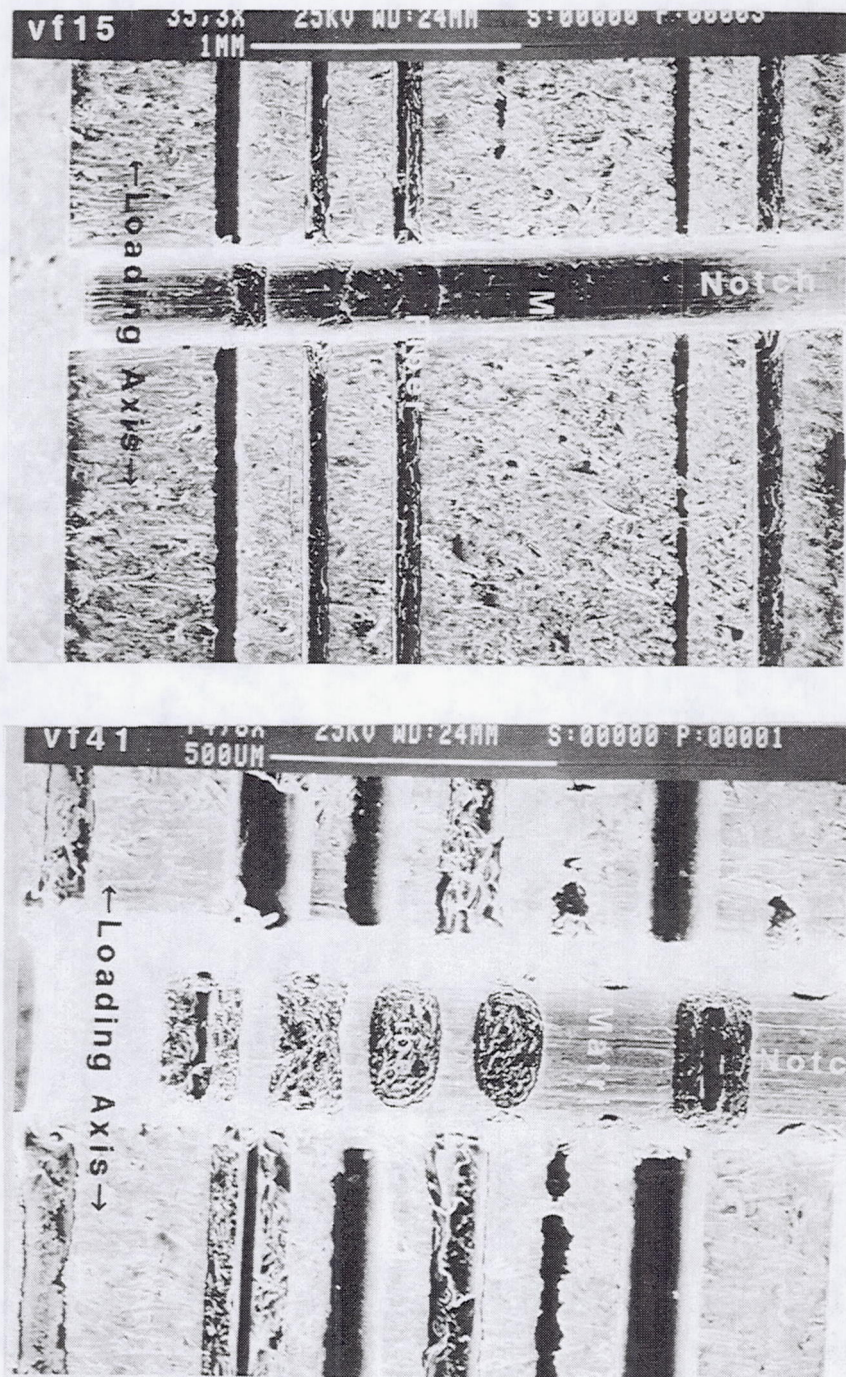
Figure 2.4: Edge on low mag notch photos showing matrix and damaged fibers.
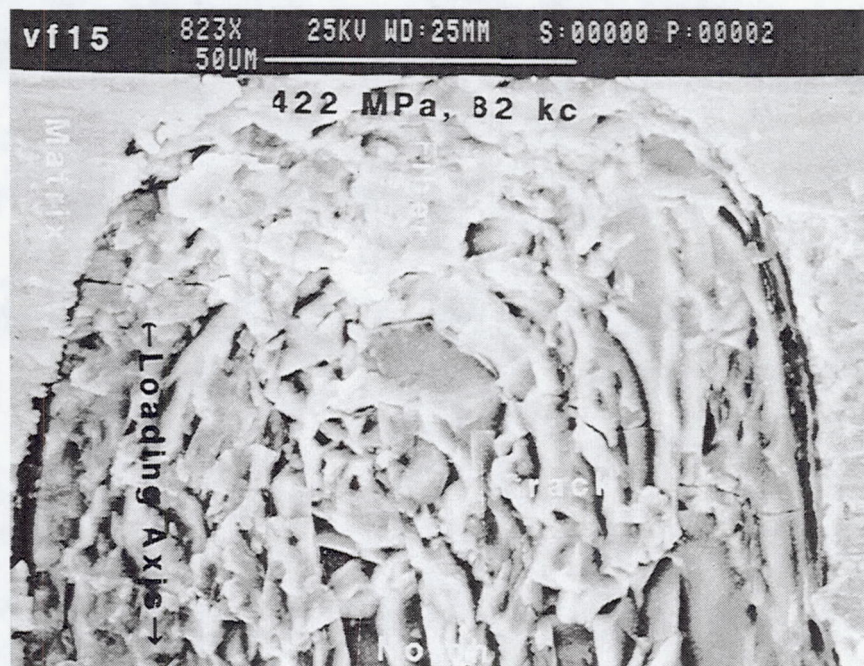
Figure 2.5:   Matrix crack initiation process shows peak stress and cumulative

cycles. Cracks initiated at the fiber/matrix interface away from the

notch root.
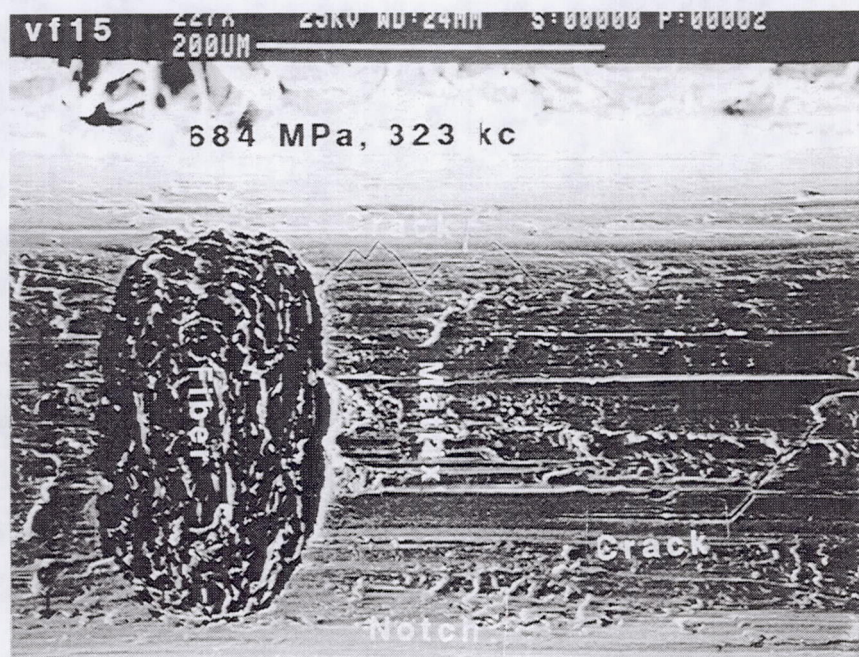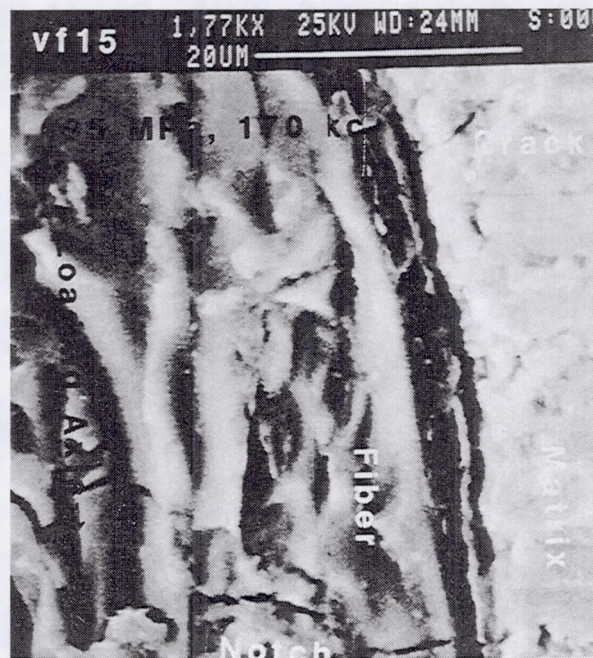
Figure 2.5: Continued

145
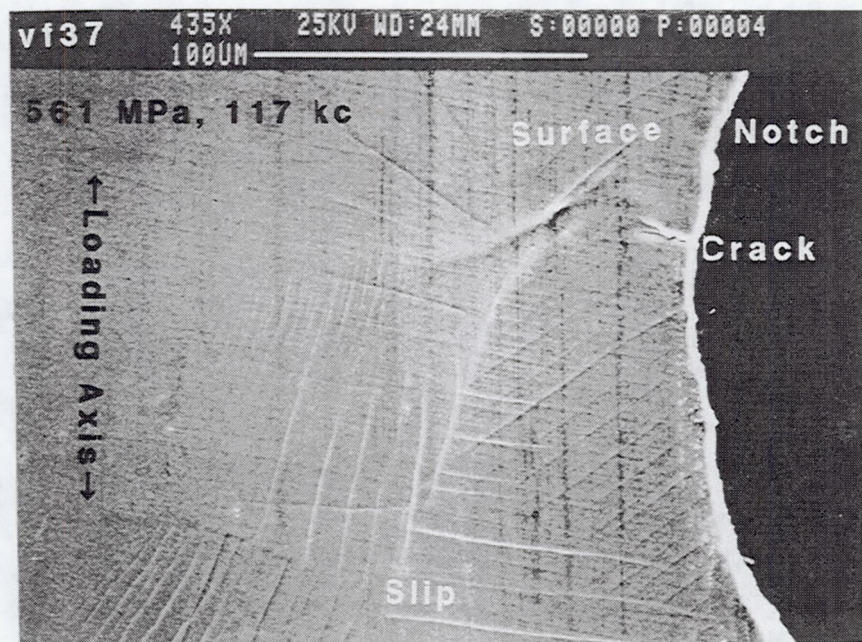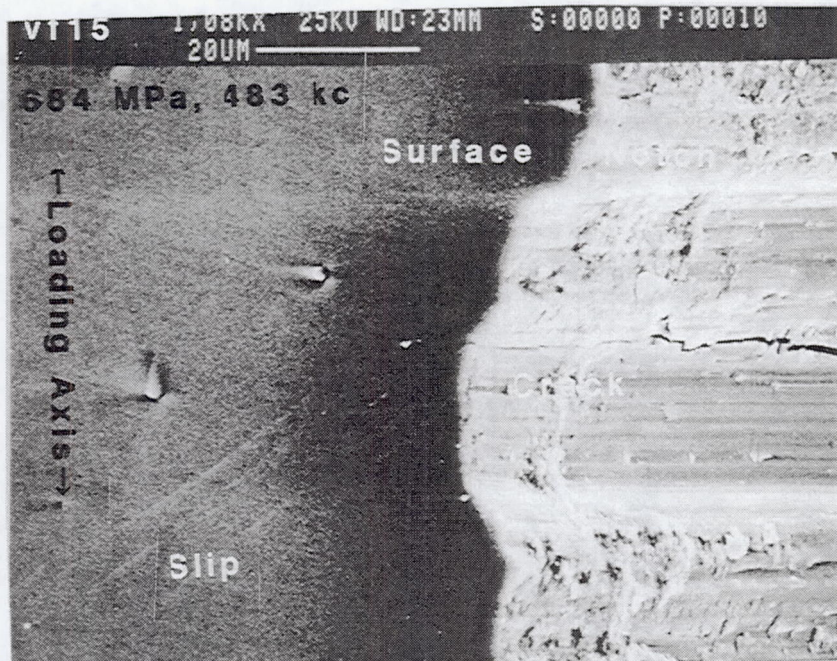
Figure 2.6: Surface slip bands of vf15 and vf37. Note the higher slip band density in the vf37 material.
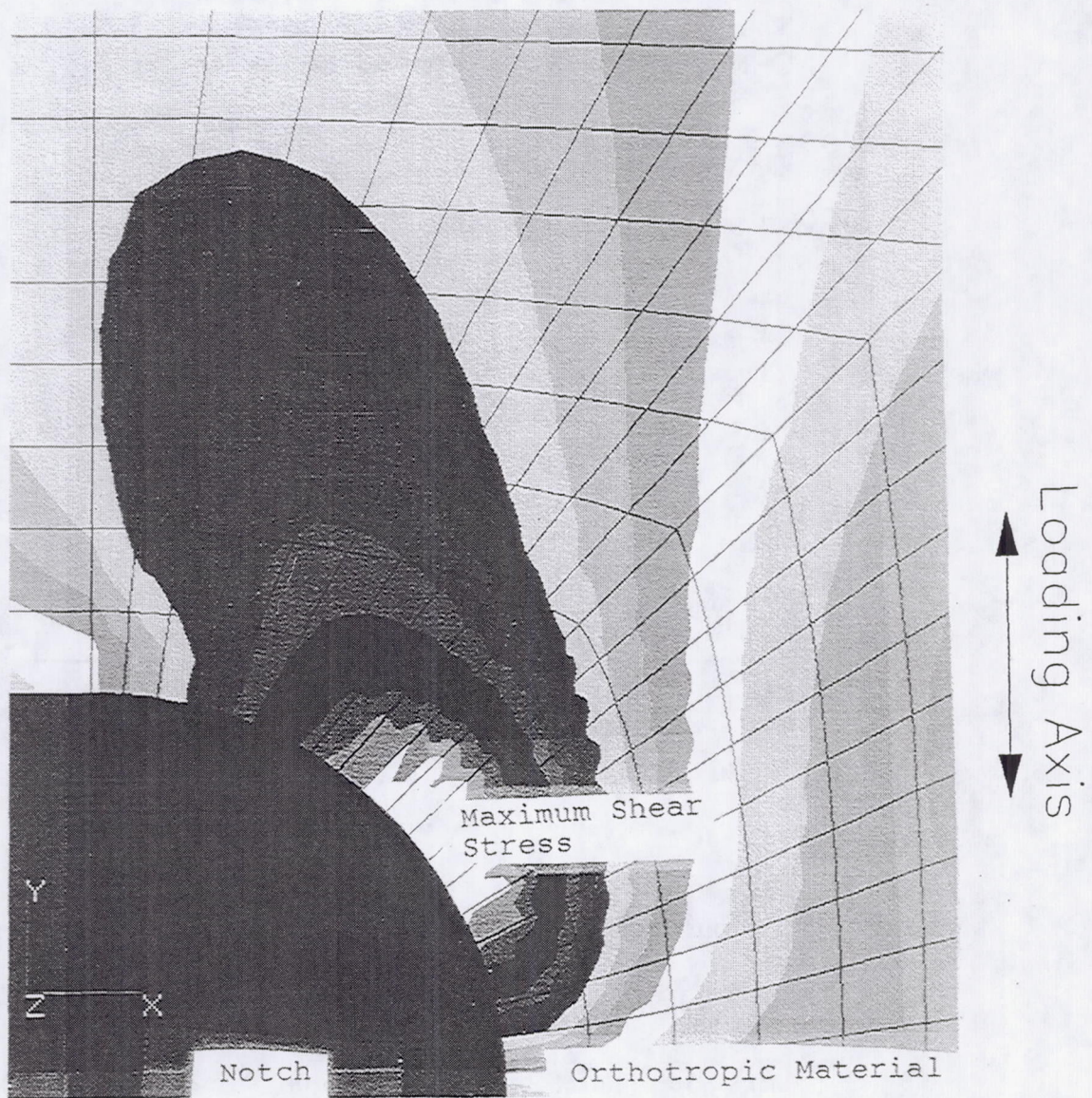
Figure 2.7: Finite element prediction of shear stress distribution in the notch

- ● Applied Composite Notch Stress, Data, $K_t \sigma_c^A$
- ▽ Applied Matrix Notch Stress, ROM, $K_t \sigma_m^A$
- ▼ Matrix Longitudinal Residual Stress, FEM, σ_m^R
- ○ Net Matrix Notch Stress at Initiation, σ_m^N
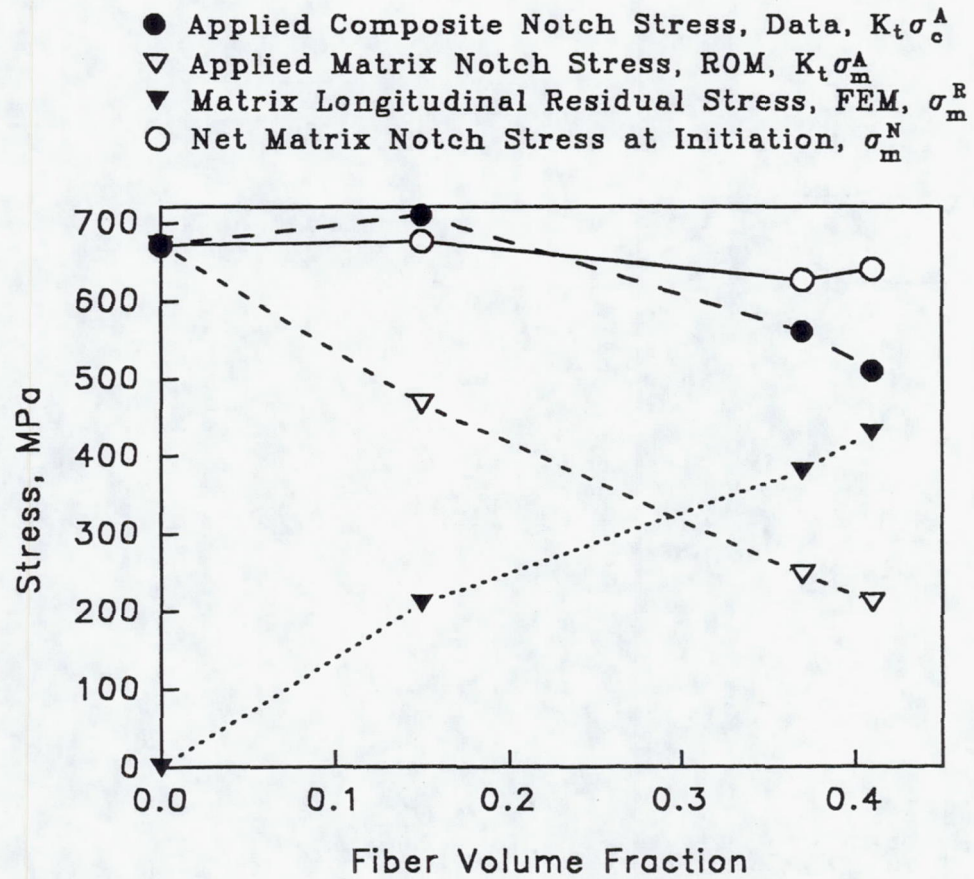
Figure 2.8: Various stress components vs fiber volume fraction. Note that while the applied matrix stress decreases for a similar applied composite stress, the matrix longitudinal residual stress increases with fiber volume fraction. Matrix cracks initiate when the net matrix stress equals the endurance limit of the matrix. Matrix (vf=0.0) data from Reference 17.

148
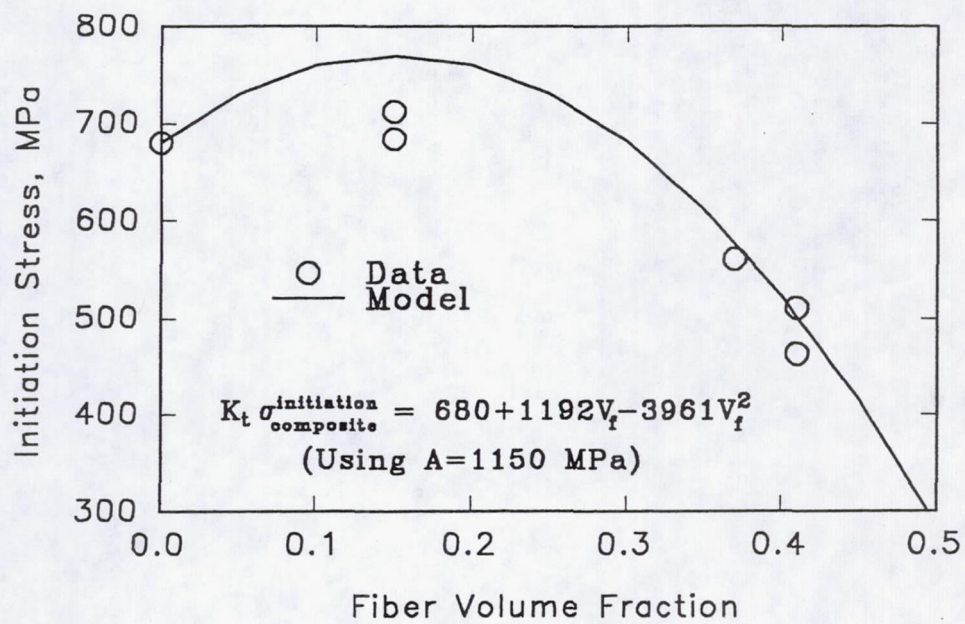
Figure 2.9: Comparison of predicted composite crack initiation stress to data.
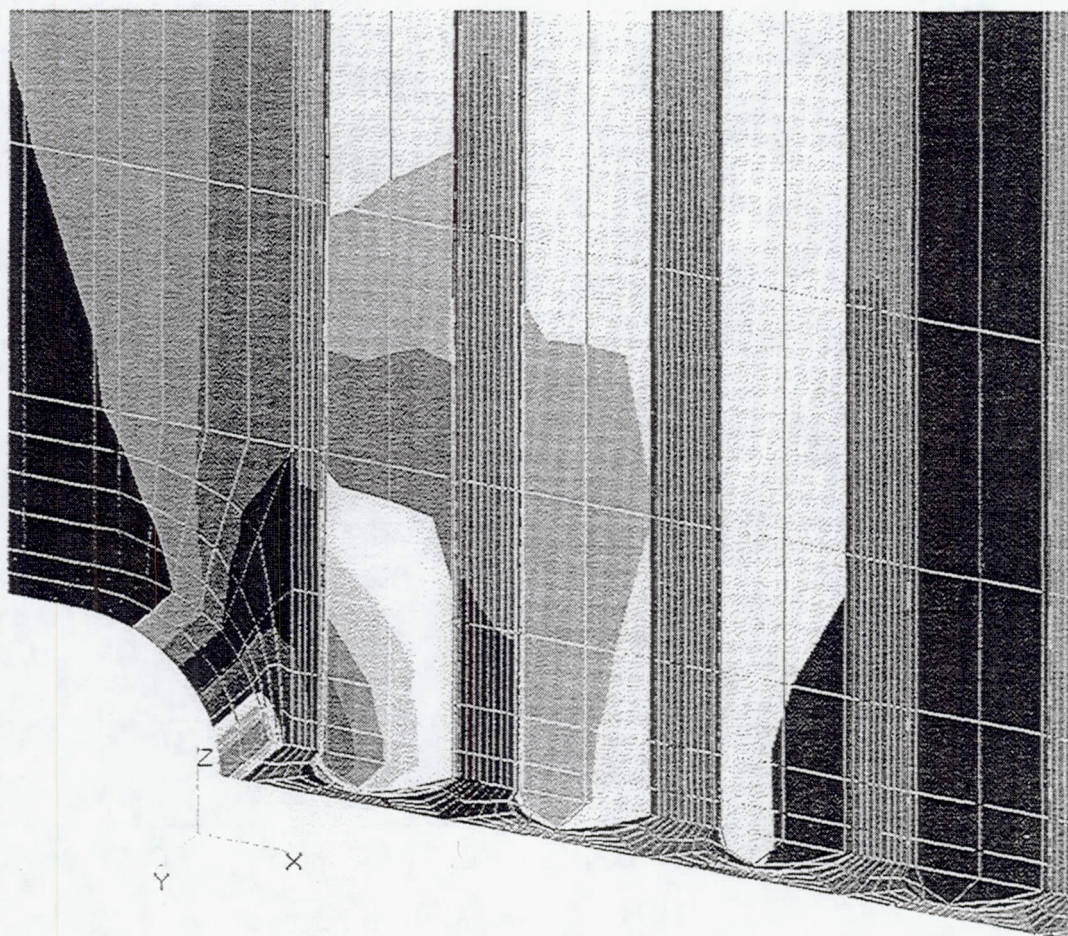
Figure 2.10: Macro/micro finite element model of vf37 shows stress concentration influence of high modulus fibers behind the notch.
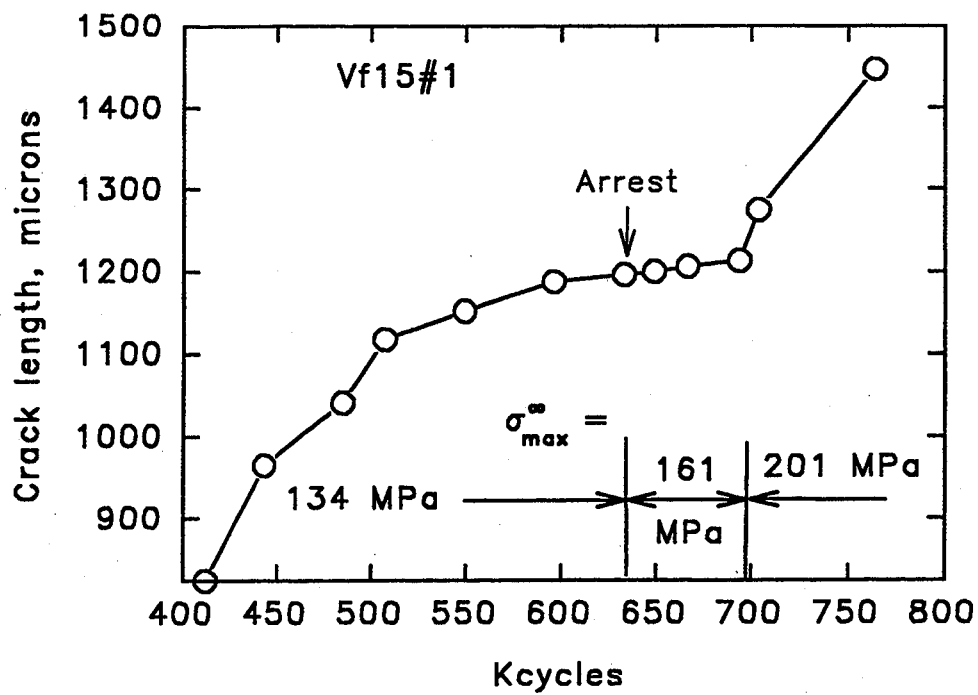
Figure 3.1: Average crack length from both sides of the specimen vs number of cycles for each fiber volume fraction. Note: scales are different.

151
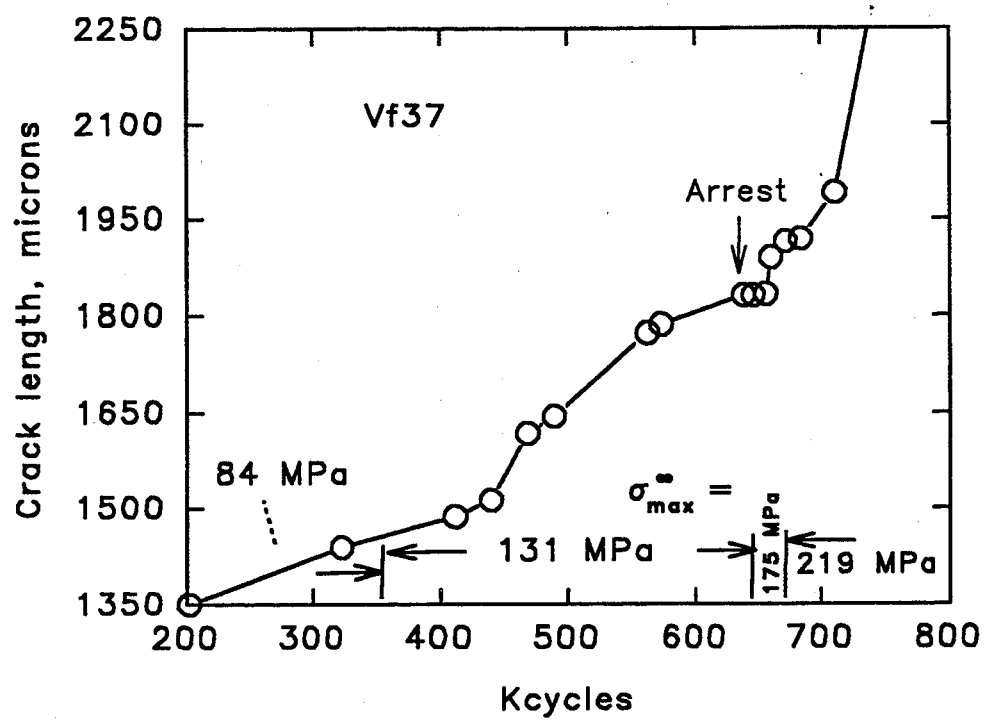
Figure 3.1: Continued
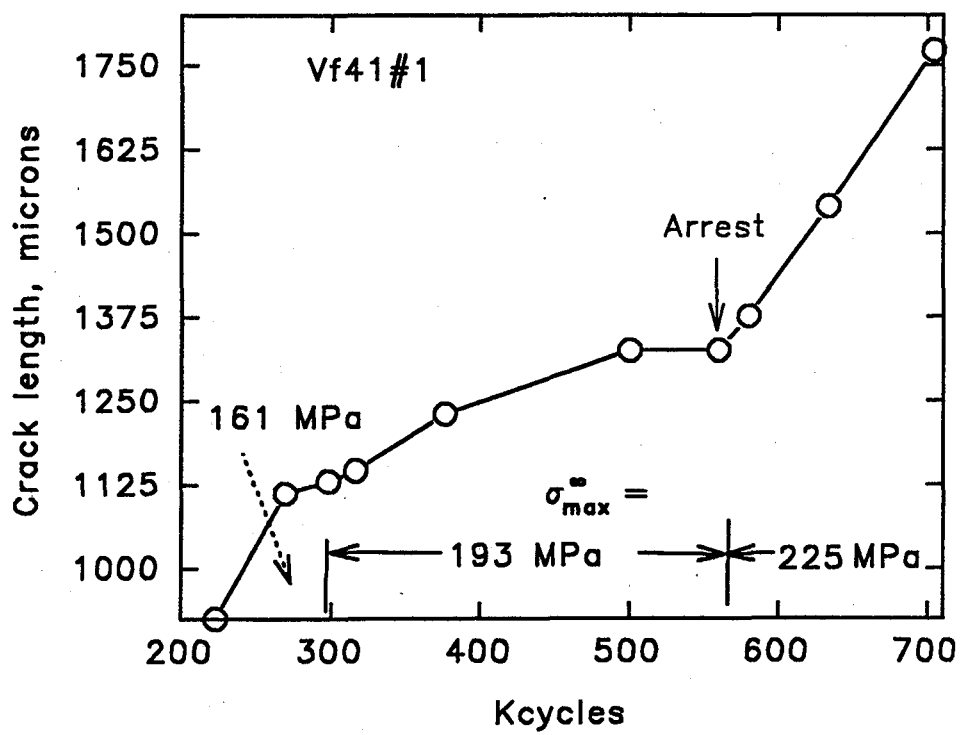
Figure 3.1: Continued
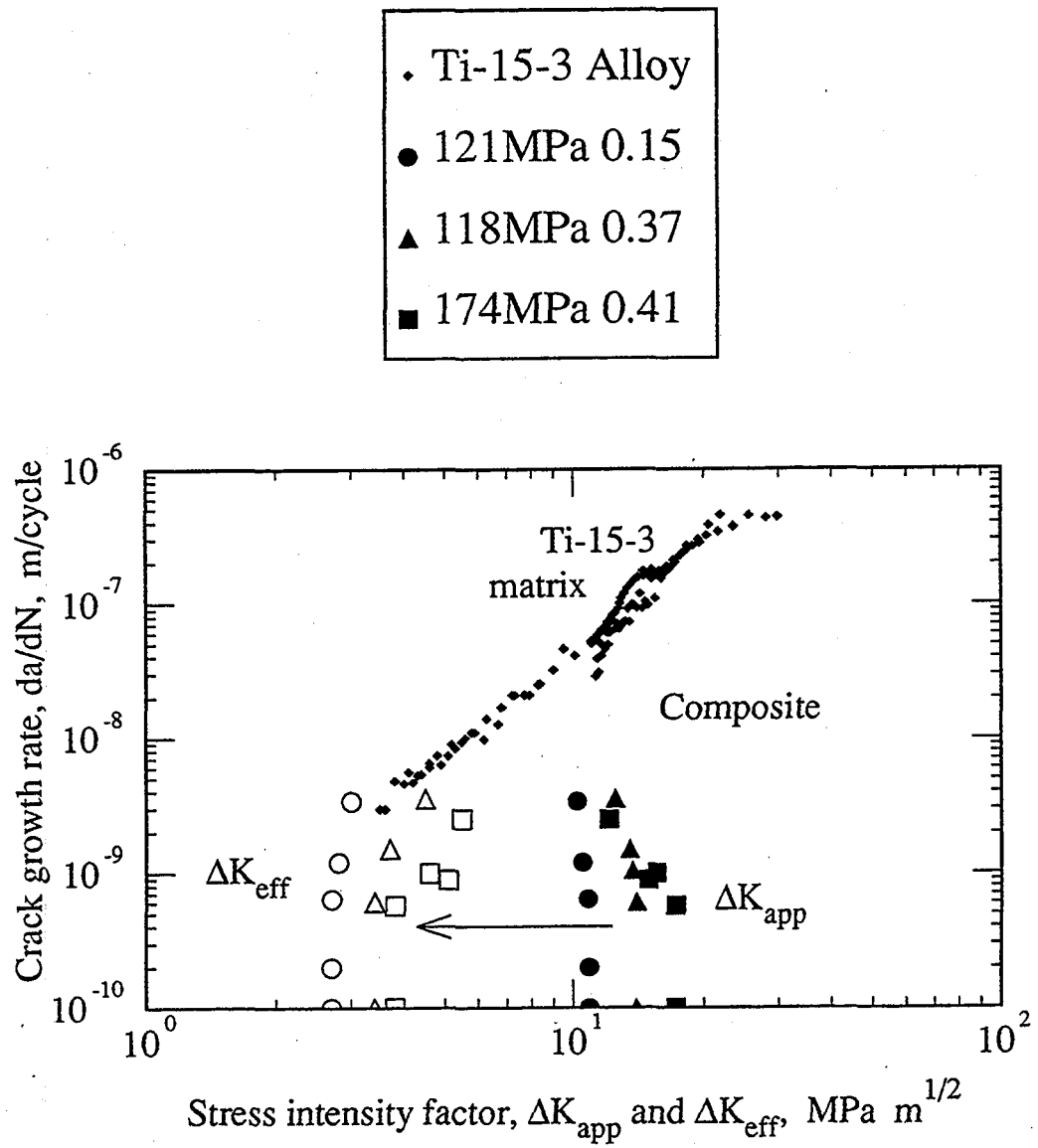
Figure 3.2: Crack growth rate vs ΔK in the region of decreasing crack growth rates for each fiber volume fraction. Matrix data from Reference 27. Solid (hollow) symbols are experimental (modeling) data.
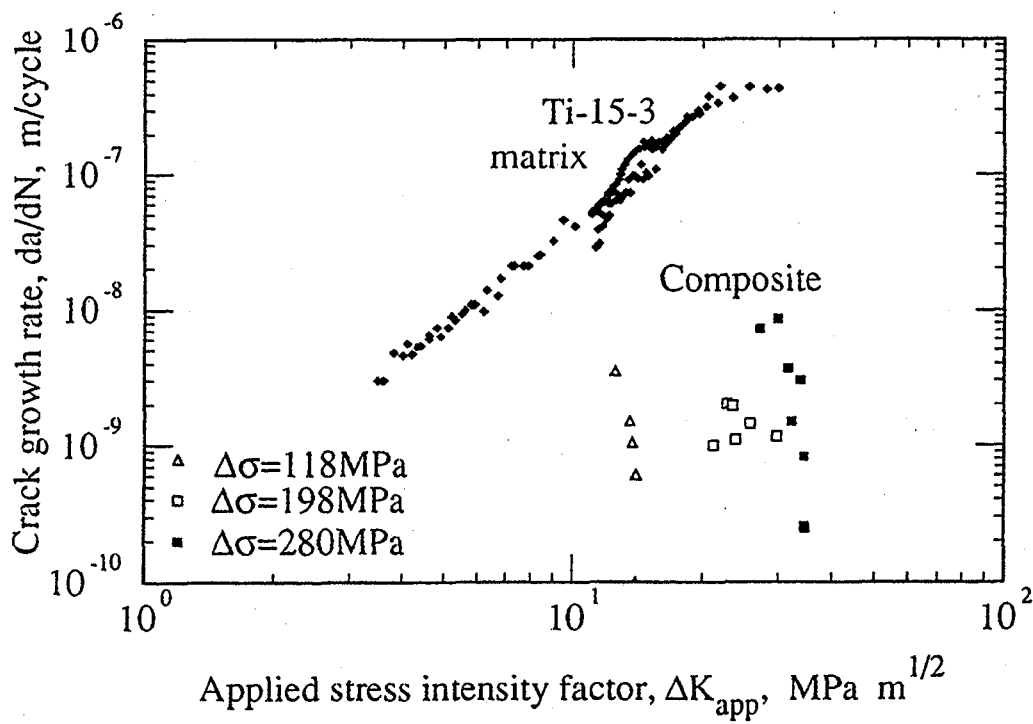
Figure 3.3: Crack growth rate vs ΔK in the region of decreasing crack growth rates for Vf37 and different applied stresses. Matrix data from Reference 27.
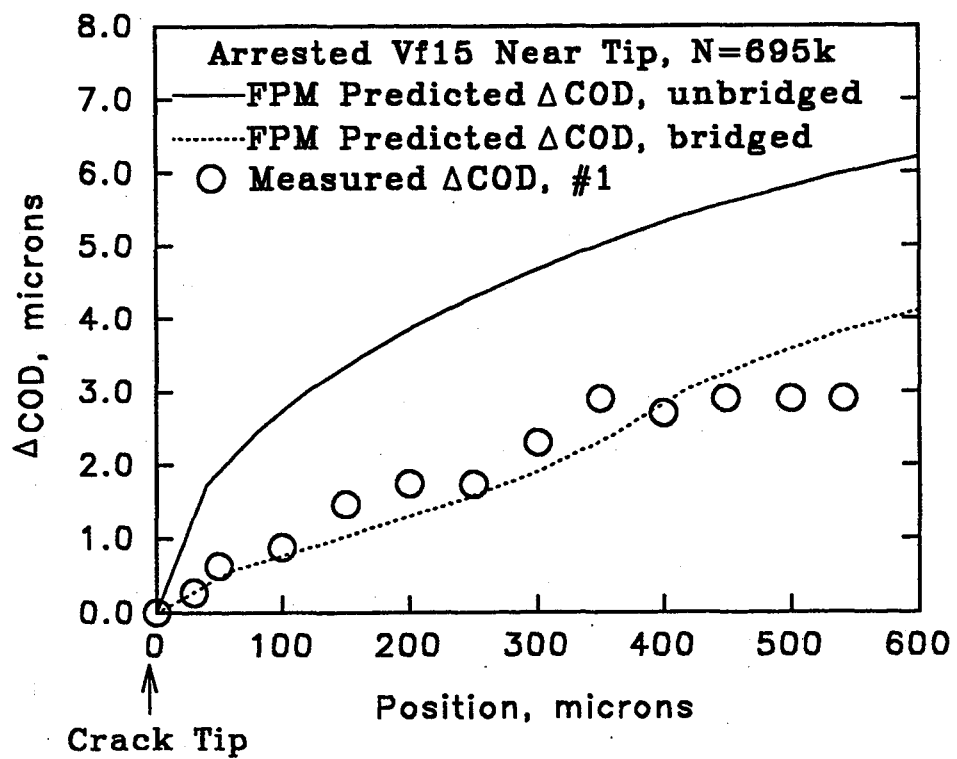
Figure 3.4: Delta COD vs position from the crack tip.
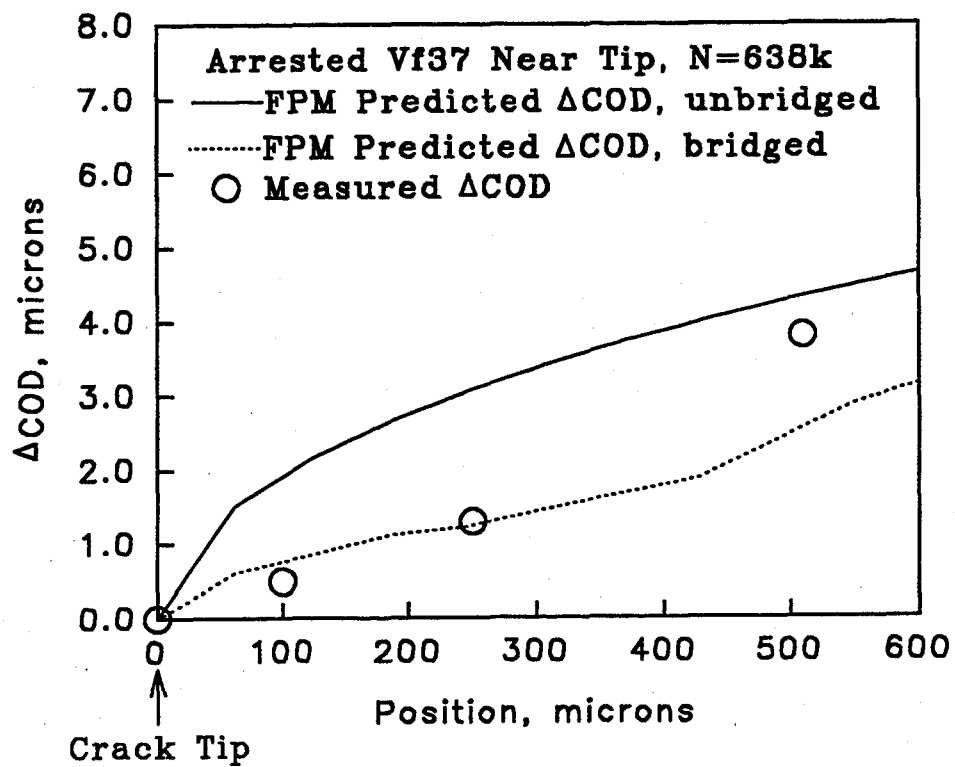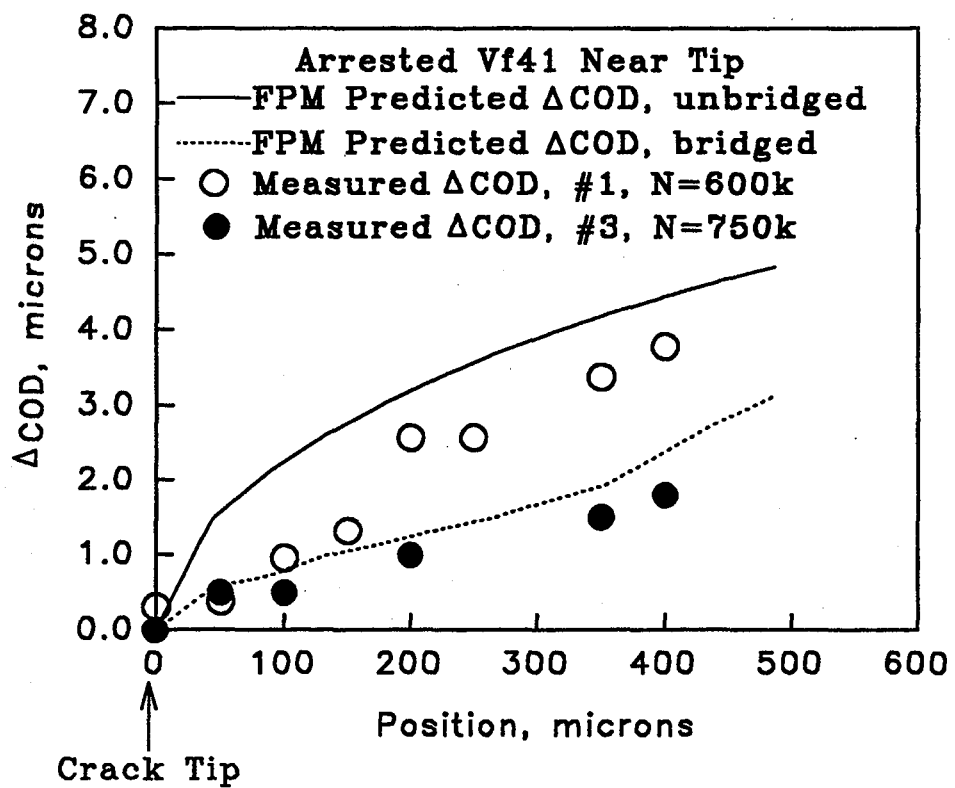
Figure 3.4: Continued

Figure 3.4: Continued

158
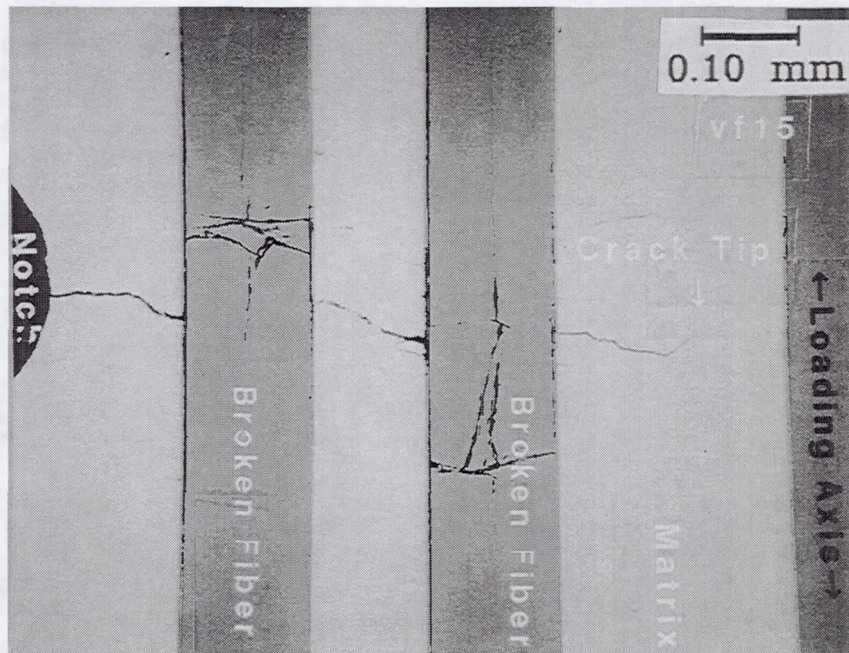
Figure 3.5: Photomicrograph of fiber bridging condition just after recommencing crack growth in the vf15 and vf41 materials. Note that while there are no intact bridged fibers in vf15#2, vf41#3 maintains an active bridge zone. Samples have been polished down to the first (second) fiber row in vf15#2 (vf41#3) after interrupting the tests at an increased stress to end crack arrest.

159
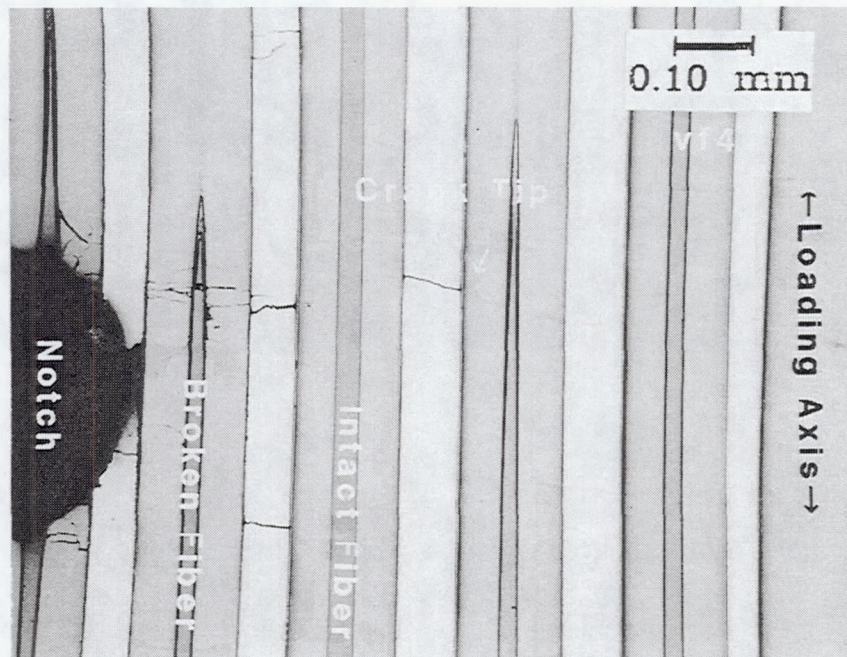
Figure 3.5: Continued

160
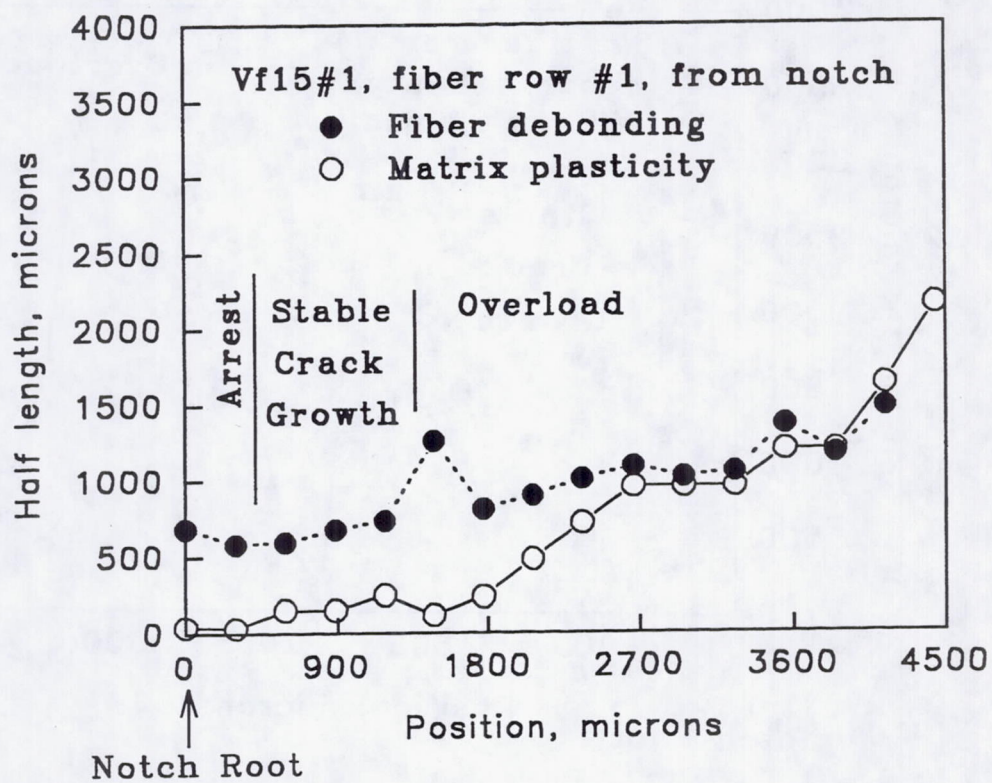
Figure 3.6: Debond and matrix plasticity half lengths vs position from the notch. The approximate regions of behavior transition are also shown.

161

Figure 3.6: Continued

162

Figure 3.6: Continued

163
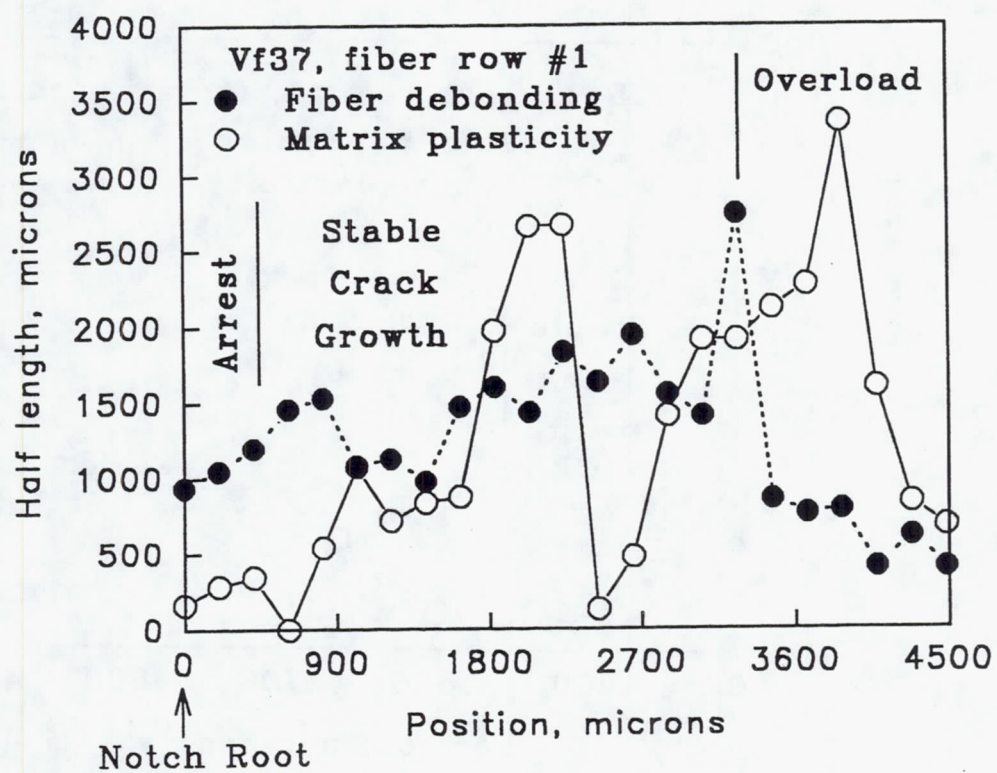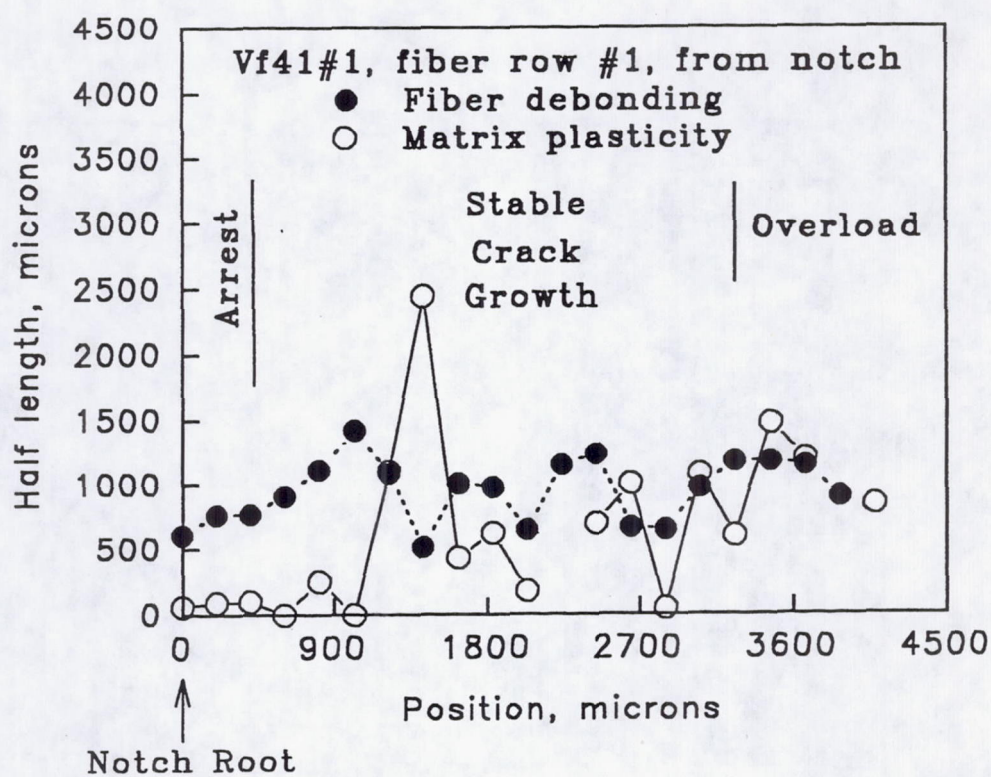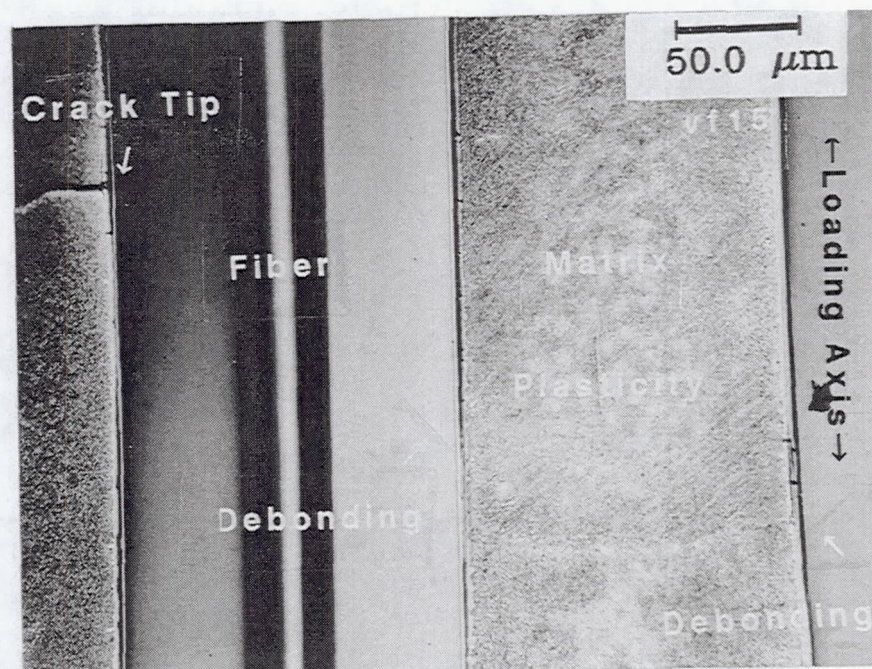
Figure 3.7: Fiber debonding and matrix plasticity ahead of the crack tip for vf15#2. Test was interrupted after increasing the applied stress to end crack arrest. The sample has been polished and etched.
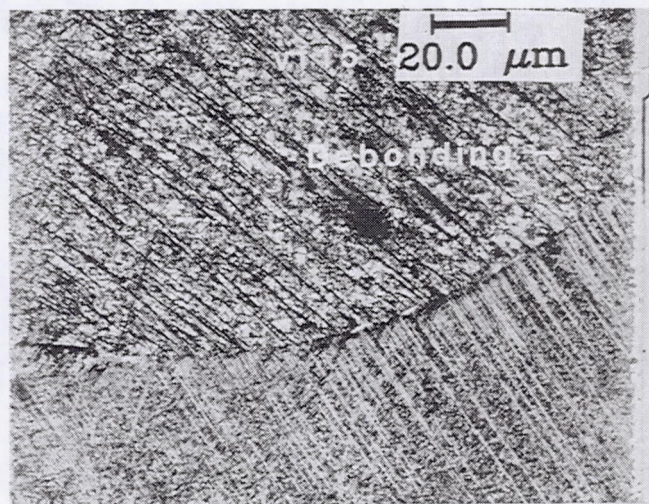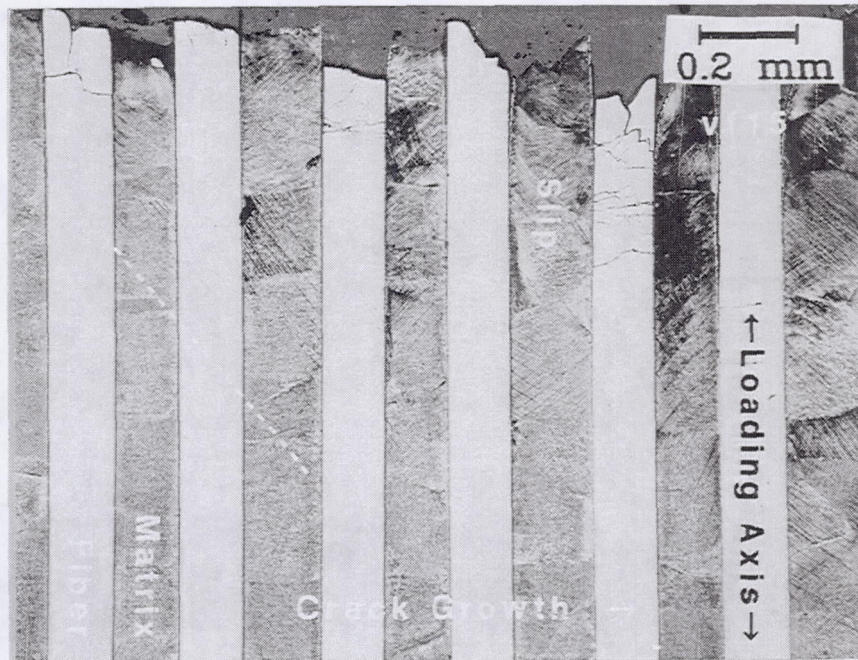
Figure 3.8: Heat treated, polished, and etched optical photo shows vf15 matrix plasticity.
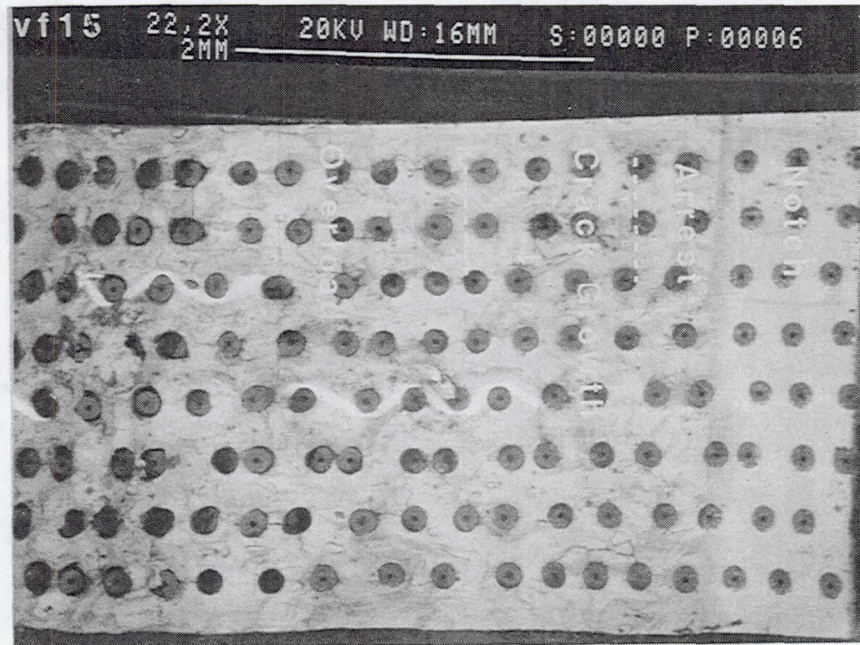
Figure 3.9: Fracture surfaces of each fiber volume fraction. The Mo-weave is the white woven structure in this backscattered electron image.
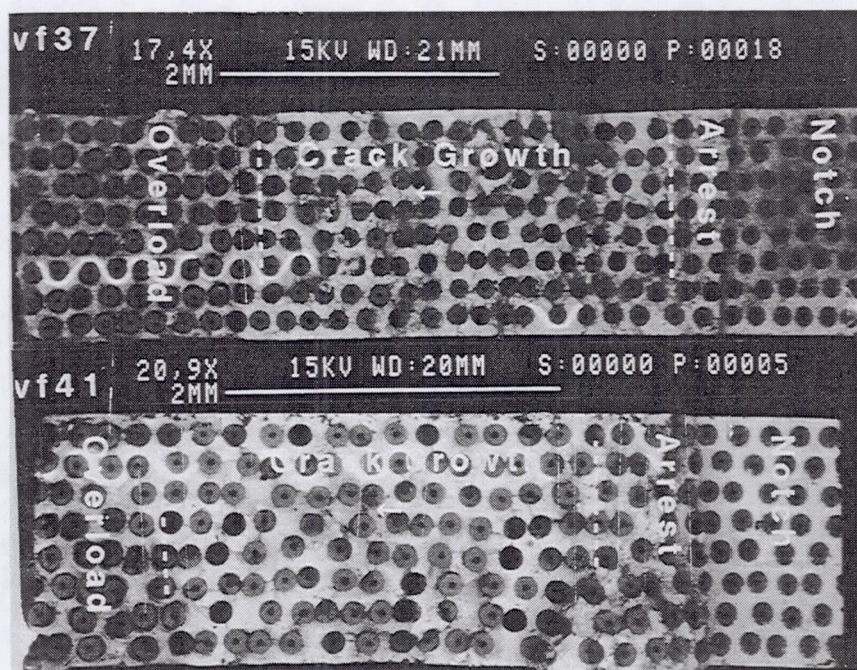
Figure 3.9: Continued
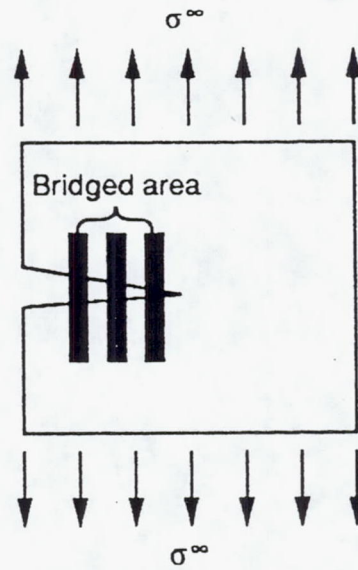
(a) Actual bridged crack.
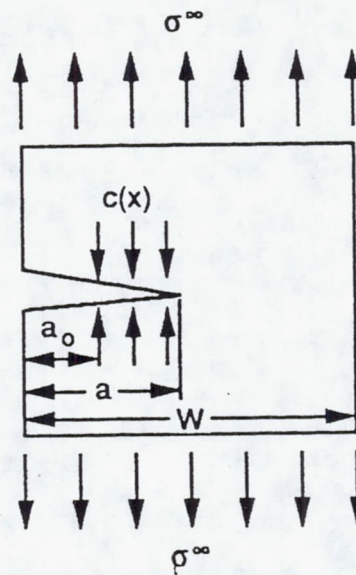
(b) Modeling of bridging
using a closure pressure.

Figure 3.10: Schematic of a partially-bridged single edge notch specimen with associated nomenclature.
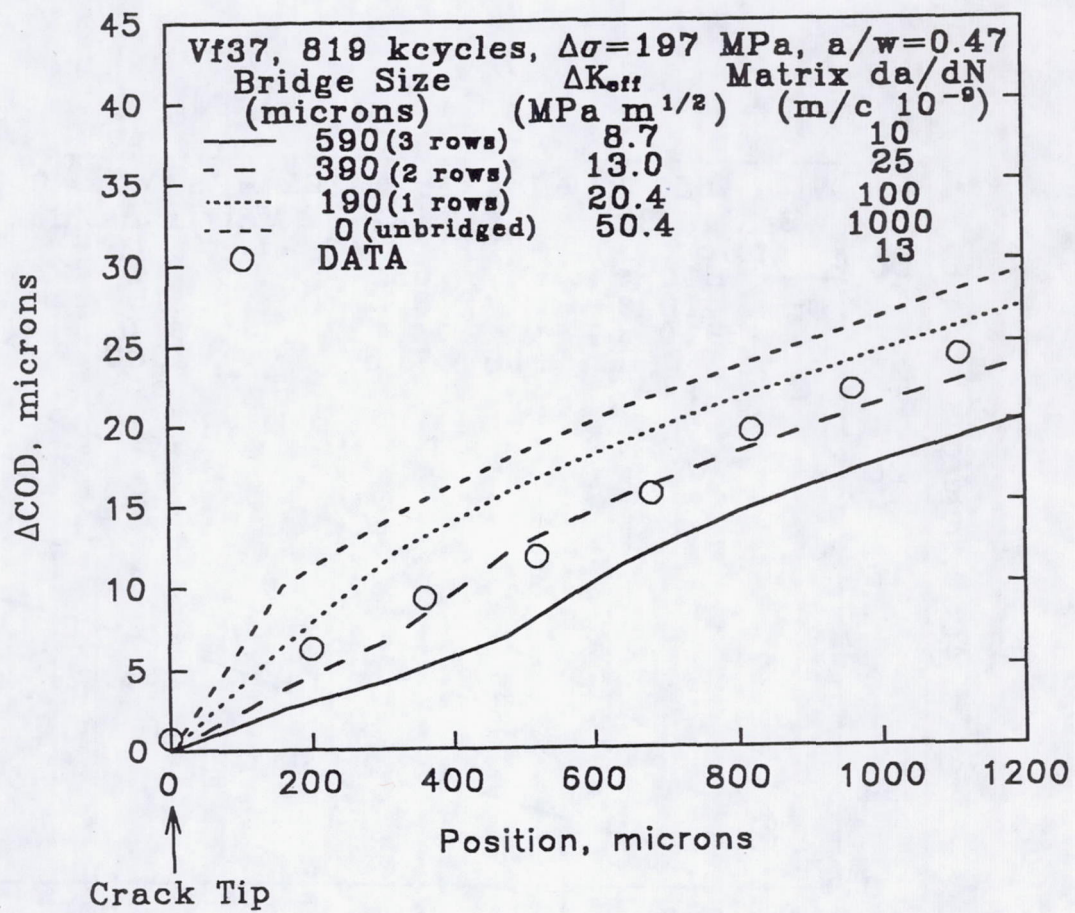
Figure 3.11: Post-arrest experimental ΔCOD vs position from the crack tip compared to fiber pressure model predictions for various bridged zone sizes. This method allows an estimation of the bridged zone size (about 400 microns) without interrupting the test.
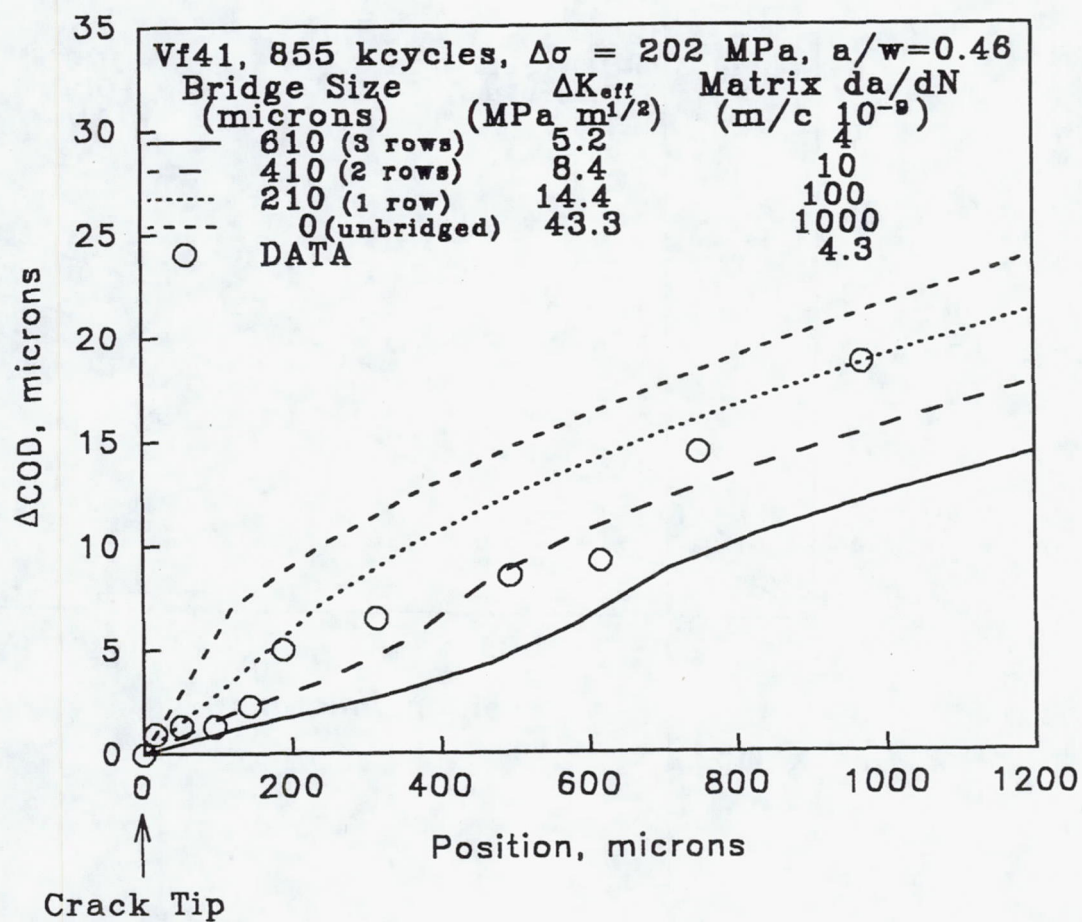
Figure 3.11: Continued

170
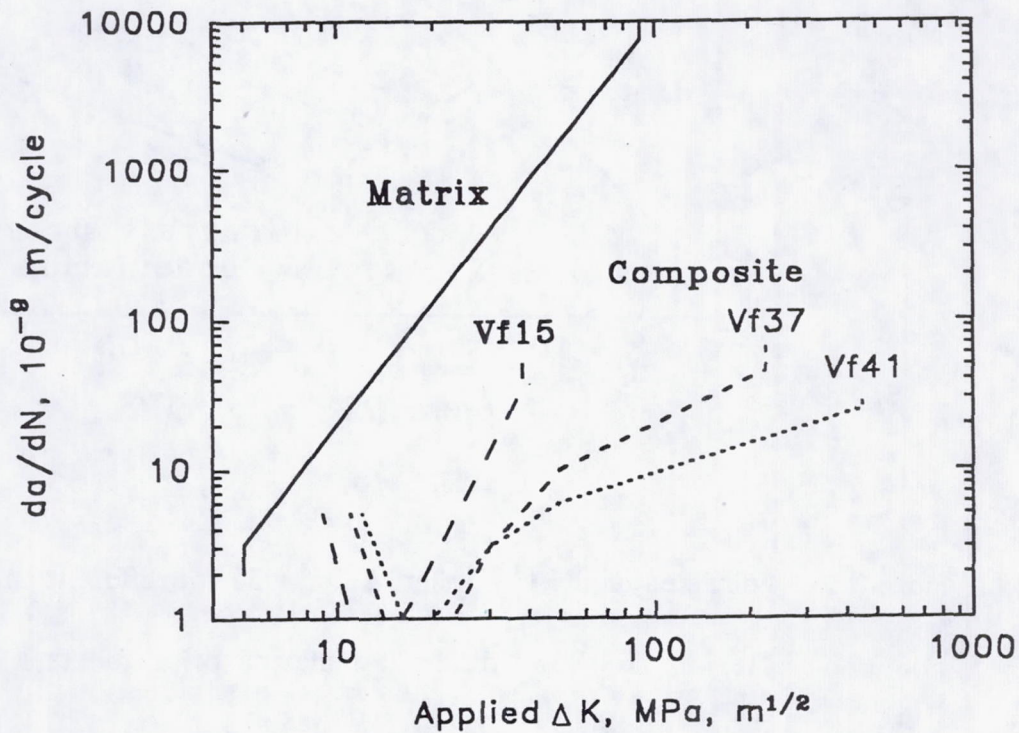
Figure 3.12: Idealized da/dN vs applied ΔK for each fiber volume fraction. Note the similar behavior prior to crack arrest but very different behavior after. The fatigue crack growth and toughness properties improve with increasing fiber volume fraction after crack arrest for these minimum stress levels.
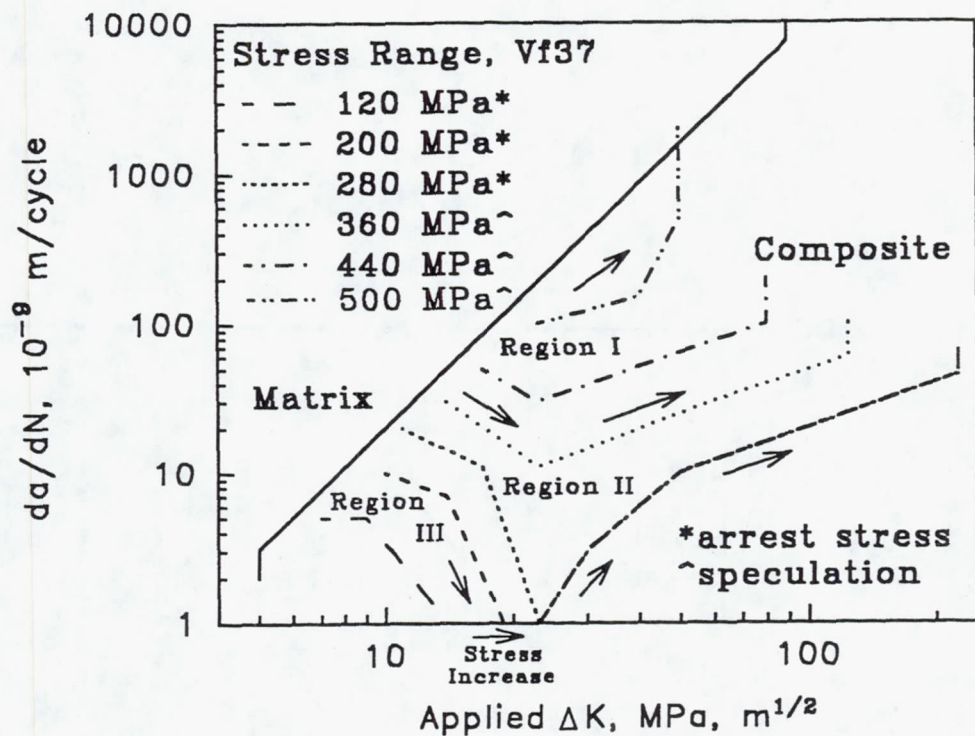
Figure 3.13: Idealized da/dN vs applied ΔK in vf37 for different stress ranges. Region III shows different behavior prior to crack arrest but identical behavior after, up to a maximum stress range of about 280 MPa. Regions II shows improved behavior over unreinforced matrix but no crack arrest because the higher applied stress breaks some of the bridged fibers. Region I occurs at a still higher applied stress level and shows properties significantly degraded from unreinforced matrix. Apparently, crack growth rates greater than 50×10^{-9} meters per cycle imply failure is imminent.

172
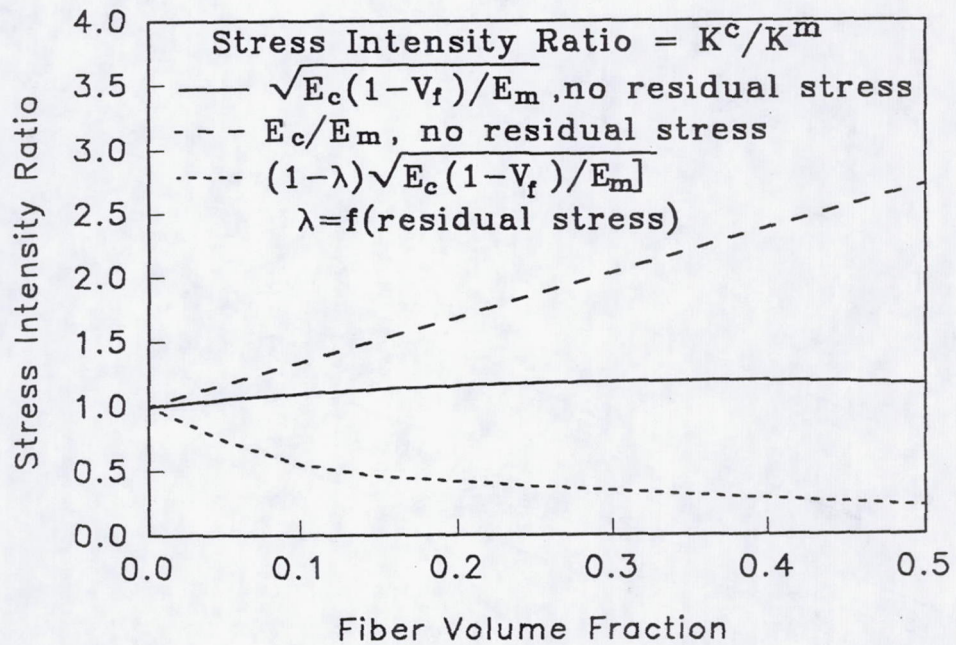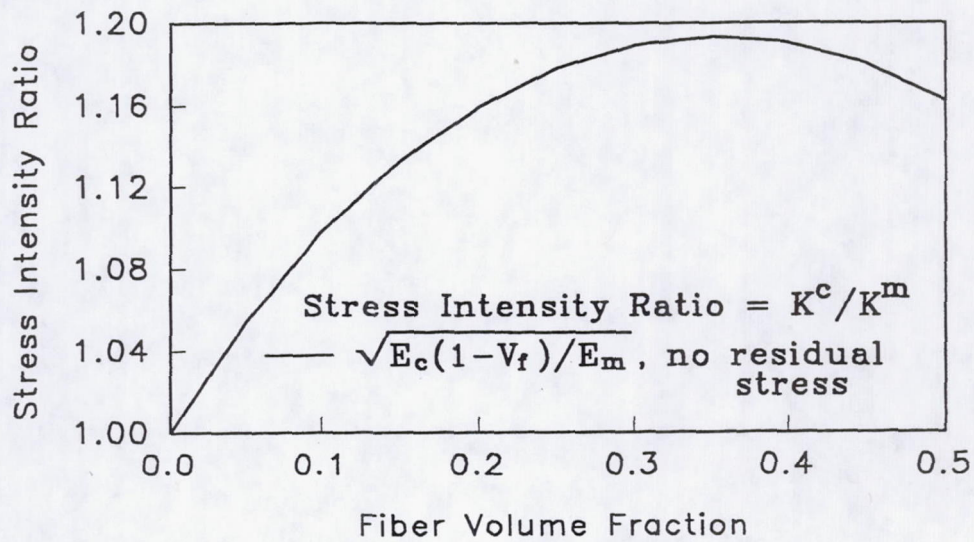
Figure 3.14: Ratio of composite to matrix stress intensity vs fiber volume fraction for three different models.
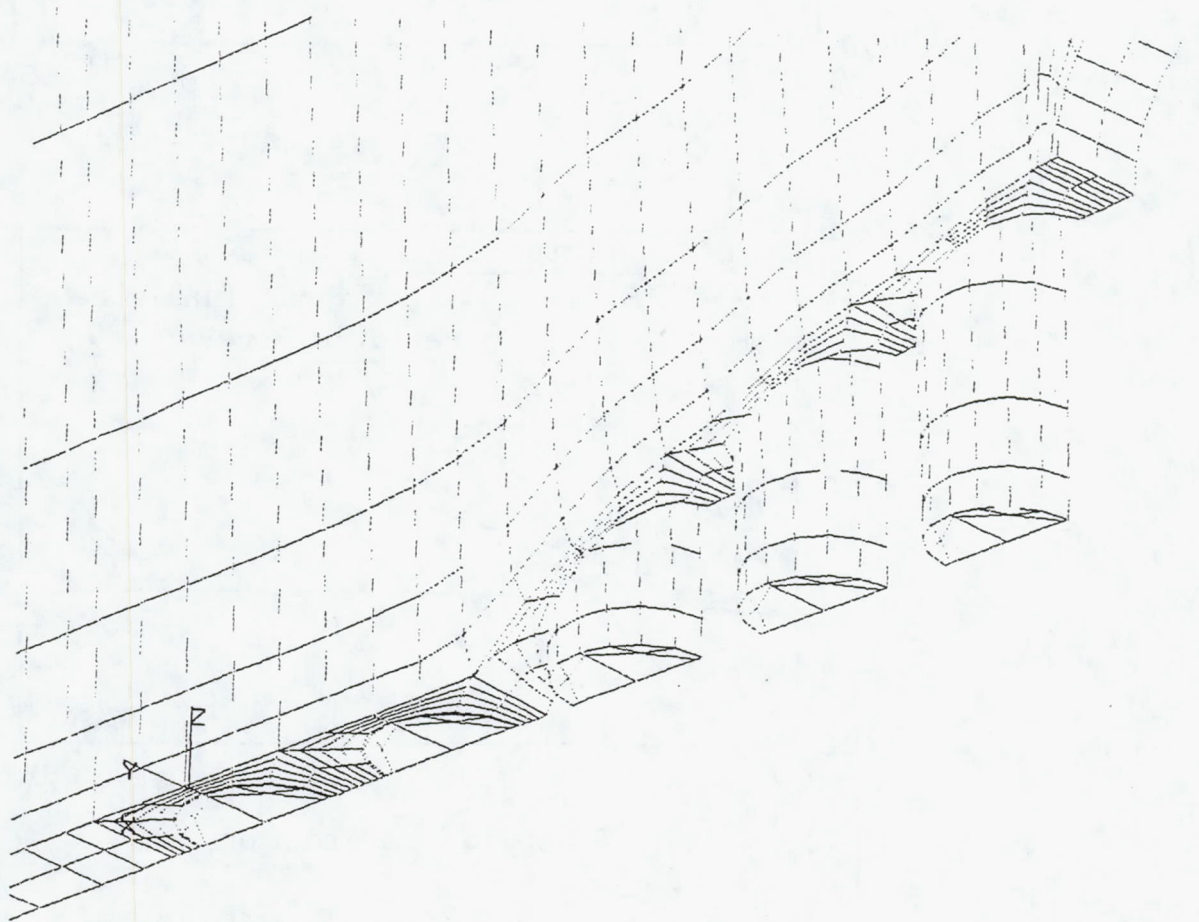
Figure 3.15: Finite element model of crack arrest shows bridged fibers.

174
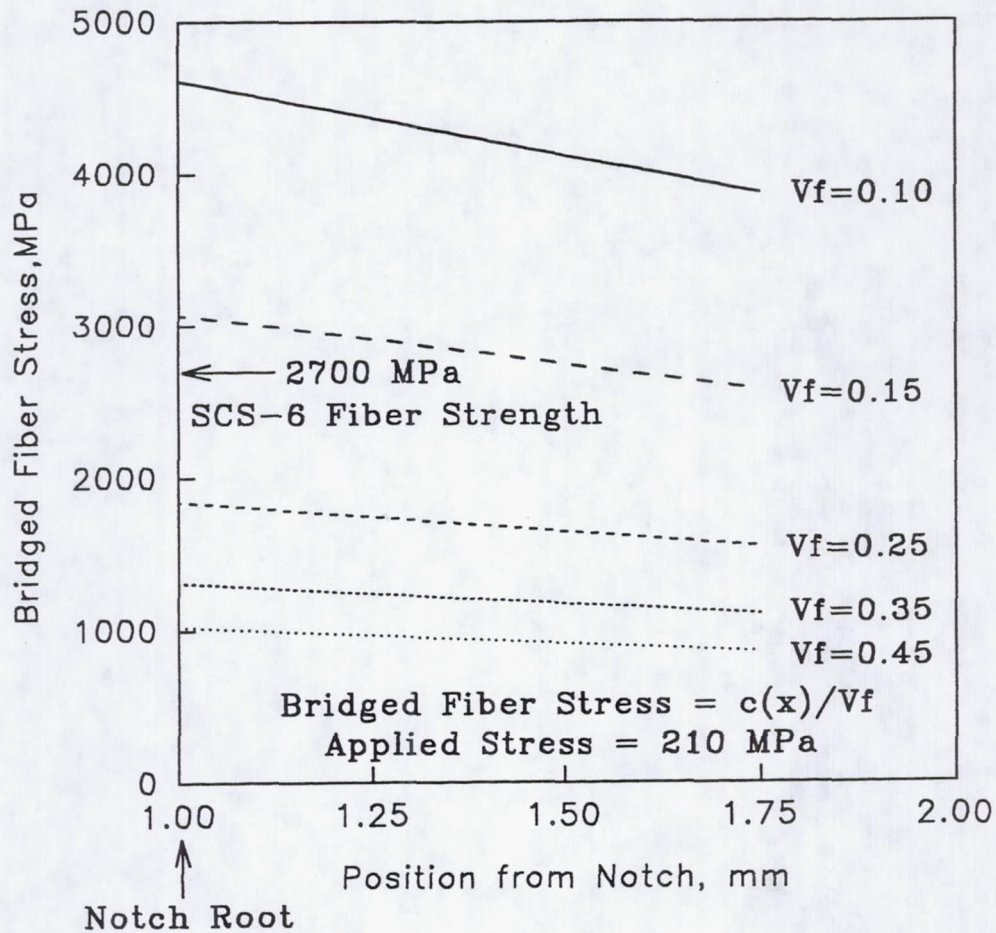
Figure 3.16: Fiber pressure model estimation of bridged fiber stress vs fiber volume fraction. Note that a fiber volume fraction of 0.15 is the minimum for which bridging can occur because the fibers break at lower fiber volumes. In-situ SCS-6 fiber strength data from Reference 6, 7.

Orthotropic — Matrix   Fiber
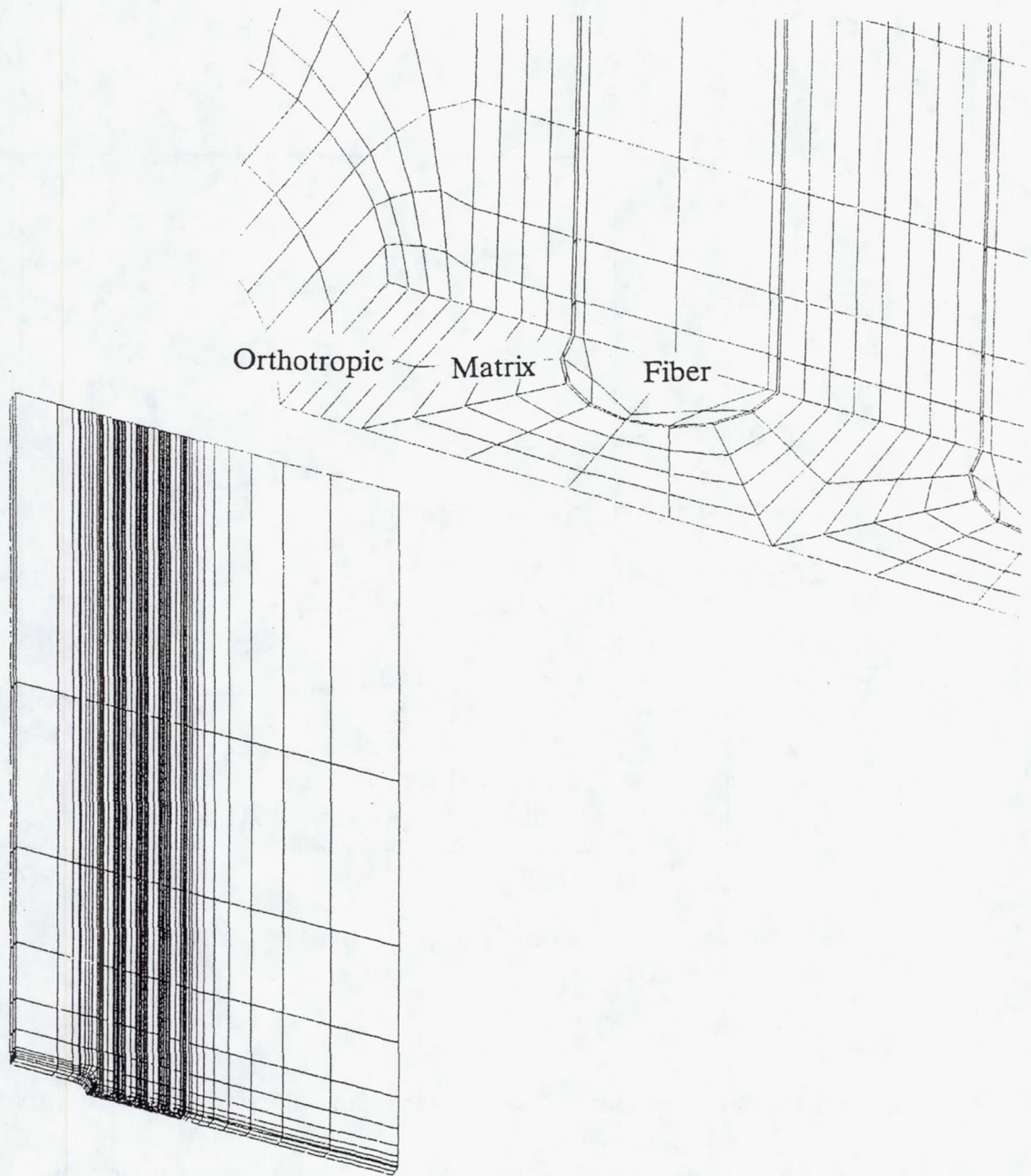
Figure 4.1:   Finite element mesh of the vf15 specimen. Note the discrete fiber

and matrix region ahead of the notch with orthotropic elements

used everywhere else.
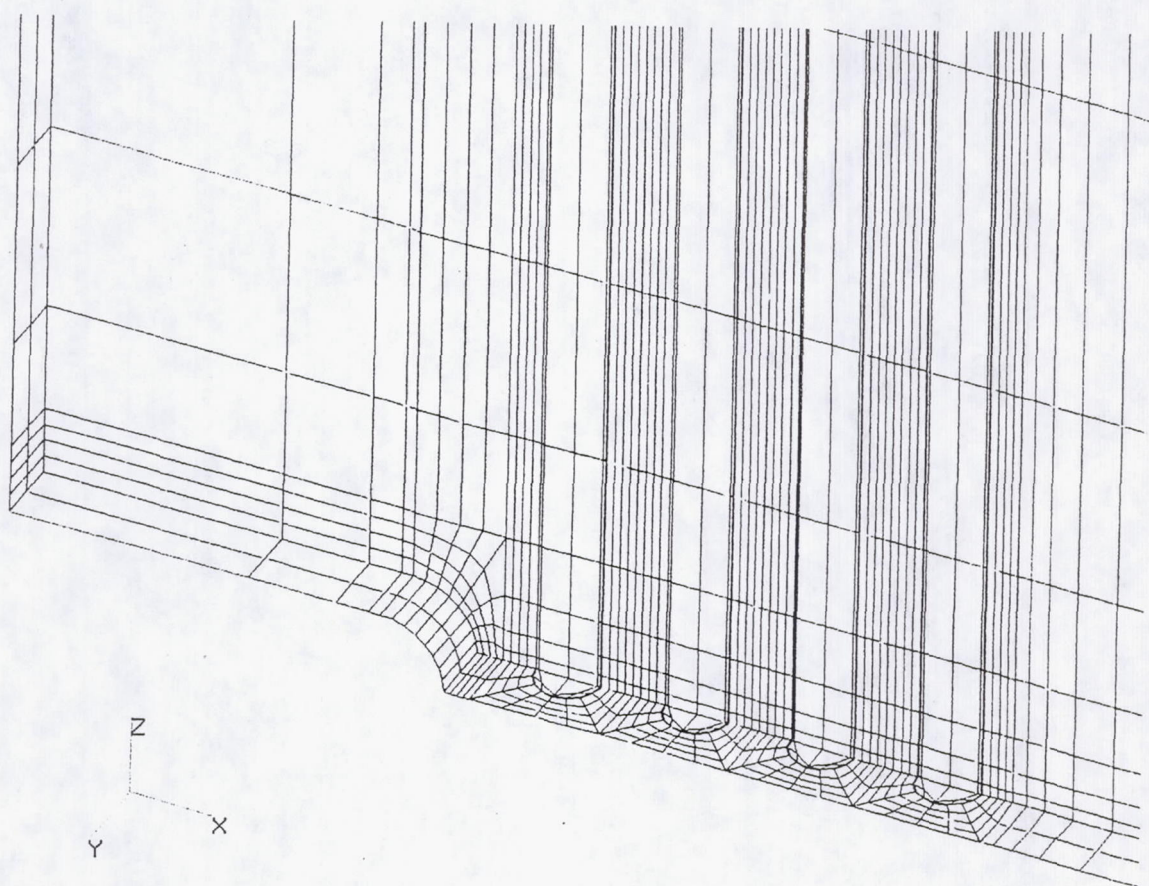
Figure 4.1: Continued

177
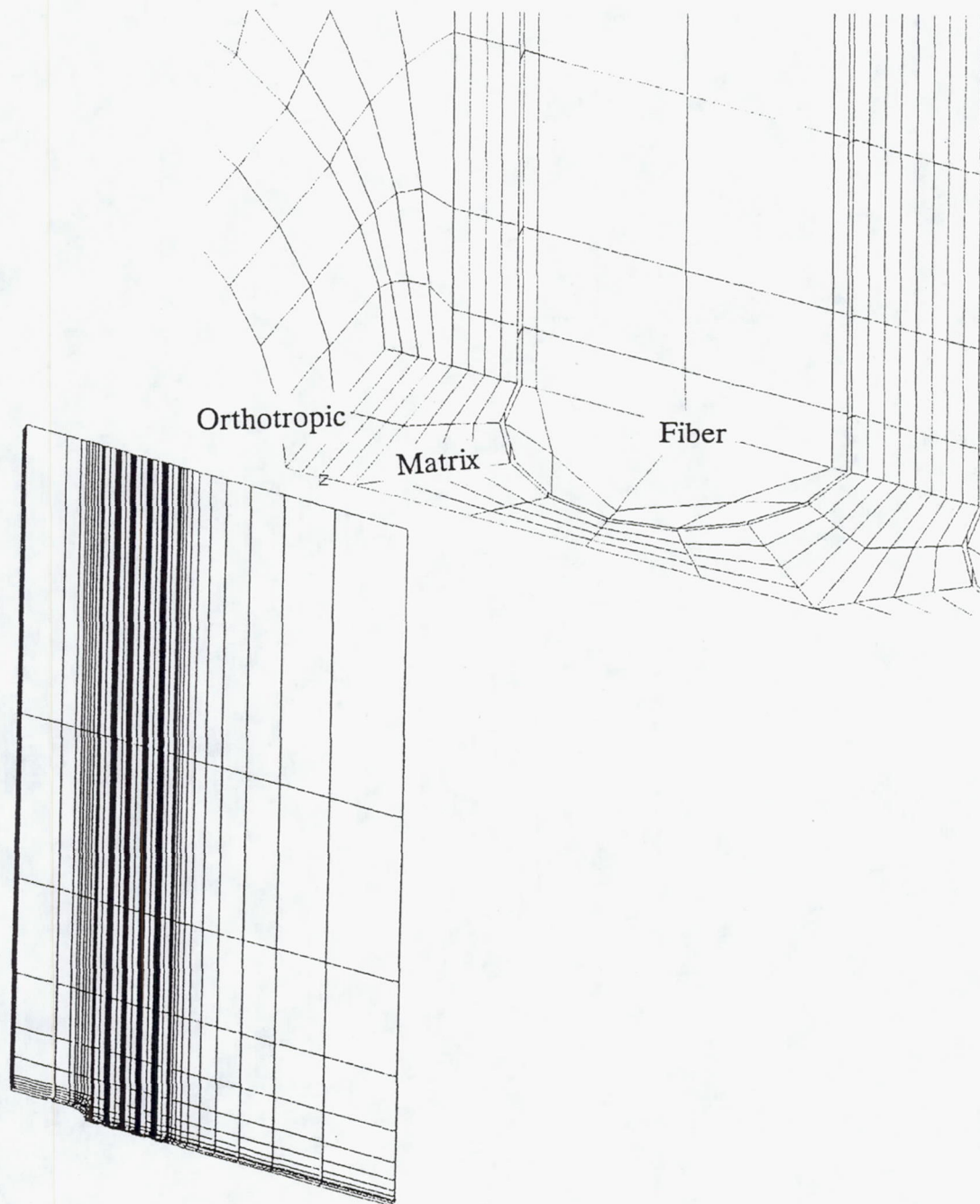
Figure 4.2: Finite element mesh of the vf37 specimen. Note the discrete fiber and matrix region ahead of the notch with orthotropic elements used everywhere else.

Figure 4.2: Continued

179

Applied Stress

Notch
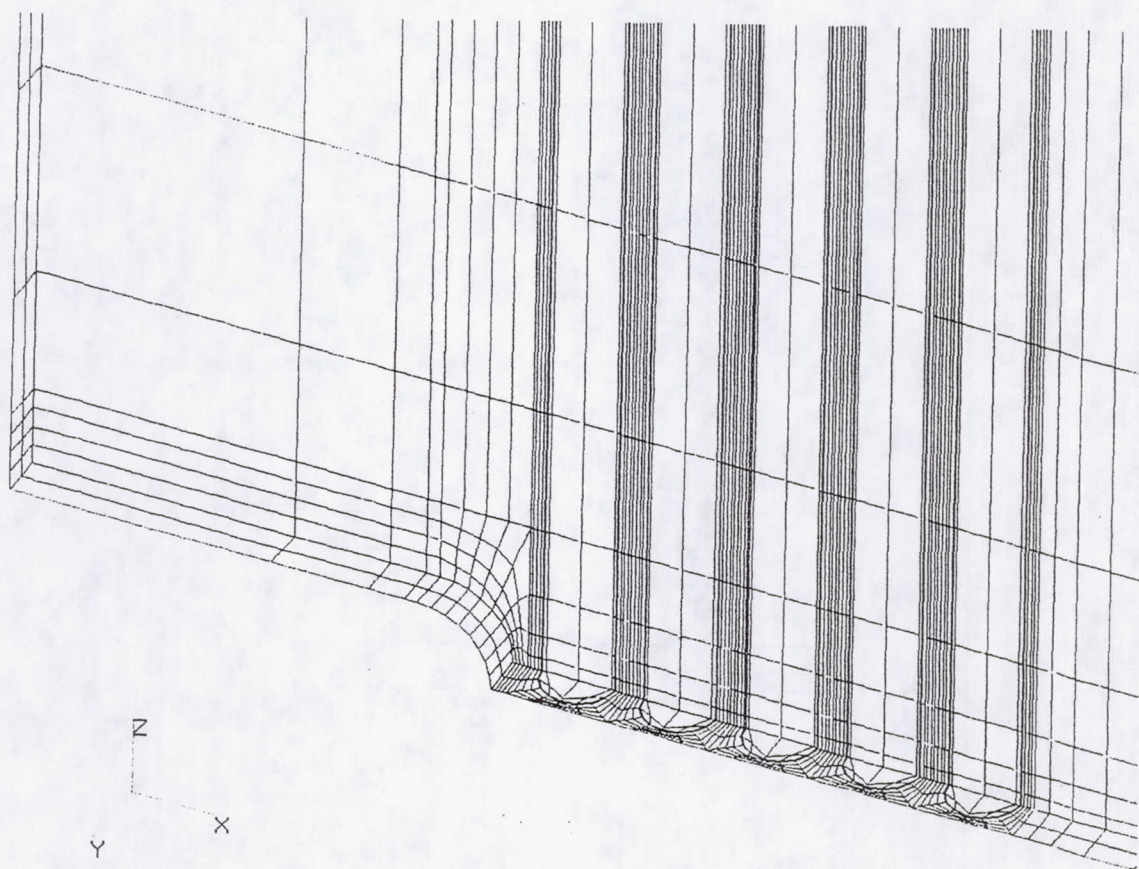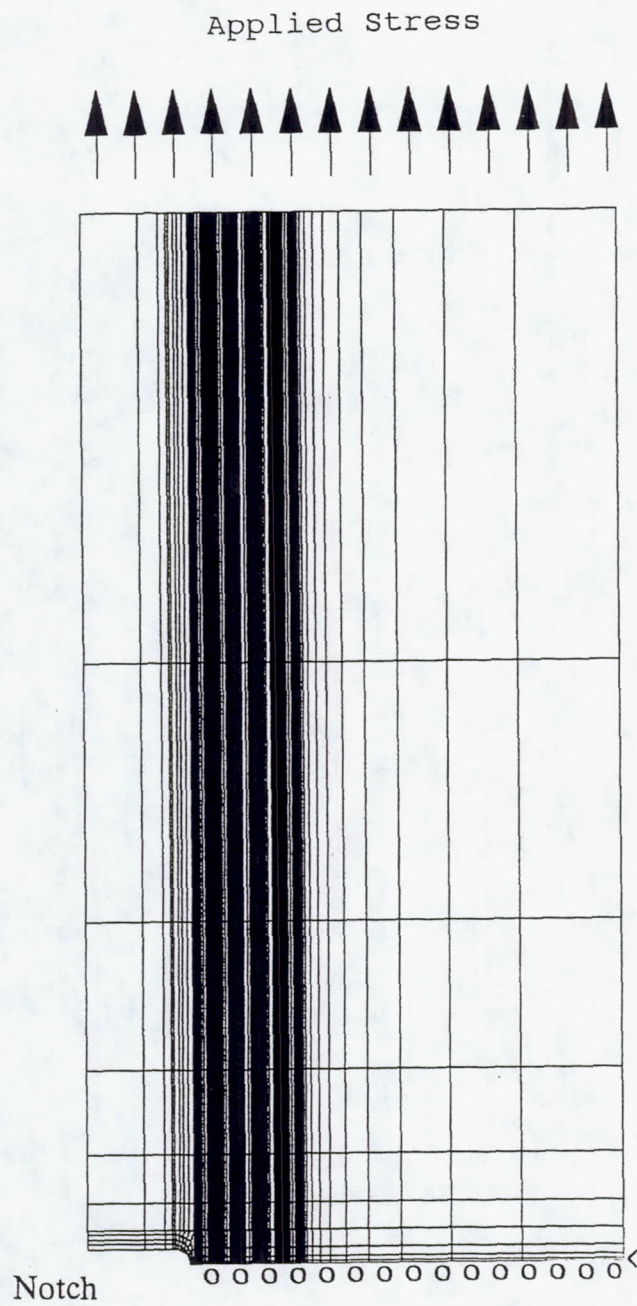
Figure 4.3: Sketch shows the finite element boundary conditions.

180

End of Debond

Vf15

End of Debond
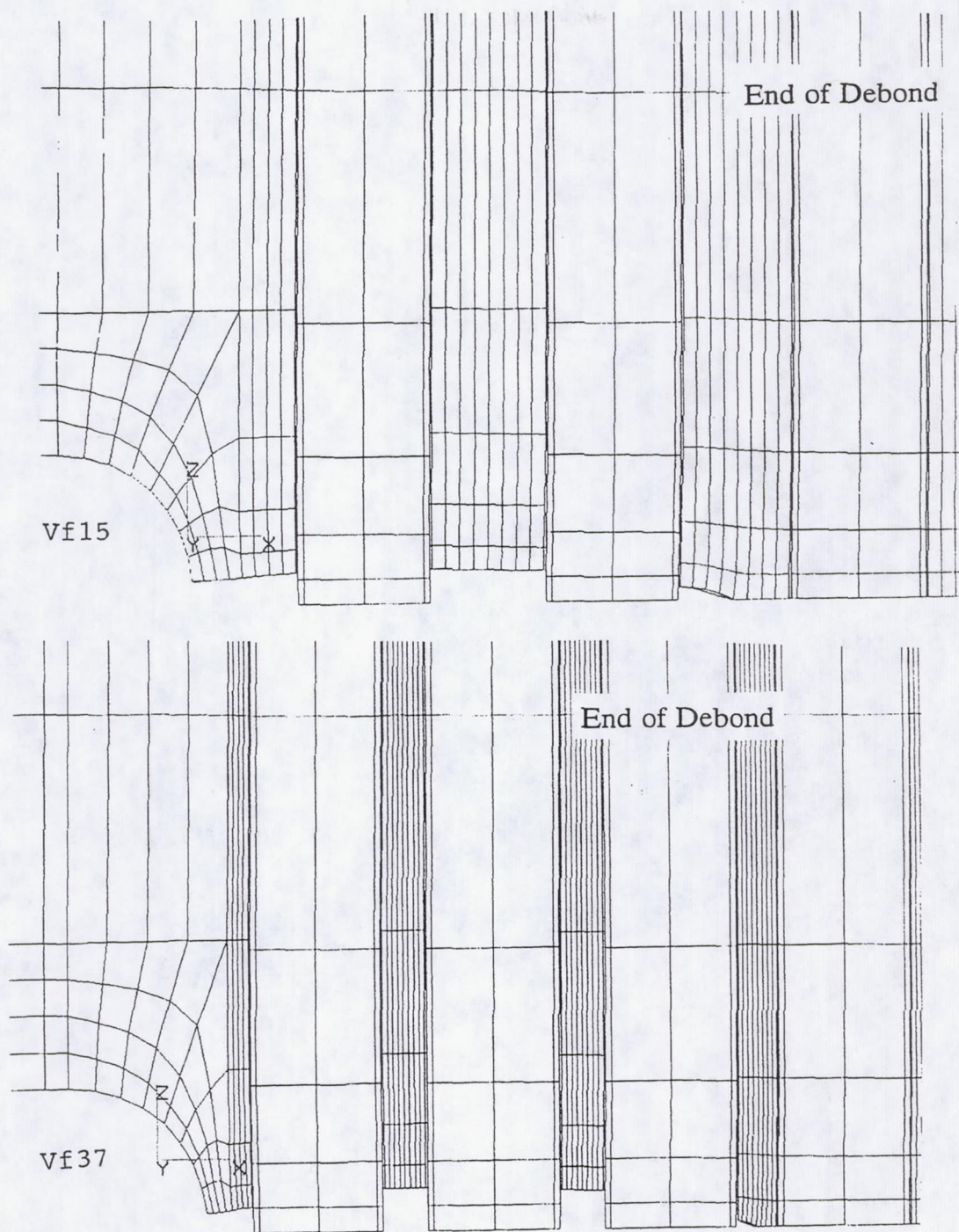
Vf37

Figure 4.4: Deformation profile of cracked matrix with residual stresses. Displacements have been magnified 25 times.

181
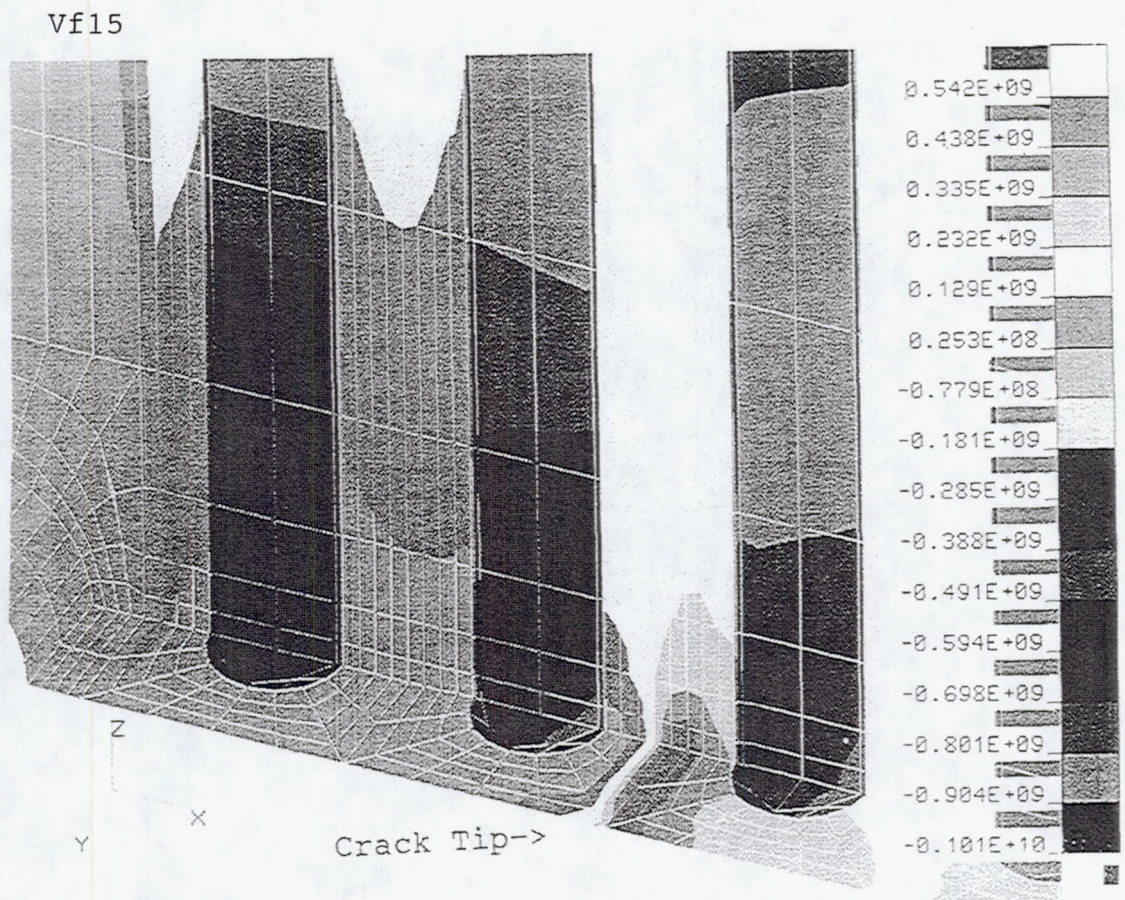
Figure 4.5: Longitudinal stress contour of cracked matrix with residual stresses. Units are in Pascals.

Vf37

Crack Tip->
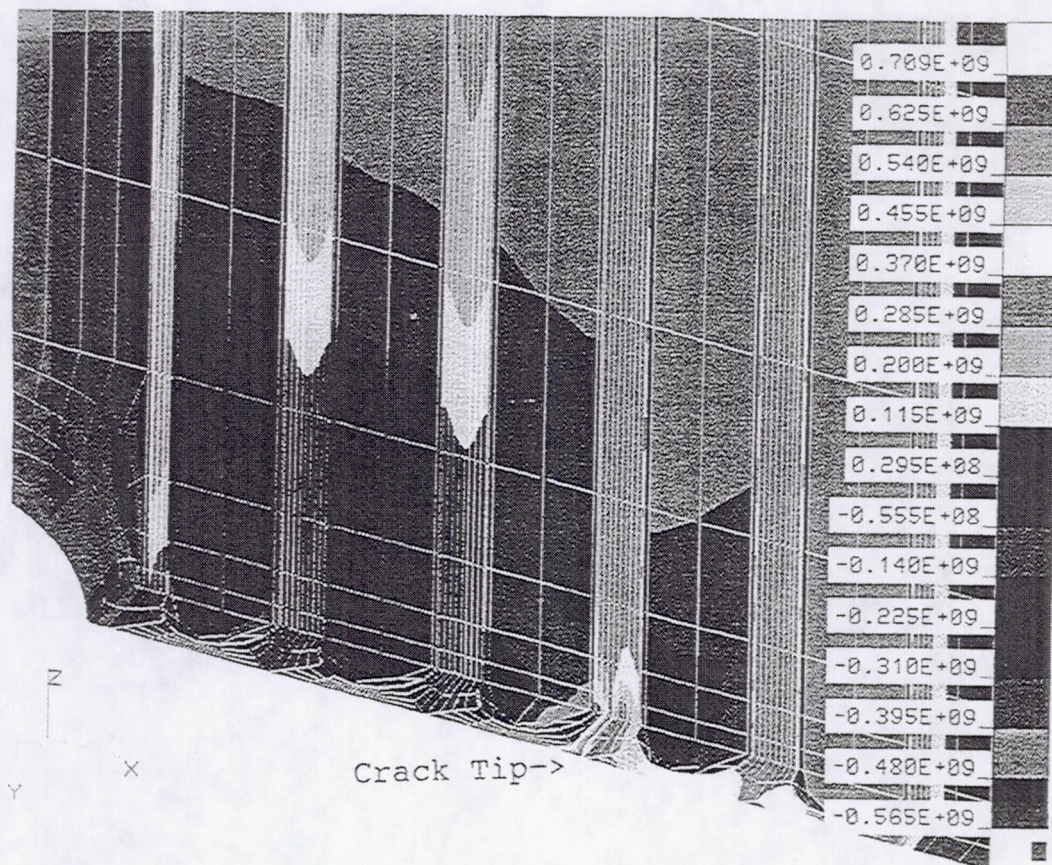
Figure 4.5: Continued
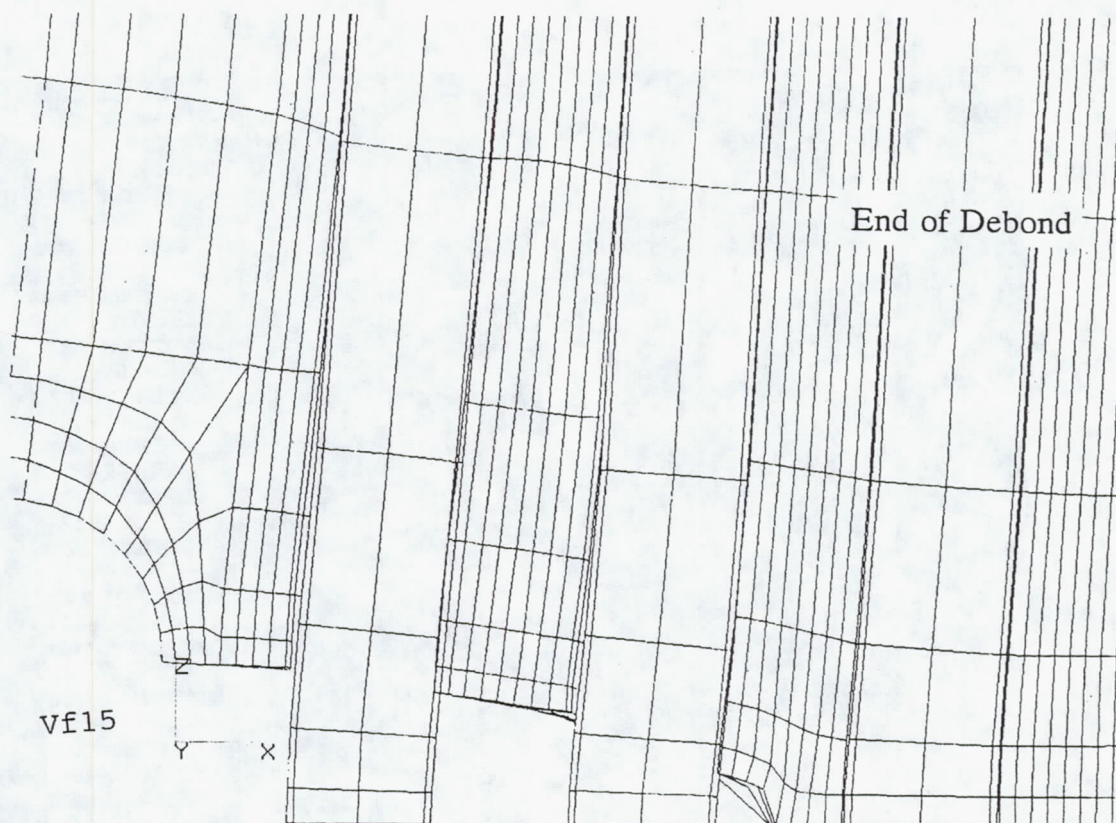
Figure 4.6:   Deformation profile of cracked matrix with residual stresses and

210 MPa applied stress. Displacements have been magnified 25 times.
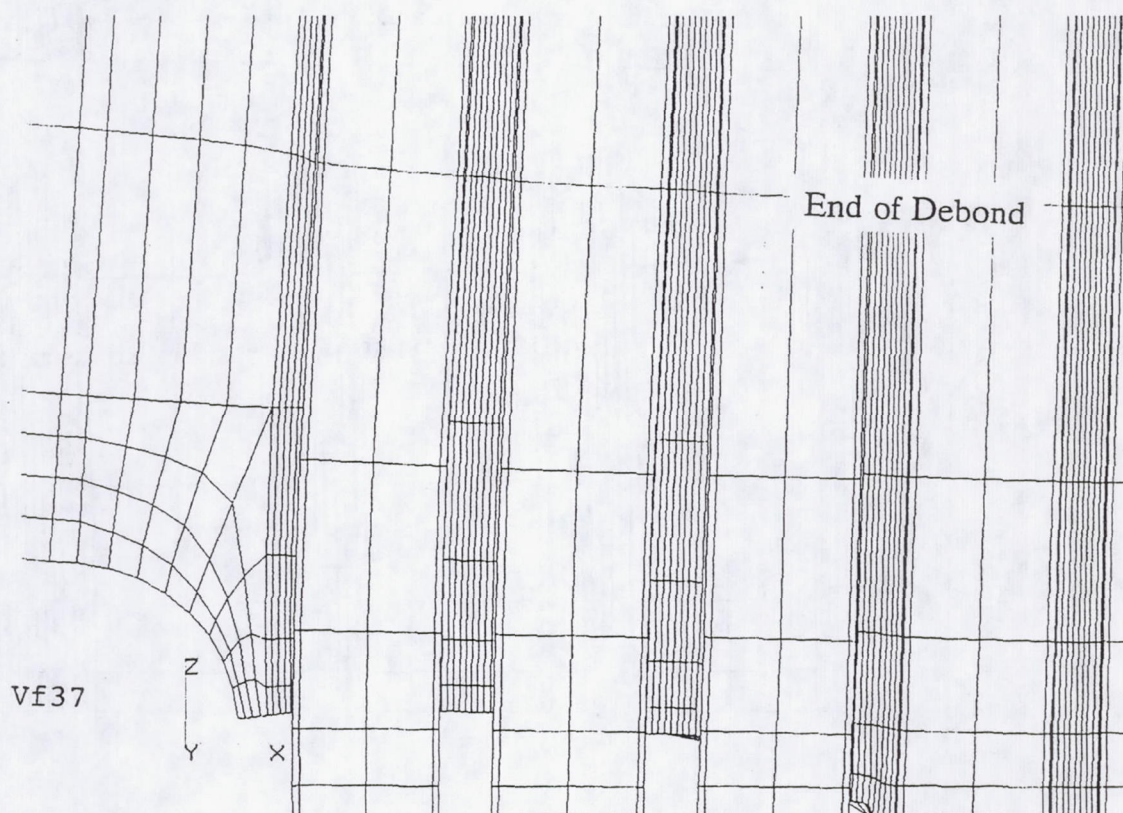
Figure 4.6: Continued

185
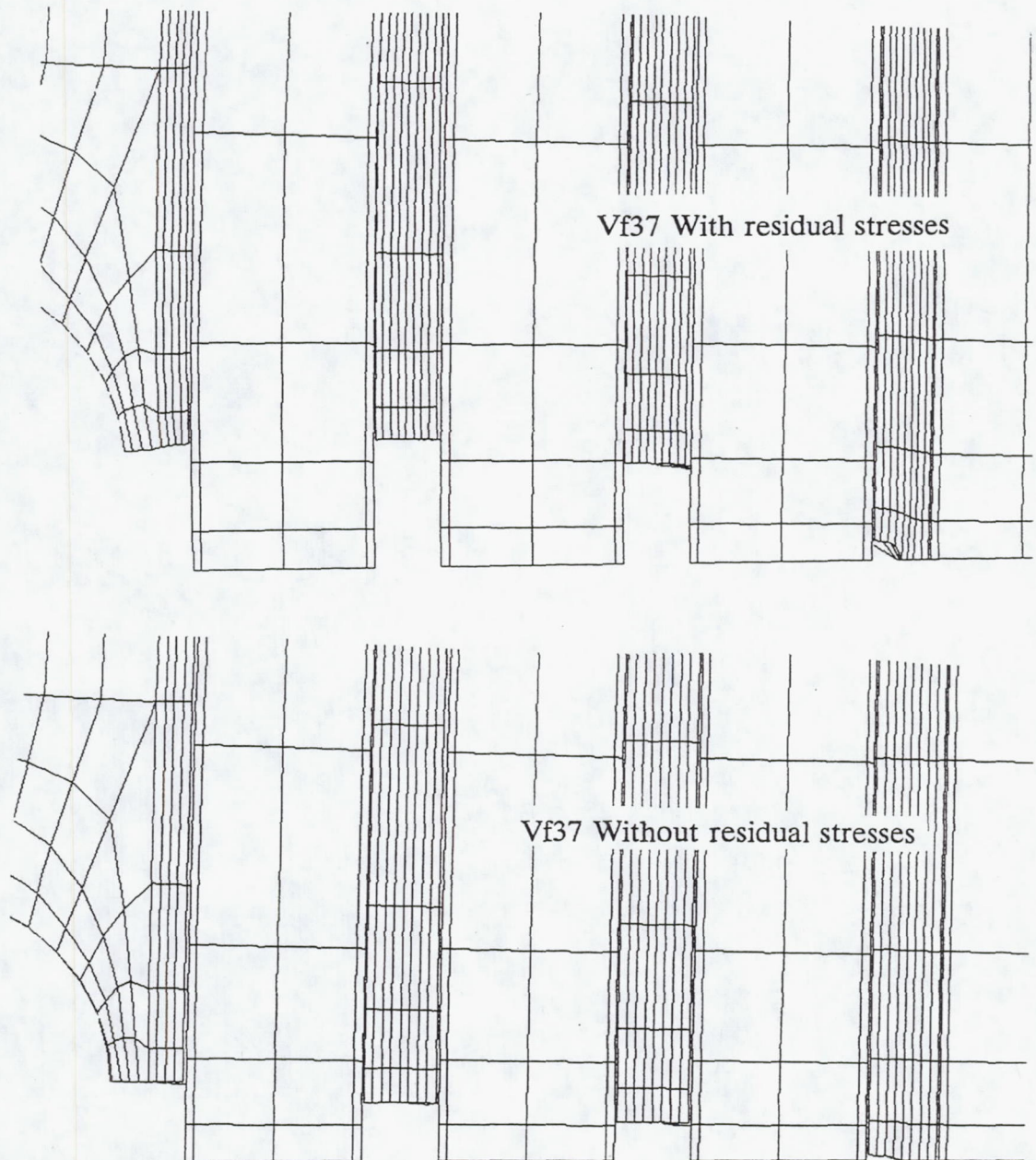
Figure 4.7: Deformation profile for vf37 of cracked matrix with a 210 MPa applied stress, with and without residuals. Displacements magnified 25 times.

Vf15
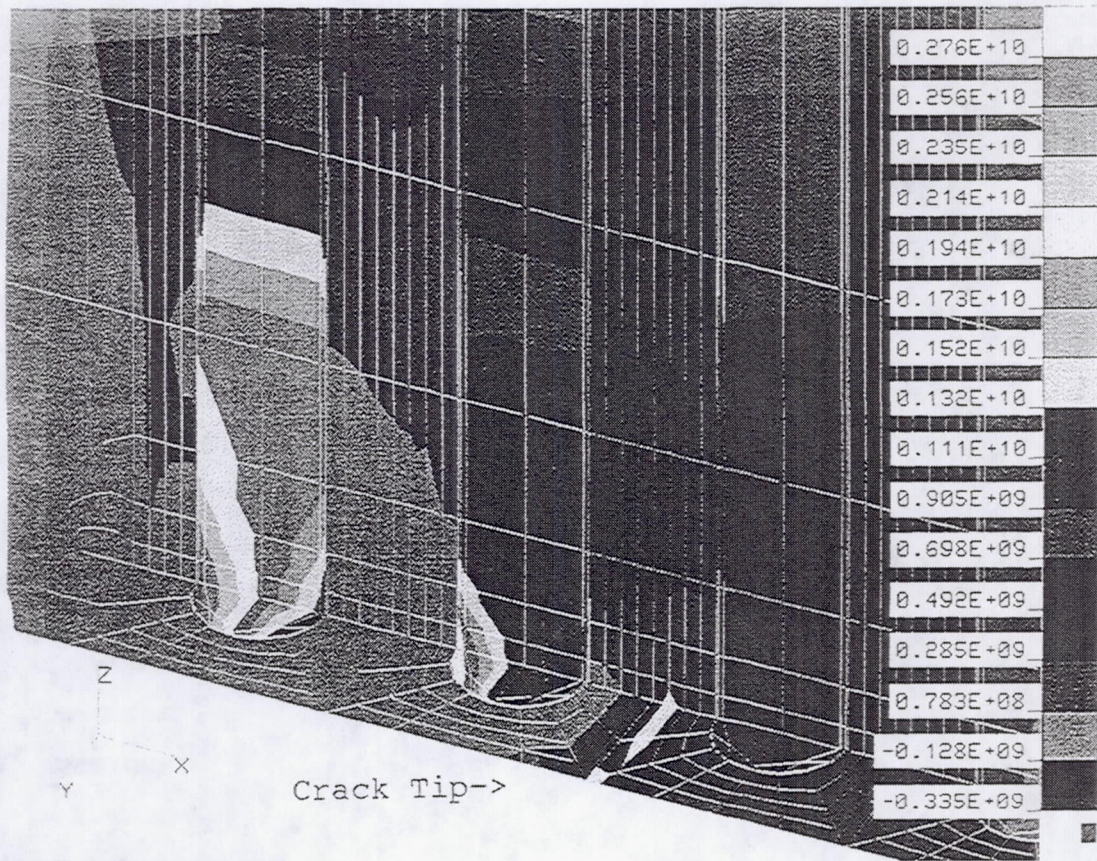
Figure 4.8:   Longitudinal stress contour of cracked matrix with residual stresses

and 210 MPa applied stress. Units are in Pascals.
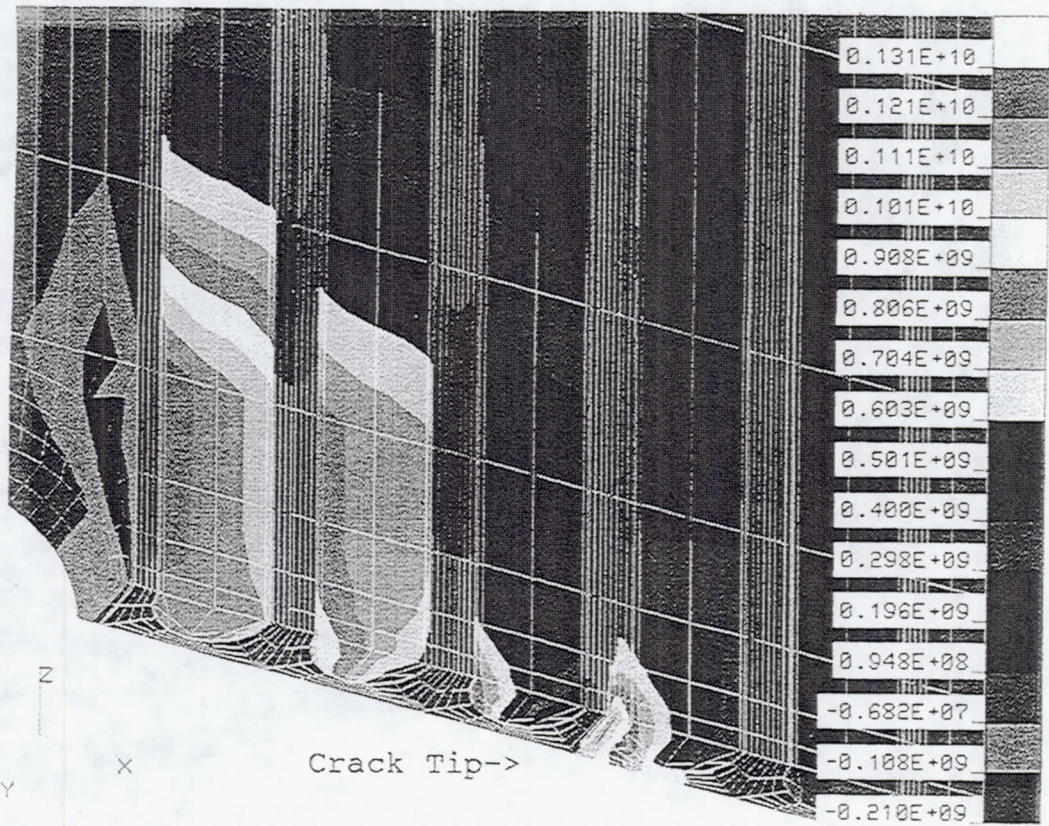
Vf37

Figure 4.8: Continued
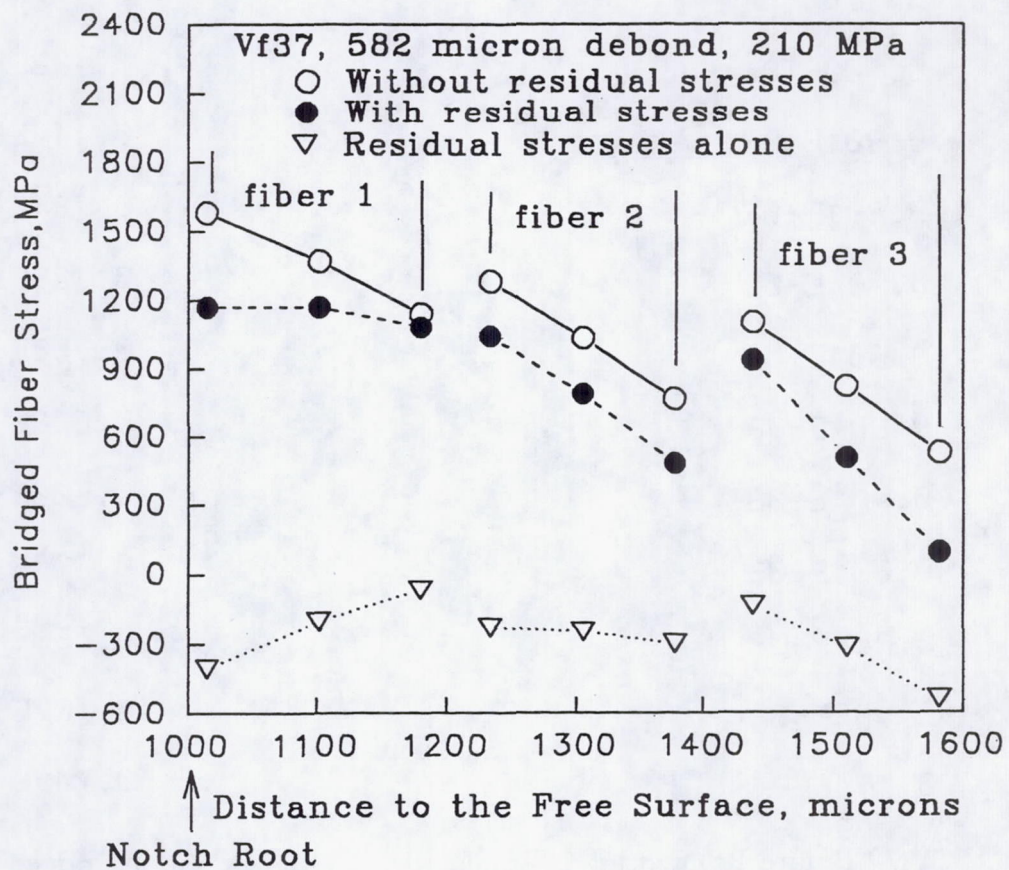
Figure 4.9: Bridged fiber stresses vs distance from the free surface with a 210

MPa applied stress with and without residual stresses.

0.150E-01	0.189E-01
0.140E-01	0.177E-01
0.130E-01	0.164E-01
0.120E-01	0.152E-01
0.110E-01	0.139E-01
0.100E-01	0.126E-01
0.901E-02	0.114E-01
0.801E-02	0.101E-01
0.701E-02	0.885E-02
0.601E-02	0.758E-02
0.501E-02	0.632E-02
0.401E-02	0.506E-02
0.301E-02	0.380E-02
0.202E-02	0.253E-02
0.102E-02	0.127E-02
0.174E-04	0.748E-05
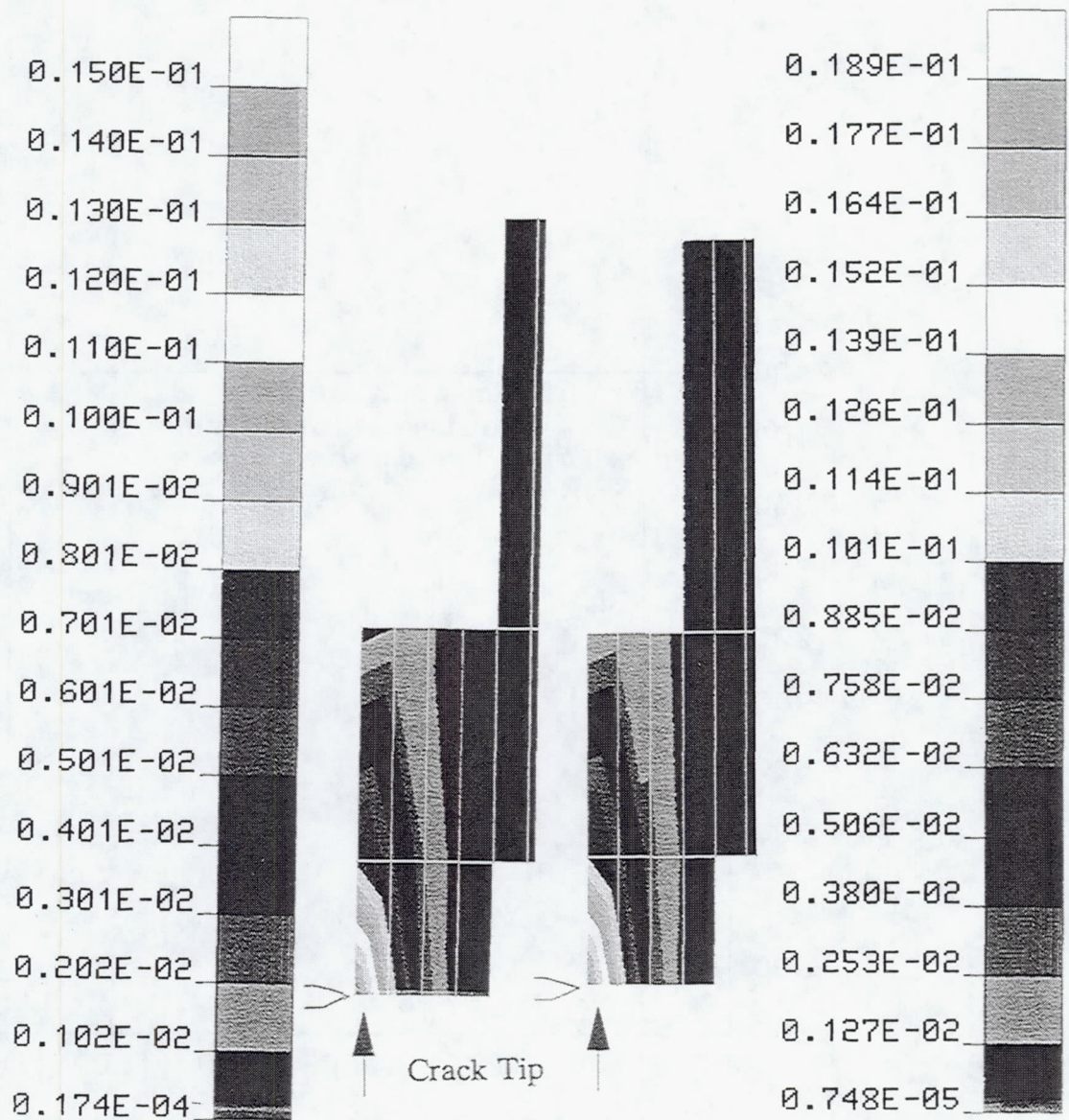
Crack Tip

Vf37 Before Bridged Fiber Break   Vf37 After Bridged Fiber Break

Figure 4.10: Effective matrix plastic strain contours near the crack tip in Vf37 for a 210 MPa applied stress with residual stresses before and after breaking bridged fibers. Note that even though the plastic zone size is similar, the strain magnitude increases by 25% after the fibers break.

190
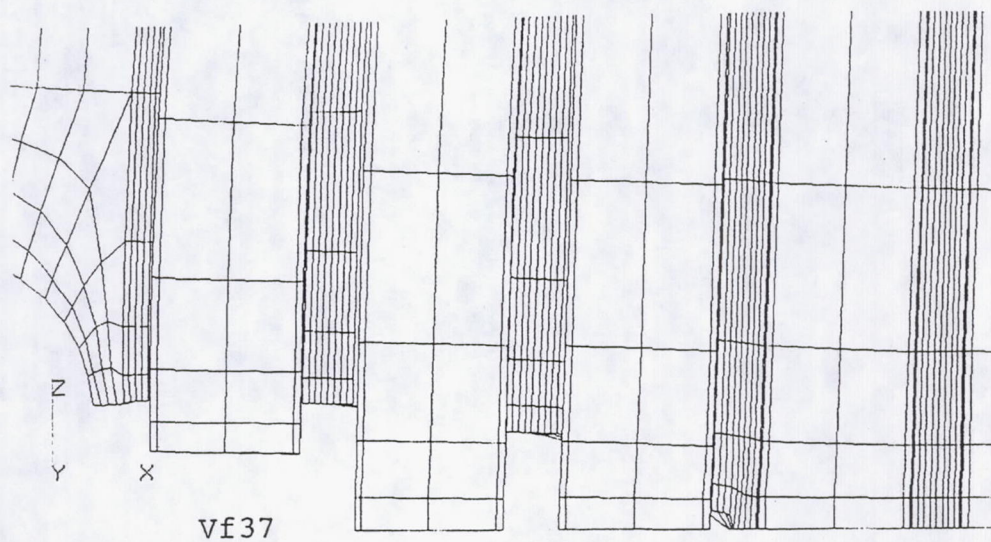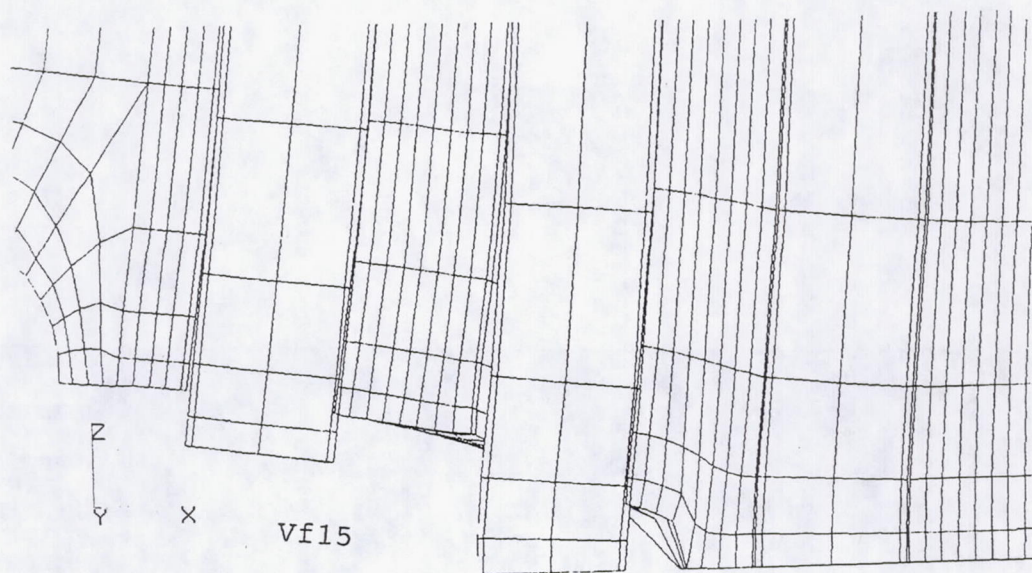
Figure 4.11: Deformation profile of cracked matrix with residuals, 210 MPa applied stress, and a broken bridged fiber. Displacements magnified 25 times.
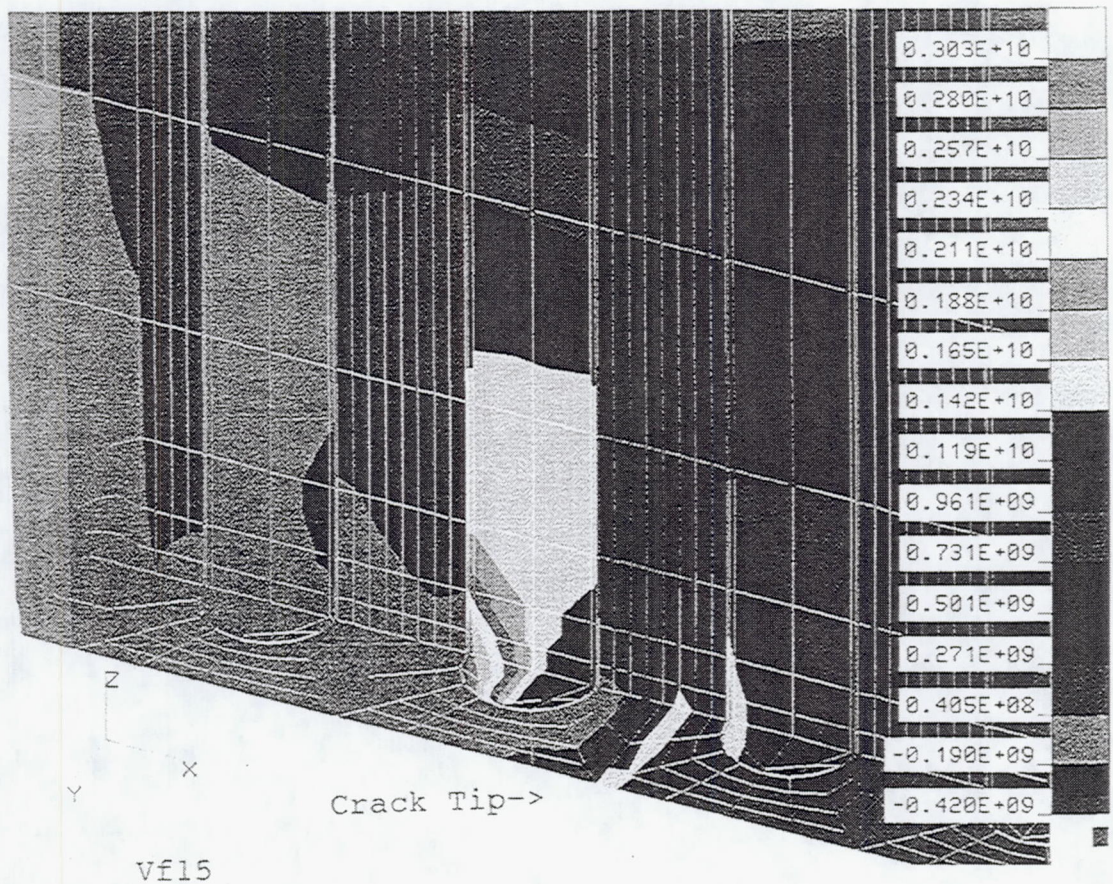
Figure 4.12: Longitudinal stress contour of cracked matrix with residual stresses, 210 MPa applied stress, and a broken bridged fiber. Units are in Pascals.

	0.151E+10
	0.140E+10
	0.128E+10
	0.117E+10
	0.105E+10
	0.939E+09
	0.825E+09
	0.710E+09
	0.596E+09
	0.482E+09
	0.368E+09
	0.254E+09
	0.140E+09
	0.258E+08
	-0.883E+08
	-0.202E+09

Crack Tip->
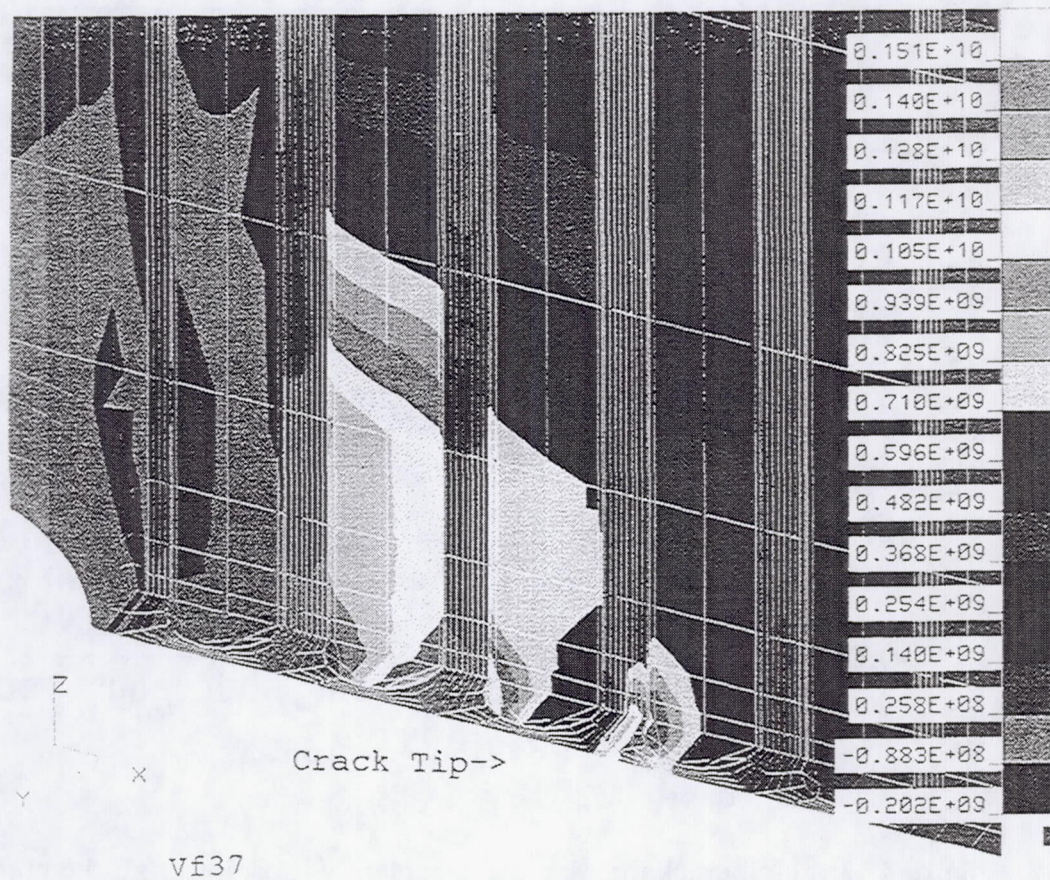
Vf37

Figure 4.12: Continued

193

Finite Element Applied Stress = 210 MPa

———vf37, 317 micron debond
– – –vf37, 582 micron debond
·····vf37, 582 micron debond w/broken fiber
········vf37, 1000 micron debond
········vf15, 582 micron debond
·–··–vf15, 582 micron debond w/broken fiber
○ Data, vf41#3, fully bridged, scaled
(COD*210/344)

● Data, vf15#2, broken fibers
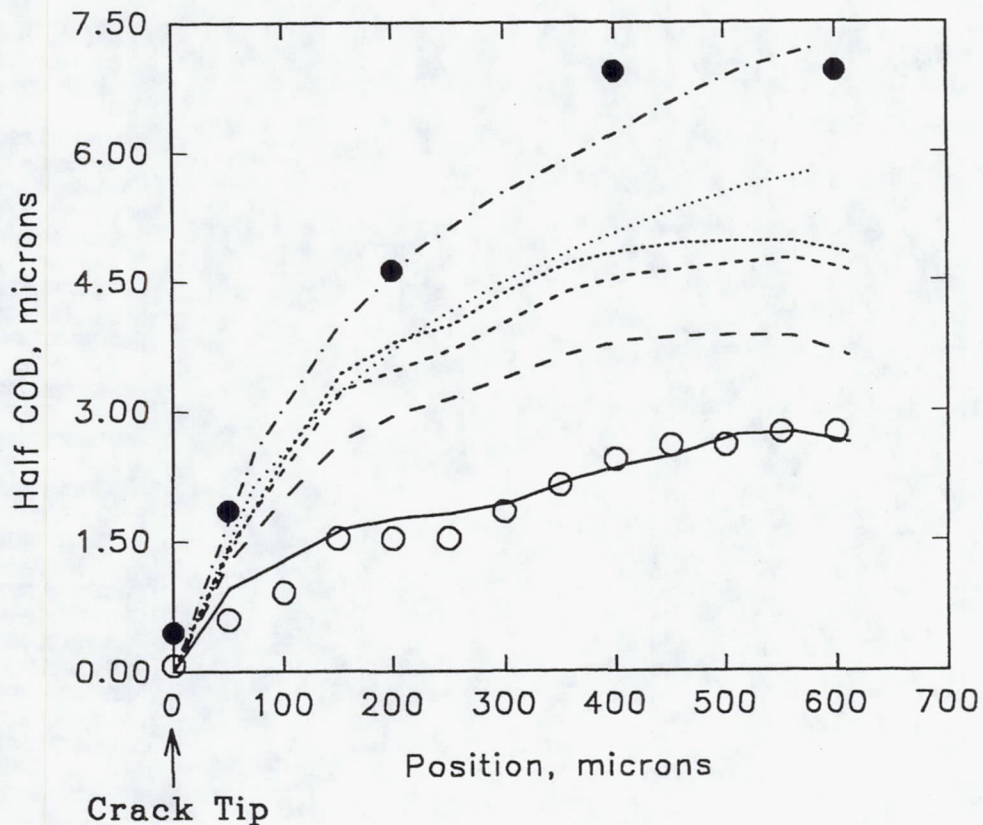
Figure 4.13: Half crack opening displacement vs position from the crack tip for

different fiber volume fractions, effective debond lengths, and fiber

bridging status. All curves include residual stress effects.

194
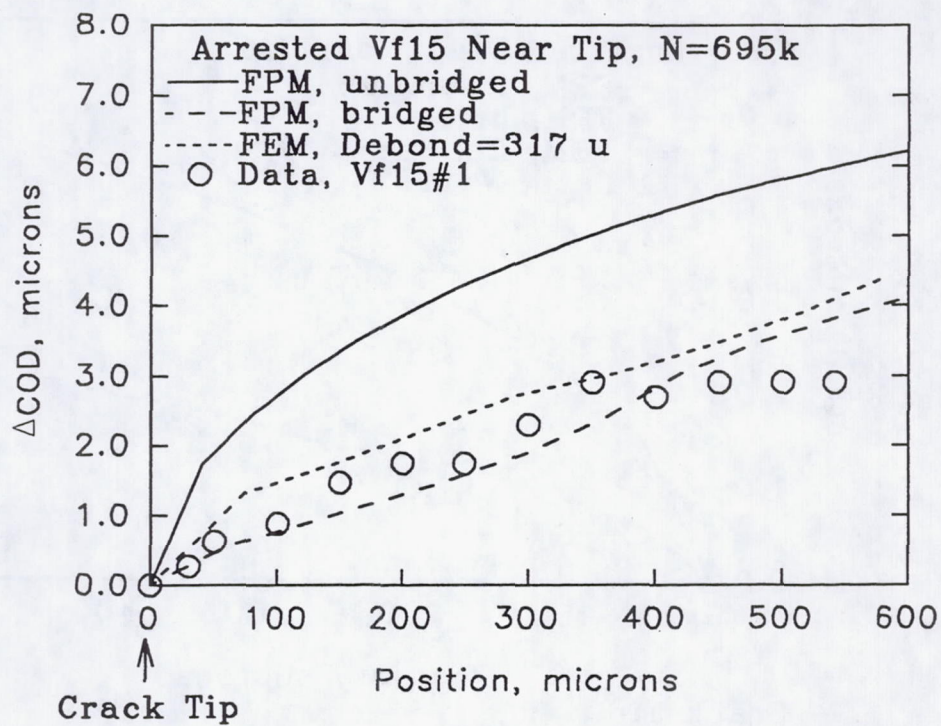
Figure 4.14: Delta COD vs position from the crack tip for current FEM models with an effective debond length of 317 microns compared to experimental data and the fiber pressure model.
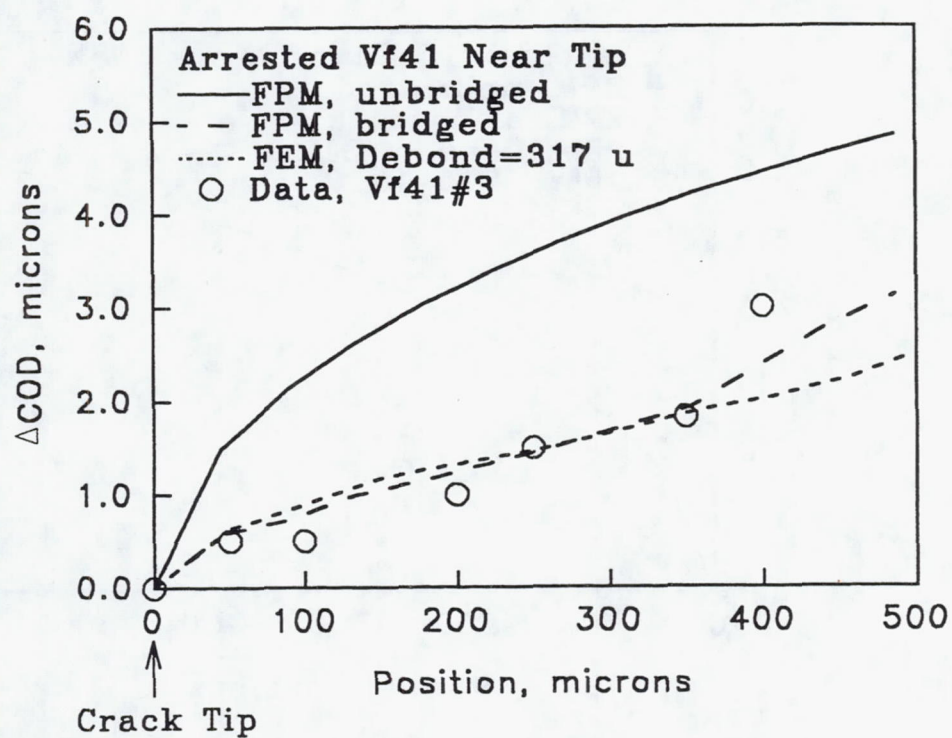
Figure 4.14: Continued

196
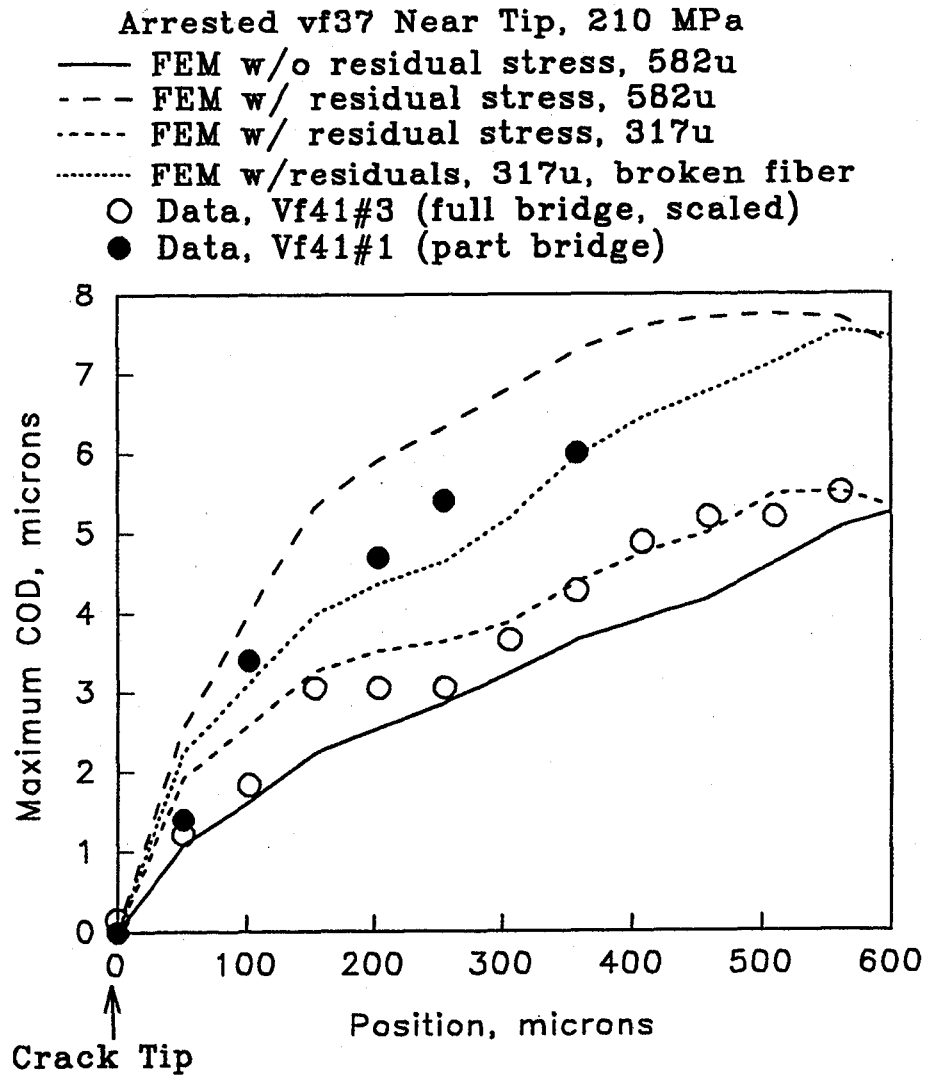
Figure 4.15: Maximum total crack opening displacements for vf37 with and without residual stresses compared to data.

Vf37, FEM, fully bridged

———	0 MPa, 317u debond
– – –	42 MPa, 317u debond
- - - -	0 MPa, 582u debond
··········	42 MPa, 582u debond
·········	210 MPa, 317u debond
·—·—·	210 MPa, 582u debond
O	Data, 35 MPa, vf41#3
●	Data, 210 MPa, vf41#3, scaled (COD*210MPa/344MPa)
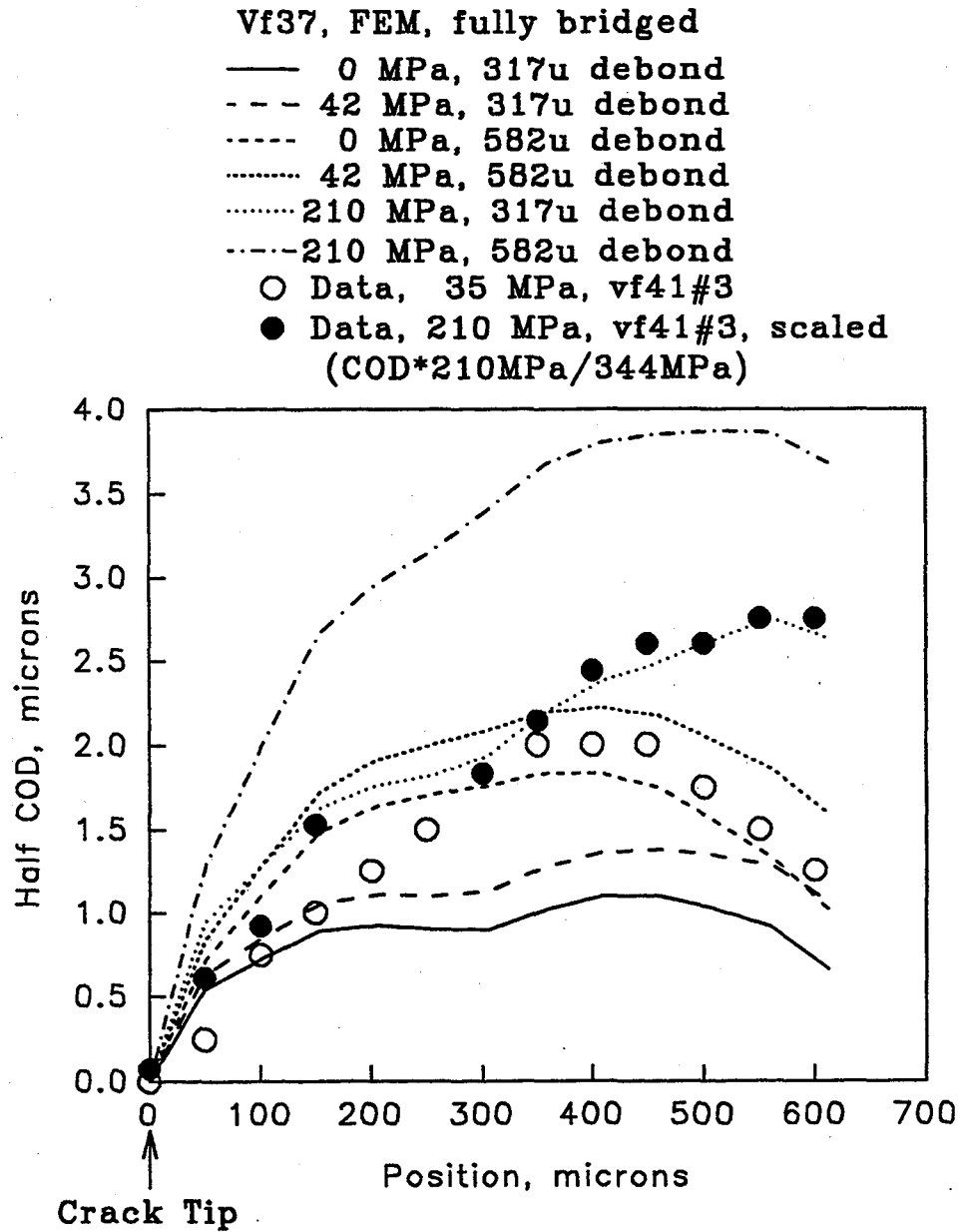
Figure 4.16: FEM predicted half COD profile for maximum and minimum applied stresses with experimental data.
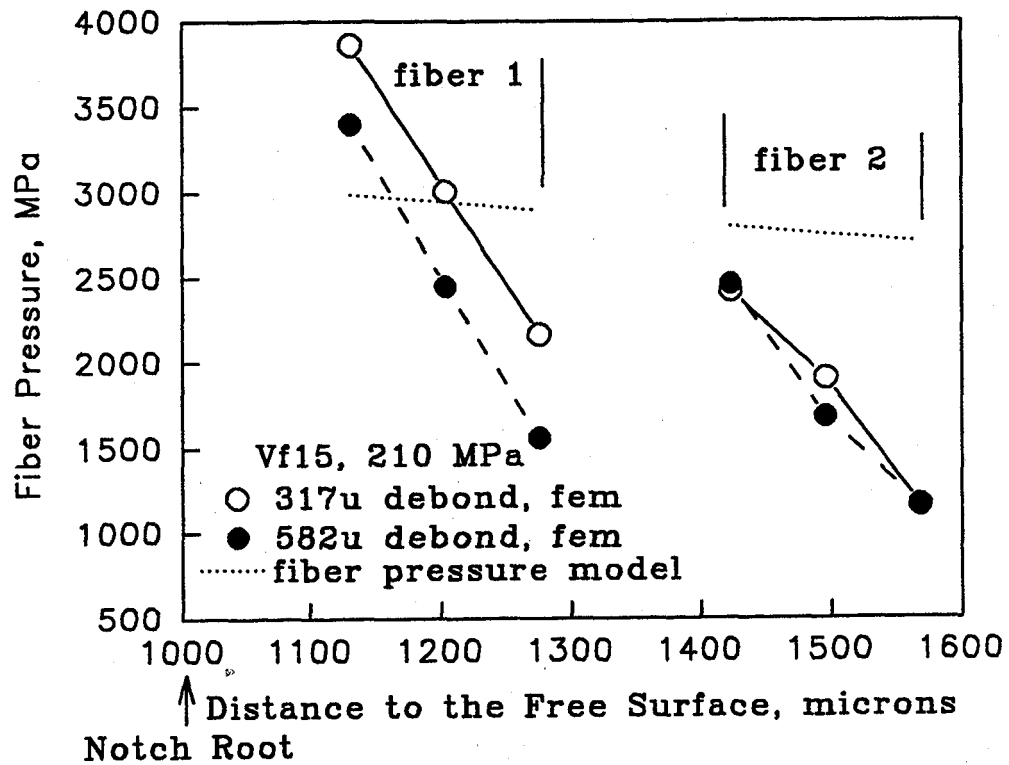
Figure 4.17: Fiber pressure distribution vs position from the free surface with residual stresses and an applied stress of 210 MPa. The fiber pressure is the sum of the fiber stress and the magnitude of the fiber residuals.

199
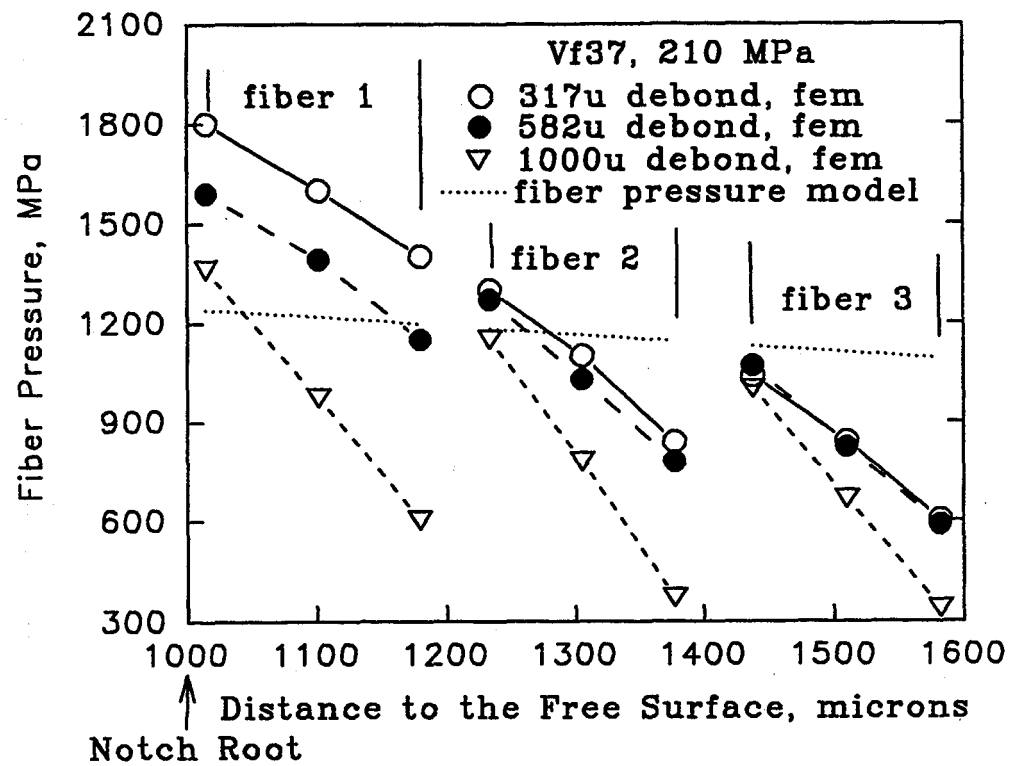
Figure 4.17: Continued
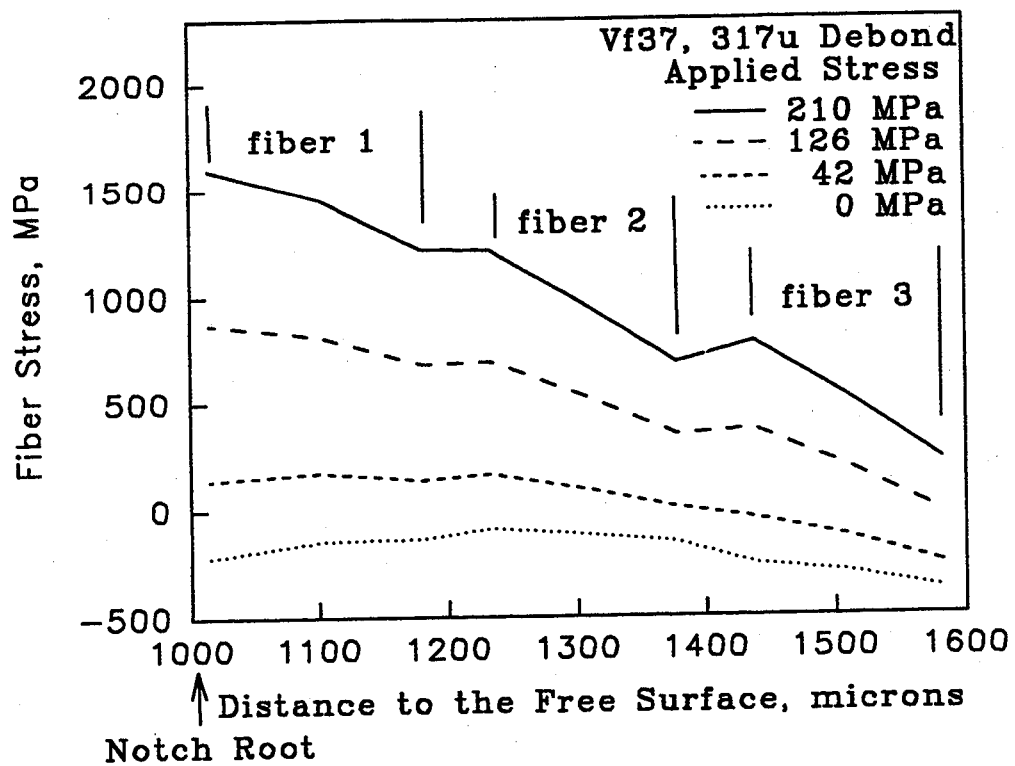
Figure 4.18: Variation of bridged fiber stress with applied stress as a function of position from the free surface.
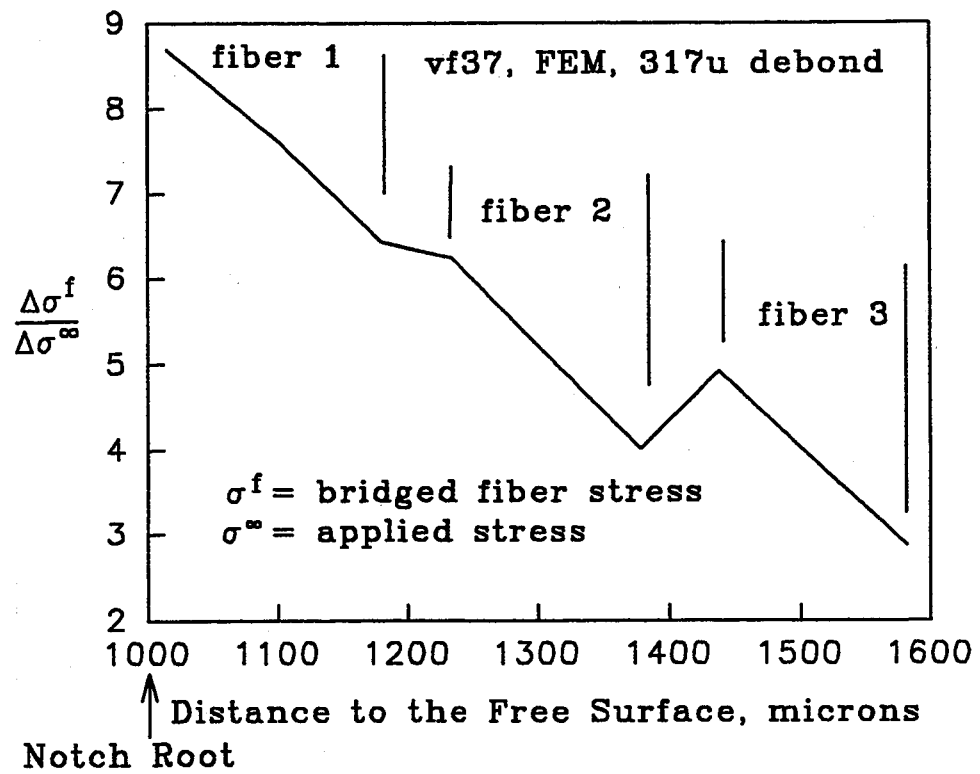
Figure 4.19: Shows the rate of change of the bridged stress with respect to the applied stress. Note that the bridged fiber nearest the crack mouth has the largest rate of stress increase with applied stress.
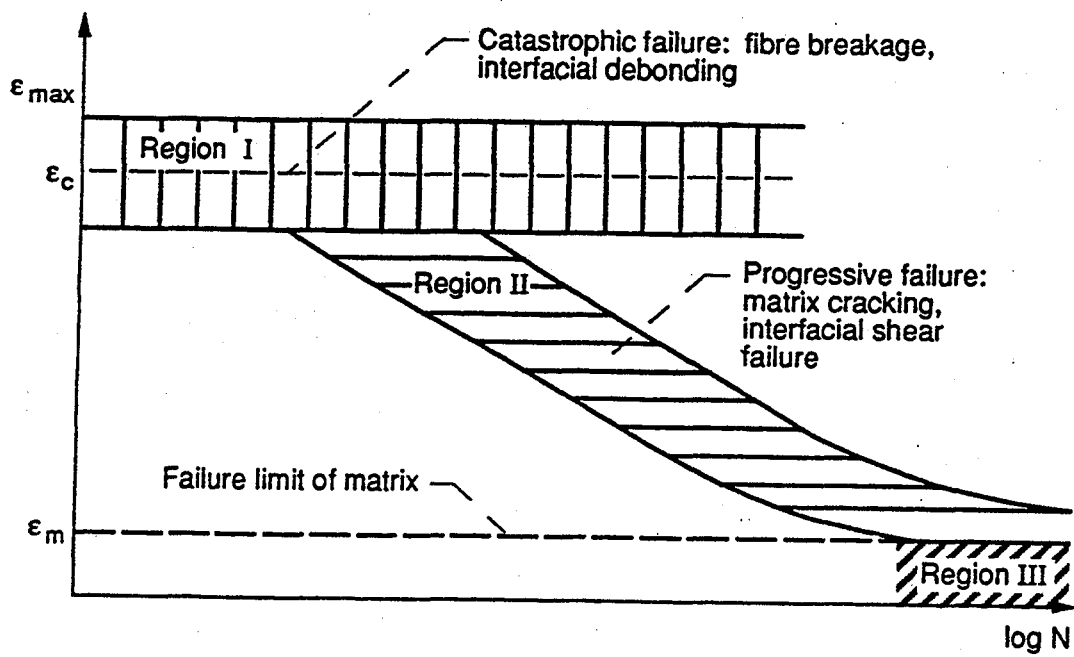
Figure 6.1: Talreja's fatigue life diagram from Reference 41.
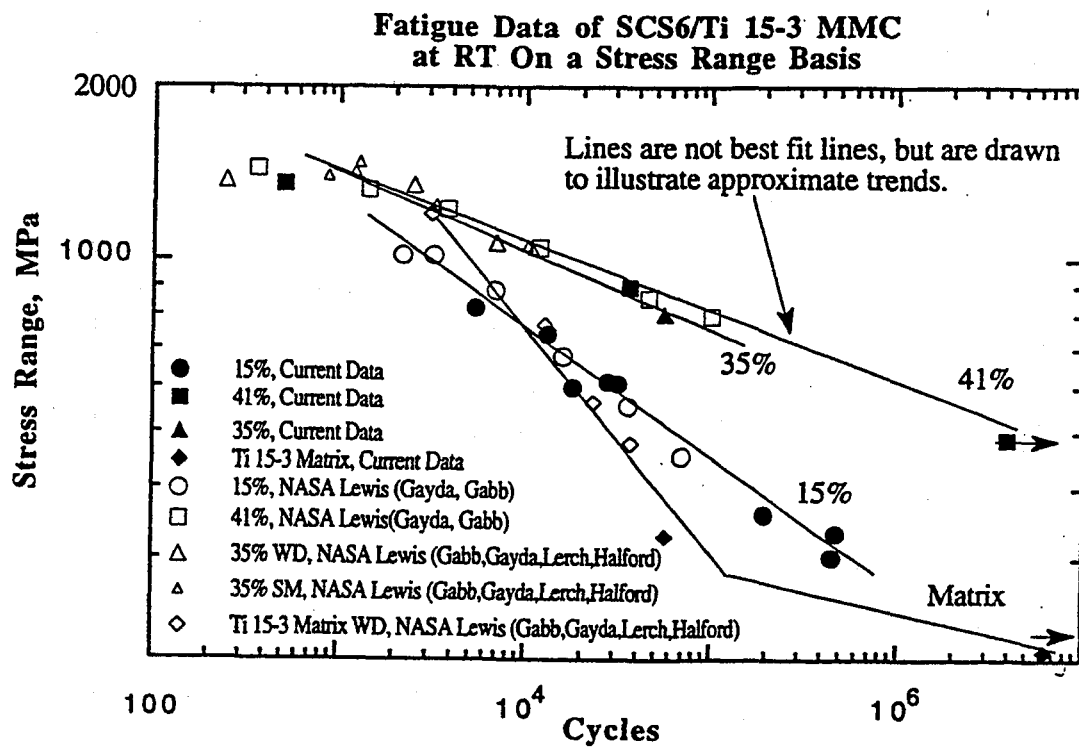
Figure 6.2: Low cycle fatigue stress life curve from Reference 46.
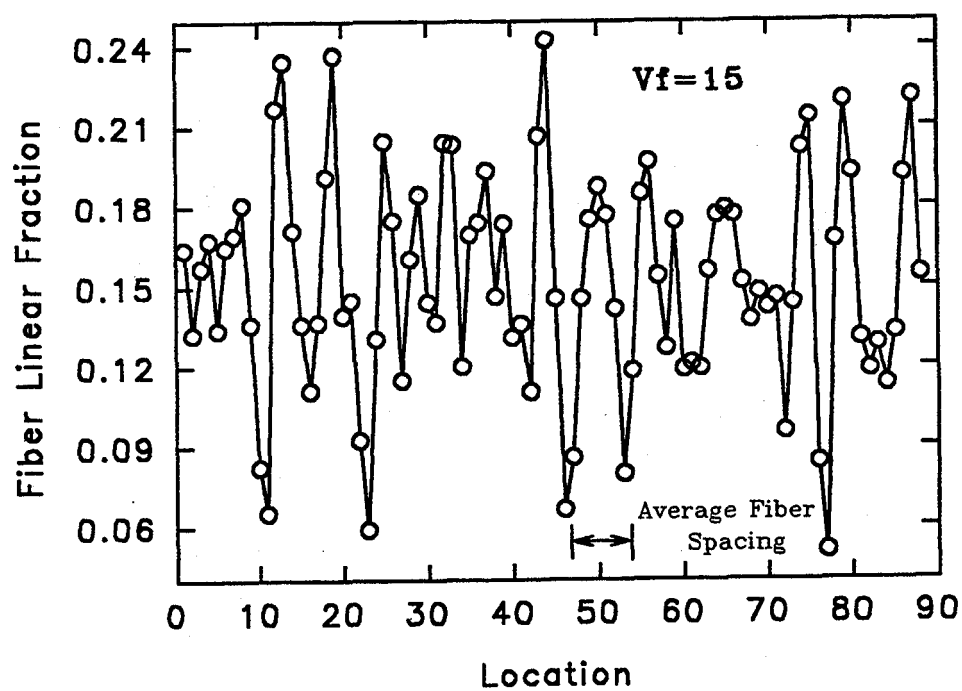
Figure A1.1: Shows how the notch fiber linear fraction varies with position. The

local material behavior can be expected to vary similarly.
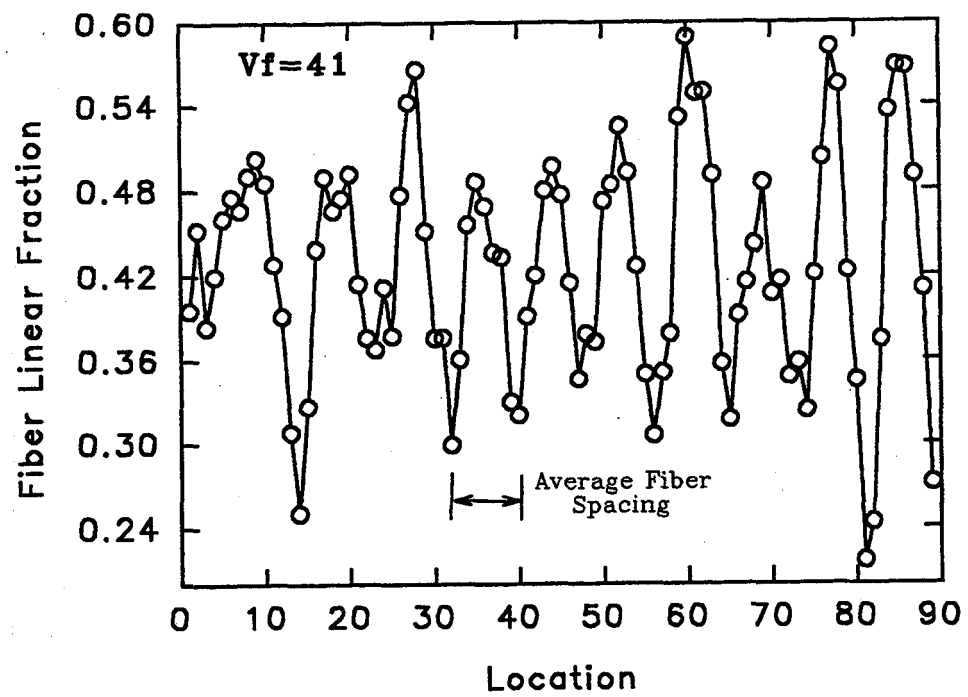
Figure A1.1: Continued
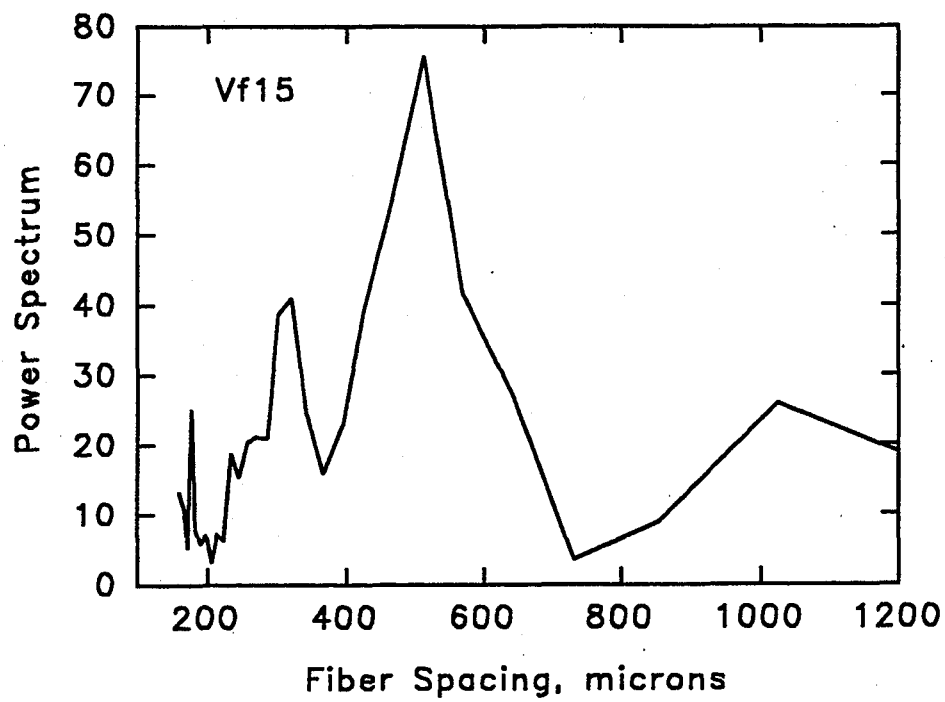
Figure A1.2: Fourier transform power spectrum of notch fiber linear fraction

variation vs period. The peak values are used to define the quarter
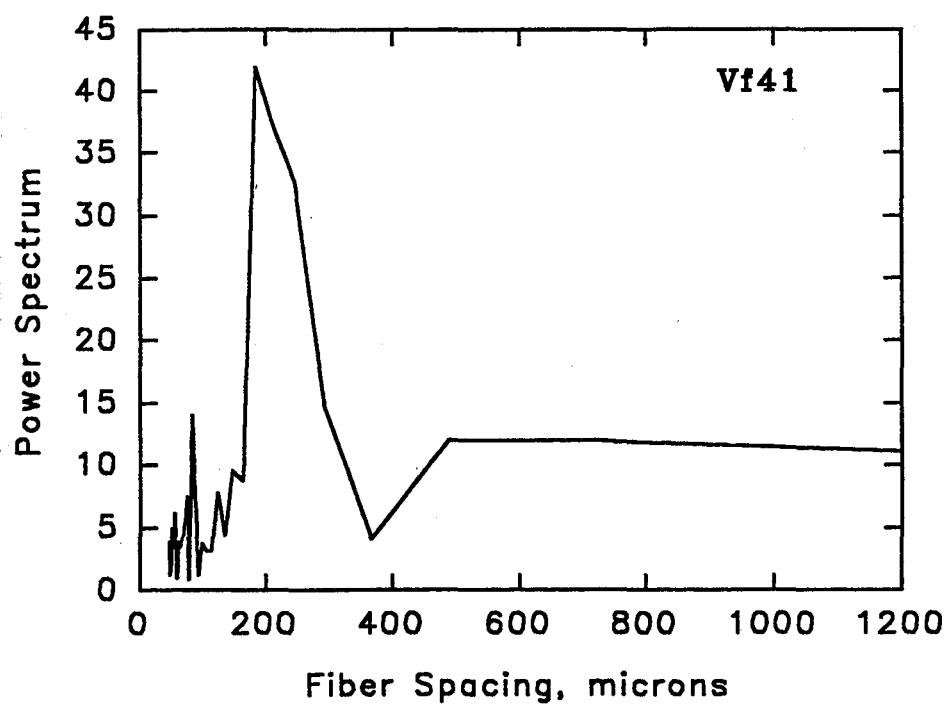
fiber unit cell geometry for the FEM models.
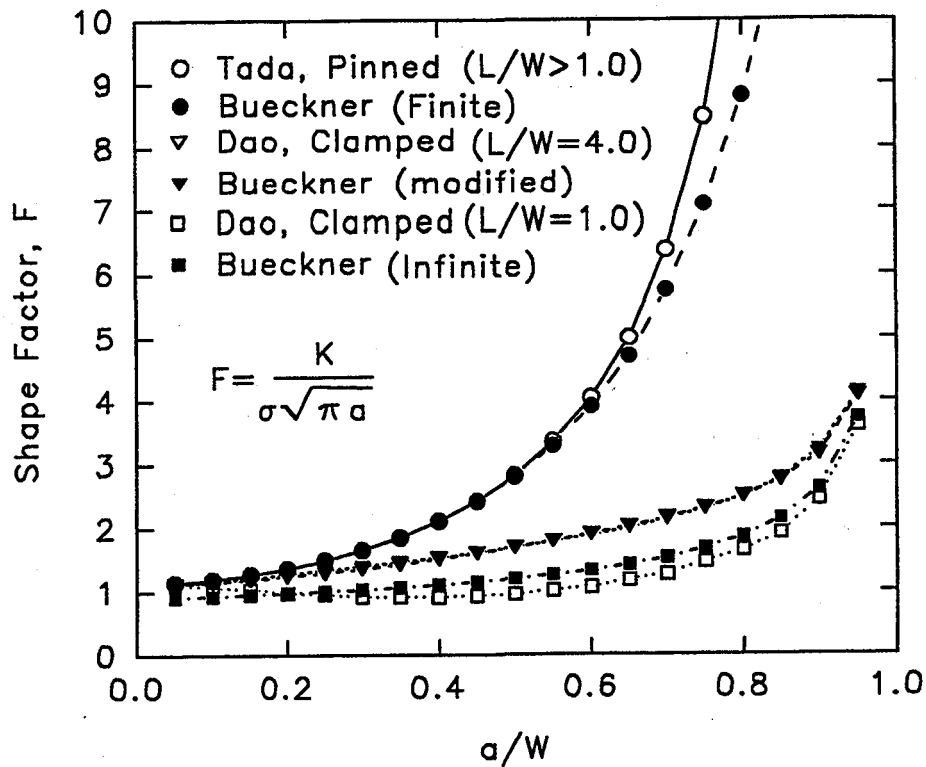
Figure A1.2: Continued.

Figure A2.1: Shape factor vs a/w for various stress intensity solutions. Note the large variation with grip and specimen geometry. The ratio of specimen gage length, L, to width, W, is L/W. Tada, Bueckner, and Dao are references found in Appendix 2.

REPORT DOCUMENTATION PAGE

1. AGENCY USE ONLY (Leave blank)	2. REPORT DATE	3. REPORT TYPE AND DATES COVERED
	September 1993	Final Contractor Report

4. TITLE AND SUBTITLE

A Study of Fiber Volume Fraction Effects in Notched
Unidirectional SCS-6/Ti-15V-3Cr-3Al-3Sn Composite

6. AUTHOR(S)

Steven J. Covey

5. FUNDING NUMBERS

WU–510–01–50
G–NGT–40016

7. PERFORMING ORGANIZATION NAME(S) AND ADDRESS(ES)

University of Cincinnati
Department of Materials Science and Engineering
Cincinnati, Ohio 45221–0012

8. PERFORMING ORGANIZATION REPORT NUMBER

E–8116

9. SPONSORING/MONITORING AGENCY NAME(S) AND ADDRESS(ES)

National Aeronautics and Space Administration
Lewis Research Center
Cleveland, Ohio 44135–3191

10. SPONSORING/MONITORING AGENCY REPORT NUMBER

NASA CR–191165

11. SUPPLEMENTARY NOTES

Project Manager, Brad Lerch, Structures Division, (216) 433–5522.

12a. DISTRIBUTION/AVAILABILITY STATEMENT

Unclassified - Unlimited
Subject Category 24

12b. DISTRIBUTION CODE

13. ABSTRACT (Maximum 200 words)

Notched unidirectional SCS-6/Ti-15–3 composite of three different fiber volume fractions (vf = 0.15, 0.37, and 0.41) was investigated for various room temperature microstructural and material properties including; fatigue crack initiation, fatigue crack growth, and fracture toughness. While the matrix hardness is similar for all fiber volume fractions, the fiber/matrix interfacial shear strength and matrix residual stress increases with fiber volume fraction. The composite fatigue crack initiation stress is shown to be matrix controlled and occurs when the net maximum matrix stress approaches the endurance limit stress of the matrix. A model is presented which includes residual stresses and presents the composite initiation stress as a function of fiber volume fraction. This model predicts a maximum composite initiation stress at vf≈0.15 which agrees with the experimental data. The applied composite stress levels were increased as necessary for continued crack growth. The applied ΔK values at crack arrest increase with fiber volume fraction by an amount better approximated using an energy based formulation rather than when scaled linear with modulus. After crack arrest, the crack growth rate exponents for vf37 and vf41 were much lower and toughness much higher, when compared to the unreinforced matrix, because of the bridged region which parades with the propagating fatigue crack. However, the vf15 material exhibited a higher crack growth rate exponent and lower toughness than the unreinforced matrix because once the bridged fibers nearest the crack mouth broke, the stress redistribution broke all bridged fibers, leaving an unbridged crack. Degraded, unbridged behavior is modeled using the residual stress state in the matrix ahead of the crack tip. Plastic zone sizes have been directly measured using a metallographic technique and allow prediction of an effective matrix stress intensity which agrees with the fiber pressure model if residual stresses are considered. The sophisticated macro/micro finite element models of the 0.15 and 0.37 fiber volume fractions presented here show good agreement with experimental data and the fiber pressure model when an estimated effective fiber/matrix debond length is used.

14. SUBJECT TERMS

Fatigue; Composite; Deformation; SiC/Ti-15–3

15. NUMBER OF PAGES

228

16. PRICE CODE

A11

17. SECURITY CLASSIFICATION OF REPORT	18. SECURITY CLASSIFICATION OF THIS PAGE	19. SECURITY CLASSIFICATION OF ABSTRACT	20. LIMITATION OF ABSTRACT
Unclassified	Unclassified	Unclassified	